Bioimaging Innovations in Bionics and Biomechanics

Lead Guest Editor: Yuan-Chiao Lu

Guest Editors: Ozan Erol, Santiago Orrego, Yao Wu, and Li Zhao

Bioimaging Innovations in Bionics and Biomechanics

Bioimaging Innovations in Bionics and Biomechanics

Lead Guest Editor: Yuan-Chiao Lu
Guest Editors: Ozan Erol, Santiago Orrego, Yao Wu, and Li Zhao

Editorial Board

Contents

Editorial

Bioimaging Innovations in Bionics and Biomechanics

Yuan-Chiao Lu [iD],[1] **Ozan Erol** [iD],[2] **Santiago Orrego** [iD],[3] **Yao Wu,**[1] **and Li Zhao** [iD][4]

[1]*Division of Diagnostic Imaging and Radiology, Children's National Medical Center, Washington, DC, USA*
[2]*Hopkins Extreme Materials Institute, Johns Hopkins University, Baltimore, MD, USA*
[3]*Department of Oral Health Sciences, Maurice H. Kornberg School of Dentistry, Temple University, Philadelphia, PA, USA*
[4]*Department of Biomedical Engineering, George Washington University, Washington, DC, USA*

Correspondence should be addressed to Yuan-Chiao Lu; yclu@jhu.edu

1. Introduction

Recent advances in computational and bioimaging techniques have greatly enhanced the ability of engineers and scientists to better understand the dynamics of the human body and functions of living organisms. Specifically, progressive computational, mathematical, and physics-based approaches have helped researchers to develop sophisticated novel techniques that can solve the problems encountered in the fields of bionics and biomechanics with improved visualization of biological systems and design of new medical devices. These advances in imaging and visualization methods are helping to identify, classify, and quantify patterns in bionics and biomechanical investigations.

The theme of this Special Issue is to explore the state of the art of bionics and biomechanical research using bioimaging technology. The Special Issue consists of original contributions addressing challenges in understanding the mechanics and functions of biological systems and living organisms solved by innovative bioimaging methods. The scope of the Special Issue includes the bioimaging analysis in biomechanics, investigation of the functions of living organisms through imaging techniques, inventions of biomedical devices, and evaluation of surgical treatments. These original research studies provided the biomedical research community an insight into novel biomedical imaging techniques and algorithms on bionics and biomechanics.

2. Description of the Special Issue

This Special Issue accepted 6 papers out of 15 through careful review by editors and peer review, which led to an acceptance ratio of 40%. These 6 original research articles investigated the radiography system improvement, radiographic image analysis, medical image modeling, and imaging technique evaluation.

Y. Liu et al. proposed a novel data-driven decomposition model to decompose the conventional chest radiograph into both soft tissue and bone images and compared the results with virtual dual-energy subtraction (DES) imaging. The proposed approach markedly reduced the visibility of bony structures in chest radiographs and produced soft tissue and bone contrast similar to those produced by the actual DES system. Their work shows potential to enhance diagnosis of lung diseases.

Y.-H. Chang et al. constructed a finite element mandible model (cortical bone, cancellous bone, miniplate, and screws) from high-resolution computed tomography (CT) images to investigate the biomechanical structures of four common occlusion conditions after bilateral sagittal split osteotomy surgical treatment. They observed high stress on the miniplate for all four occlusion conditions, and the screws on the proximal segment near the bone gap experienced high stress. This platform provides more information on the biomechanics of mandible implantation.

W.-E. Hsu et al. compared 15 vertebral measurements on radiographic images of 18 patients with single-level vertebral compression fracture to access the degree of vertebral body height loss and kyphotic angle. The evaluation of these measurements could help to determine the probability of intravertebral clef, and this study could provide a reference for surgeons when using imaging modalities to access the degree of vertebral body collapse.

C.-W. Liao et al. developed a high-frame-rate intraoral periapical sensor with a senor imaging speed of up to 15 Hz for a 2.5D periapical radiography system, which could be used to capture images at different depths of an object. The developed sensor could be combined with tomosynthesis to obtain reconstructed slice images of different depths and has the potential for clinical dentistry applications.

K. Oberhofer et al. fit a generic musculoskeletal model of the lower limbs of an adult female subject to 3D body surface data of children with and without cerebral palsy. They compared the fitted lengths and volumes of six muscle-tendon structures with the subject-specific muscle-tendon lengths and volumes derived from magnetic resonance images. High accuracies were obtained in the fitted lower limbs in both study groups for 3D body surface data, but the accuracies of muscle volumes contained large variations.

S. Shimawaki et al. performed CT imaging on the fingers of 10 male adults gripping cylinders of three different diameters (10, 60, and 120 mm) and constructed 3D computational bone models based on these CT images to measure the flexion angle of each finger joint. Results showed that smaller cylinder diameters were associated with significant increases in the flexion angle of the all joints of four fingers. Consistent results were observed when comparing to the flexion angles of joints using other published methods.

Conflicts of Interest

The Guest Editorial team as a whole declares that any member of the team does not have any conflict of interest or private agreements with companies.

Acknowledgments

Yuan-Chiao Lu
Ozan Erol
Santiago Orrego
Yao Wu
Li Zhao

Research Article

Soft Tissue/Bone Decomposition of Conventional Chest Radiographs Using Nonparametric Image Priors

Yunbi Liu ,[1] **Wei Yang** ,[1] **Guangnan She,**[1] **Liming Zhong,**[1] **Zhaoqiang Yun,**[1] **Yang Chen,**[2,3] **Ni Zhang,**[4] **Liwei Hao,**[1] **Zhentai Lu,**[1] **Qianjin Feng** ,[1] **and Wufan Chen**[1]

[1]School of Biomedical Engineering and Guangdong Provincial Key Laboratory of Medical Image Processing, Southern Medical University, Guangzhou, Guangdong 510515, China
[2]Laboratory of Image Science and Technology, Southeast University, Nanjing 211189, China
[3]Key Laboratory of Computer Network and Information Integration, Southeast University, Ministry of Education, Nanjing 210096, China
[4]Nanfang Hospital, Southern Medical University, Guangzhou 510515, China

Correspondence should be addressed to Wei Yang; weiyanggm@gmail.com

Background and Objective. When radiologists diagnose lung diseases in chest radiography, they can miss some lung nodules overlapped with ribs or clavicles. Dual-energy subtraction (DES) imaging performs well because it can produce soft tissue images, in which the bone components in chest radiography were almost suppressed but the visibility of nodules and lung vessels was still maintained. However, most routinely available X-ray machines do not possess the DES function. Thus, we presented a data-driven decomposition model to perform virtual DES function for decomposing a single conventional chest radiograph into soft tissue and bone images. *Methods*. For a given chest radiograph, similar chest radiographs with corresponding DES soft tissue and bone images are selected from the training database as exemplars for decomposition. The corresponding fields between the observed chest radiograph and the exemplars are solved by a hierarchically dense matching algorithm. Then, nonparametric priors of soft tissue and bone components are constructed by sampling image patches from the selected soft tissue and bone images according to the corresponding fields. Finally, these nonparametric priors are integrated into our decomposition model, the energy function of which is efficiently optimized by an iteratively reweighted least-squares scheme (IRLS). *Results*. The decomposition method is evaluated on a data set of posterior-anterior DES radiography (503 cases), as well as on the JSRT data set. The proposed method can produce soft tissue and bone images similar to those produced by the actual DES system. *Conclusions*. The proposed method can markedly reduce the visibility of bony structures in chest radiographs and shows potential to enhance diagnosis.

1. Introduction

Chest radiography is a widely used diagnostic imaging technique for lung diseases, such as tuberculosis, pneumonia, and lung cancer, because this method is cheap, routinely available, and relatively safe. However, overlying anatomical structures, such as ribs and clavicles, make the reading and interpretation of chest radiographs difficult for radiologists. Such inaccurate analysis may cause serious decision-making errors. Studies showed that approximately 30% of pulmonary nodules in chest radiographs could be missed by radiologists,

and 82% to 95% of such missed nodules are partly obscured by ribs and clavicles [1]. Therefore, suppression of ribs and clavicles in chest radiographs would be potentially useful for improving the detection accuracy of radiologists.

One method to reduce the visual clutter of chest radiographs from overlying anatomy is DES imaging [2]. DES radiography involves capturing two radiographs with the use of two X-ray exposures at two different energy levels. These radiographs are then combined to form a subtraction image that highlights either soft tissue or bone components, as shown in Figure 1. The soft tissue image can achieve
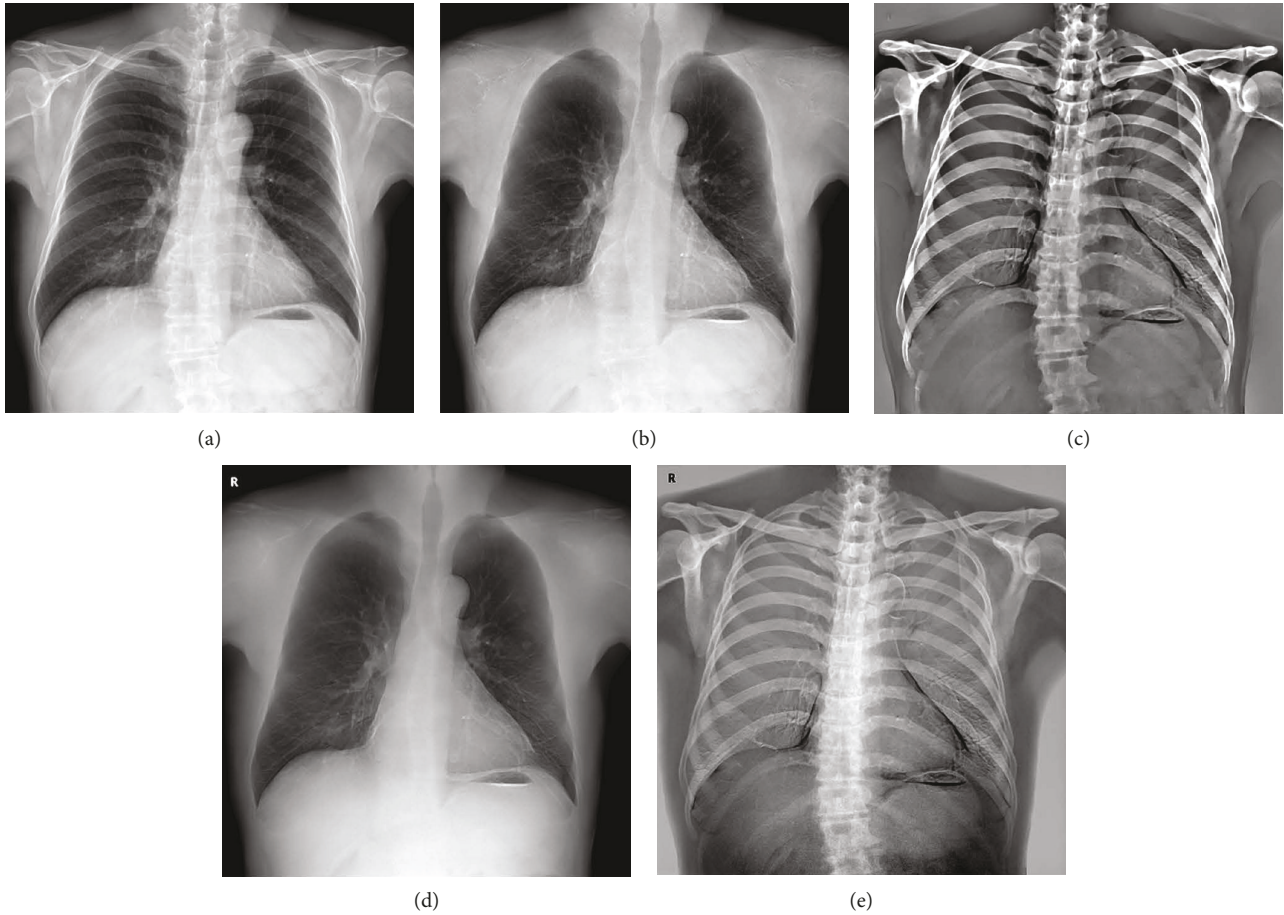
FIGURE 1: An example of the processed DES training set: (a) the standard chest radiograph; (b) the processed DES soft tissue image; (c) the processed DES bone image; (d) the soft tissue image directly obtained by the DES system; (e) the bone image directly obtained by the DES system.

improved visualization of pulmonary nodules because the ribs and clavicles become invisible in this approach. DES chest radiography exhibits many advantages over conventional chest radiography in terms of facilitating image interpretation. However, only a few hospitals use the DES system because of the required specialized equipment.

Another method to remove or suppress the bone components in chest radiographs is the image processing technique that does not require specialized equipment for DES. The commercial software ClearRead Bone Suppress (formerly SoftView) of Riverain Technologies is such a tool for bone suppression in chest radiographs. An early version of the MTANN (massive training artificial neural network) model for rib suppression proposed by Suzuki et al. [3] was evaluated on 60 chest radiographs. Oda et al. [4] found that a combination of rib-suppressed and original chest radiographs could significantly improve the diagnostic performance of radiologists over the use of chest radiographs alone for the detection of small pulmonary nodules. Suppression of bony structures in chest radiographs by using the image processing technique can improve radiologist performance in terms of nodule detection [5], as well as the performance of computer-aided nodule detection (CAD) [6]. Previous methods for bone suppression can generally be divided into

two categories: supervised and unsupervised methods. The supervised methods treat bone suppression in chest radiographs as a regression prediction problem, and the regressors are trained or optimized by a DES training data set to estimate the soft tissue or bone images [3, 7, 8]. The soft tissue images are then reconstructed using the outputs of the regressor with the local image features as the direct inputs or by subtracting the outputs of the regressor from the chest radiographs based on the prediction target of the regressor. However, in the supervised methods, only local features and information of the input chest radiographs can be used to predict the soft tissue or bone images. The unsupervised methods for bone suppression do not require the training set, but these methods need segmentation and border locations of the bony structures as intermediate results [9, 10]. The bone-free images are reconstructed by the blind source separation approach or from the gradient images modified according to the intermediate results. The effectiveness of unsupervised methods highly depends on the accuracy of segmentation and border locations of bony structures.

Unlike the previous methods for the bone suppression of chest radiographs, we proposed a supervised method by treating the separation of soft tissue components from bone components as an image decomposition problem. We

attempted to use the information of whole chest radiographs and the prior knowledge contained in the data set of real DES radiographs to infer the soft tissue and bone images. The decomposition of a single image is highly ill-posed, and the effective prior or regularization is a critical factor for obtaining the reasonable decomposed components. The general image priors, such as smoothness [11] and sparsity [12, 13], are too general to impose effective constraint on the solutions of soft tissue and bone images. Considering the visual characteristics of soft tissue and bone images, these images are distinctly different from the images of other anatomical positions or modalities. Soft tissue images are also distinctly different from bone images, as well as from natural texture images. Thus, we needed to construct specific priors of soft tissue and bone images for the decomposition. Inspired by the work of Tappen and Liu [14], we constructed nonparametric priors of soft tissue and bone images in the kernel density estimation framework. These nonparametric priors are then integrated into a Bayesian maximum a posteriori (MAP) model to estimate the soft tissue and bone images for a given chest radiograph.

The key issue in estimating the nonparametric probability density is sample selection. Given the assumption that if the local features of the patches at the close anatomical position in the chest radiographs are similar, the corresponding patches in the soft tissue and bone images should also be similar. We can search the nearest neighbors of unknown patches in the soft tissue and bone images according to the similarities among patches in chest radiographs. A simple way for sampling is to build a large data set of patch triplets (patches at the same spatial location of chest radiograph, soft tissue image, and bone image) and then search the nearest neighbors of each patch in a given chest radiograph to select the corresponding patches of the soft tissue and bone as samples for density estimation. The size of the data set of patch triplets should be large enough for accurate density estimation. However, a very large data set would lead to a huge computation cost of the nearest neighbor search for each patch, and the information of spatial layout about chest radiographs would be completely ignored. A more efficient way to find the nearest neighbors of patches between two images is the dense matching algorithms, such as SIFT Flow [15], PatchMatch [13], and deformable spatial pyramid (DSP) matching [16]. The corresponding relationship of similar patches between two images can be represented by the dense corresponding field or nearest-neighbor field. The dense matching algorithms can use the spatial smoothness prior of the corresponding fields to accelerate the search of the nearest neighbors of image patches. The smoothness of the corresponding fields can be ensured implicitly or explicitly, which is important to obtain more reasonable matching of patches. In the current study, a hierarchically dense matching algorithm is proposed to solve the corresponding fields by integrating DSP and PatchMatch algorithms.

Given a large data set of DES radiographs, another issue may occur regarding the selection of an effective subset of images as exemplars to estimate the priors. Matching a given chest radiograph to all chest radiographs in the training set would be time-consuming. To alleviate this problem, we selected several of the most similar images of the given chest radiograph as exemplars. Similarities among the images are defined based on their bag-of-words (BoW) histograms for rapid search and selection. Other issues of our decomposition method, such as the normalization of chest radiographs and optimization of decomposition energy function, are also addressed. Our method can produce decomposition results similar to those produced by the real DES system.

2. Methods

2.1. Image Data. The image data used in this study were collected from two data sets. The first data set consisted of 503 posterior-anterior DES chest radiographies acquired with a DES system (Revolution XR/d, GE) at Nanfang Hospital, Guangzhou, China. The X-ray tube voltages for the two exposures were 120 and 60 kV. The sizes of the chest radiographs ranged from 2011×2011 pixels to 2048×2048 pixels, and the pixel sizes ranged from 0.191 mm to 0.195 mm. The images were stored in a DICOM format with a 16-bit depth. The second one was the publicly available Japanese Society of Radiological Technology (JSRT) data set. The JSRT data set consisted of 247 standard posterior-anterior chest radiographic images, among which 154 images contained one pulmonary lung nodule, while the remaining 93 images contained no lung nodules. The nodule diameters range from 5 to 60 mm, and their intensities vary from nearly invisible to very bright. All the images were scanned from plain film radiographs (size: 2048×2048 pixels, pixel size: 0.175 mm).

We have collected 503 cases of DES chest radiographs from the first data set. 403 cases were randomly selected to construct the training set, and the remaining 100 cases were considered the validation set. Each of the DES image triplets in our collected data set included a standard CXR (denoted by $\mathbf{Y}$), a DES soft tissue image (denoted by $\mathbf{S}^0$), and a DES bone image (denoted by $\mathbf{B}^0$). Given the sophisticated nonlinear postprocessing of the raw image data, the relationship $\mathbf{Y} = \mathbf{S}^0 + \mathbf{B}^0$ was not eventually satisfied. To build our decomposition model, we need to process the DES images for exacting the bone component $\mathbf{B}$ and soft tissue component $\mathbf{S}$ to satisfy $\mathbf{Y} = \mathbf{S} + \mathbf{B}$. The gradient $\mathbf{G}$ of the bone components in $\mathbf{Y}$ were obtained as the transformed gradient field of $\mathbf{Y}$ using cross projection tensors [17] from $\mathbf{B}^0$. The bone component $\mathbf{B}$ in $\mathbf{Y}$ was ultimately reconstructed from $\mathbf{G}$ through 2D integration. The corresponding soft tissue component $\mathbf{S}$ can be obtained as $\mathbf{Y}$-$\mathbf{B}$. Finally, we constructed a training set containing the standard DES CXRs, the processed DES soft tissue, and bone images. The spatial resolution of images was then rescaled by the factors 0.25 and 0.3 and cropped by a rectangle centered at the images with a size of 512×512 pixels. An example of the processed training set is shown in Figure 1. In Figure 1, you can see that the contrast was enhanced in the processed DES soft tissue image compared to the original. The bony component can be seen more clearly in the processed DES bone image than the original. For convenience, the processed DES soft tissue and bone images are considered the DES images in the following.
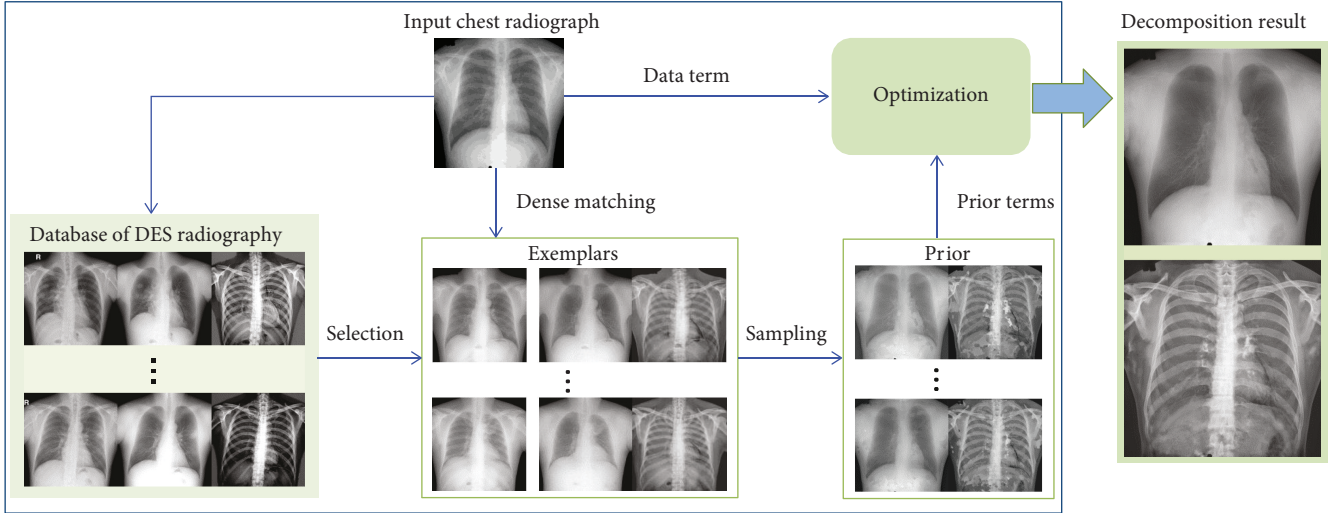
FIGURE 2: Flowchart of the proposed method for decomposition of a chest radiograph.

2.2. Overview of the Proposed Method. Figure 2 illustrates an overview of the decomposition of a standard chest radiograph using the proposed method. A database of the image triplets (chest radiographs and corresponding soft tissue and bone images) of DES radiographs has been established in advance. Given a standard chest radiograph as the input, its soft tissue and bone components are then produced with the following basic steps:

(1) Search and find the exemplars from the database of DES radiographs according to the similarity between the representations of the input chest radiograph and the chest radiographs in the database

(2) Solve the dense corresponding fields between the input image and the chest radiographs of exemplars using a dense matching algorithm

(3) Construct the exemplar-based nonparametric priors for unknown soft tissue and bone images

(4) Optimize an energy function and infer the soft tissue and bone components under a Bayesian MAP framework

The framework for the decomposition of a chest radiograph is similar to the method proposed by Tappen and Liu [14] which was used to solve the face hallucination problem. The image hallucination or superresolution could be treated as an image restoration problem of missing high-frequency components of the original image that need to be restored. However, an image decomposition problem is more ill conditioned and more difficult than face hallucination and image superresolution. The method of Tappen and Liu cannot be directly applied to the task of decomposition of chest radiographs. We need to establish the decomposition model, develop the efficient selection strategy of exemplars and dense matching algorithm for large images, and design the efficient optimization algorithm for the energy function of a decomposition model.

2.3. Bayesian Framework for Decomposition of Chest Radiographs. We expressed the decomposition of chest radiographs in a Bayesian MAP inference framework. Given a chest radiograph $\mathbf{Y}$, the goal was to find a soft tissue image $\mathbf{S}*$ and a bone image $\mathbf{B}*$ which maximize the posterior:

$$\{\mathbf{S}*,\mathbf{B}*\} = \arg \max_{\mathbf{S},\mathbf{B}} p(\mathbf{S}, \mathbf{B} \mid \mathbf{Y})$$
$$= \arg \max_{\mathbf{S},\mathbf{B}} p(\mathbf{Y} \mid \mathbf{S}, \mathbf{B}) p(\mathbf{S}, \mathbf{B}). \qquad (1)$$

Assuming that the bone image $\mathbf{B}$ and the soft tissue image $\mathbf{S}$ were independent, then

$$\{\mathbf{S}*,\mathbf{B}*\} = \arg \max_{\mathbf{S},\mathbf{B}} p(\mathbf{Y} \mid \mathbf{S}, \mathbf{B}) p(\mathbf{S}) p(\mathbf{B}), \qquad (2)$$

where $p(\mathbf{S})$ and $p(\mathbf{B})$ were the probability density functions (image priors) of the soft tissue and bone components, respectively. The likelihood function $p(\mathbf{Y} \mid \mathbf{S}, \mathbf{B})$ expressed the compatibility between the observed chest radiograph and the decomposed soft tissue and bone components. Considering that we expected a chest radiograph $\mathbf{Y}$ to be decomposed as $\mathbf{Y} = \mathbf{S} + \mathbf{B}$, $p(\mathbf{Y} \mid \mathbf{S}, \mathbf{B})$ is expressed as

$$p(\mathbf{Y} \mid \mathbf{S}, \mathbf{B}) = \frac{1}{Z_d} \exp\left(-\lambda \|\mathbf{Y} - \mathbf{S} - \mathbf{B}\|_2^2\right), \qquad (3)$$

where λ is a tuning coefficient and Z_d is the normalization constant to make $p(\mathbf{Y} \mid \mathbf{S}, \mathbf{B})$ a valid distribution.

2.4. Exemplar-Based Nonparametric Image Priors. The key for successfully decomposing chest radiographs is the effective image priors $p(\mathbf{B})$ and $p(\mathbf{S})$. As previously discussed, the general image priors cannot work well in separating the soft tissue component from the bone component. We formed the nonparametric priors from the database of actual DES radiographs. The image triplets in the database were denoted as the set $\{(\mathbf{Y}_i, \mathbf{S}_i, \mathbf{B}_i), i = 1, 2, \cdots, N\}$. The probability density

of a soft tissue image $\mathbf{S}$ in a form of kernel density estimation can be written as

$$p(\mathbf{S}) = \frac{1}{Z_S} \sum_{i=1}^{N} K(\mathbf{S}, \mathbf{S}_i ; \mathbf{T}_i), \qquad (4)$$

where $K(\mathbf{S}, \mathbf{S}_i ; \mathbf{T}_i)$ is a kernel function measuring the similarity between $\mathbf{S}$ and $\mathbf{S}_i$, Z_S is the normalization factor, and $\mathbf{T}_i$ is a corresponding field which represents the pixel-to-pixel corresponding between $\mathbf{S}$ and $\mathbf{S}_i$. Using the corresponding field $\mathbf{T}_i$, the relationships of image patches were established to align $\mathbf{S}$ and $\mathbf{S}_i$. For example, an image patch centered at x in $\mathbf{S}$ (denoted as $R_x \mathbf{S}$) corresponded to the image patch centered at $x + \mathbf{T}_i(x)$ in $\mathbf{S}_i$ (denoted as $R_{x+\mathbf{T}i(x)} \mathbf{S}_i$).

If the Gaussian kernel is adopted as the kernel function for density estimation, the prior $p(\mathbf{S})$ can be formulated as

$$p(\mathbf{S}) = \frac{1}{Z_S} \sum_{i=1}^{N} \exp\left(-\eta_S \sum_{x \in \mathbf{S}} \left\| R_x \mathbf{S} - R_{x+\mathbf{T}_i(x)} \mathbf{S}_i \right\|_2^2\right), \qquad (5)$$

where η_S is a hyperparameter. Similarly, the prior $p(\mathbf{B})$ can be written as

$$p(\mathbf{B}) = \frac{1}{Z_B} \sum_{i=1}^{N} \exp\left(-\eta_B \sum_{x \in B} \left\| R_x \mathbf{B} - R_{x+\mathbf{T}_i(x)} \mathbf{B}_i \right\|_2^2\right). \qquad (6)$$

When there are many samples (e.g., N is large) in the image database, it would be very expensive (and unnecessary) to construct the priors $p(\mathbf{B})$ and $p(\mathbf{S})$ using all samples. To alleviate this problem, a small subset of samples should be selected in the image database as exemplars. The above priors estimated using the selected samples are regarded as exemplar-based priors. The search and selection method for the exemplars and the resolution of corresponding fields will be described in the following subsections.

2.5. Preprocessing and Local Feature Descriptors of Chest Radiographs. Due to the differences in acquisition conditions and patients, the density and contrast vary within different chest radiographs, which were acquired by X-ray digital radiography (DR) or computed radiography and DES systems. These differences may affect the comparability of image features. The preprocessing step of contrast normalization is necessary to achieve consistency of chest radiographs. We adopted the guided image filter [18] to enhance the structural details and normalize the contrast of chest radiographs.

A guided image filter is an edge-preserving smoothing filter, which is effective and efficient in many computer vision and graphic applications. The principle of the guided image filter is that the input image is filtered through a guidance image through utilizing the structures in the guidance image. As a result, the output image maintained the overall characteristics and gradients of the input image when the input image is used as the guidance image. For a given chest radiograph $\mathbf{Y}$, its smoothed image by the guided image filter with a large radius (e.g., 40 pixels) is used as a base layer $\mathbf{Y}_0$.

The detail layer is $\mathbf{Y}_d = \mathbf{Y} - \mathbf{Y}_0$. The chest radiograph $\mathbf{Y}$ is normalized as

$$\mathbf{Y} \longleftarrow \mathbf{Y}_n = \frac{\mathbf{Y}_d - \mu_d}{\sigma_d}, \qquad (7)$$

where μ_d and σ_d are the intensity mean and standard deviation of $\mathbf{Y}_d$, respectively. $\mathbf{Y}_n$ is the normalized $\mathbf{Y}$. Given that the bone images are rather homogeneous at the large scale, the base layers of the bone images are very homogeneous. Actually, the base layer of $\mathbf{Y}$ is almost identical to that of the corresponding soft tissue image $\mathbf{S}$ apart from a global intensity offset. Thus, the soft tissue image $\mathbf{S}$ is normalized consistently to equation (7) without the loss of structural details as

$$\mathbf{S} \longleftarrow \mathbf{S}_n = \frac{\mathbf{S} - \mathbf{Y}_0 - \mu_S}{\sigma_d}, \qquad (8)$$

where μ_S is the intensity mean of $\mathbf{S} - \mathbf{Y}_0$ and $\mathbf{S}_n$ is the normalized $\mathbf{S}$. And the bone image $\mathbf{B}$ is normalized as

$$\mathbf{B} \longleftarrow \mathbf{B}_n = \frac{\mathbf{B} - \mu_B}{\sigma_d}, \qquad (9)$$

where μ_B is the intensity mean of $\mathbf{B}$ and $\mathbf{B}_n$ is the normalized $\mathbf{B}$. In this way, the chest radiographs exhibited consistent contrast with the enhanced details, and the relationship $\mathbf{Y} = \mathbf{S} + \mathbf{B}$ between the normalized images was also maintained. The normalized soft tissue/bone images by the use of the proposed normalization procedure can be easily recovered to their original form, and the details of corresponding chest radiographs are enhanced.

In our proposed system, the image representations and the corresponding image patches highly relied on the local feature descriptors. Ideally, the descriptors should have high discriminative power and invariance to image transformations. However, no single kind of dense local descriptor can achieve these two goals very well. We combined three kinds of dense descriptors to describe the local feature and the contextual information of chest radiographs. The first kind of descriptor is the small raw image patch (e.g., 7×7 patch). The raw image patches contain the important (normalized) intensity information. The second kind of descriptor exhibits the responses of the modified Leung-Malik (LM) filter bank [19]. The modified LM filter bank consists of the first and second derivatives of Gaussians at six orientations and four scales resulting in a total of 48 filters, one Laplacian of Gaussian filter and one Gaussian filter. The filter scales range from 1 to 32 pixels. The 50-dimensional filter bank responses are normalized by Weber's law, which can obtain the information of small textural and large structures. The third kind of descriptor is the dense SIFT (Scale-Invariant Feature Transform) descriptor [20], which is extracted to characterize local image structures and encode contextual information. For each pixel in an image, its neighborhood (e.g., 16×16 block) is divided to a 4×4 cell array. The gradient orientations in each cell are quantized into eight bins. The obtained dense

SIFT descriptors are $4 \times 4 \times 8 = 128$ dimensional. The combined descriptors are 277 $(49 + 50 + 128)$ dimensional. Finally, we set the different weight factors for the three kinds of descriptor to balance their contributions and reduce the dimensionality of combined descriptors through principal component analysis (PCA) to alleviate computational burden.

2.6. Search and Selection of Exemplars from Image Database. Rapid search of similar images for an input image from a database can be performed by comparing the global representations of images. We used BoW image representation [21] as the global representation of the chest radiographs. The BoW image representation is analogous to the BoW representation of text documents, which makes techniques for text retrieval readily applicable to the problem of image retrieval. The BoW model first needs to construct a codebook containing visual words (cluster centers) by clustering invariant descriptors on a given training data set and then exacts the local descriptors of an input image that will be vector quantized with respect to these visual words. Given a codebook, an image is represented as a histogram formed by the number of occurrences of each visual word on the sampled local descriptors from the image. In this study, the codebooks of local descriptors are generated by k-means clustering. Since the difference between chest radiographs is subtle, a relatively large codebook is needed. To further improve the descriptive power of BoW histograms, a spatial pyramid model is adopted to incorporate the spatial information of images [22]. Specifically, the spatial pyramid includes two levels: the entire image (level 0) and its four rectangular grid cells (level 1). The BoW histograms of the entire image region and the four subregions are concentrated as the global representation of a chest radiograph.

Let $H(k)$ denote the k_{th} element of a concentrated histogram H. The image similarity measure of two images A and B in the image search stage can be defined as histogram intersection:

$$\text{sim}(A, B) = \text{sim}(H_A, H_B) = \sum_k \min(H_A(k), H_B(k)), \quad (10)$$

where the maximum of k is 5000. This similarity measure refers to an approximate number of matches between the local descriptors at two spatial levels in the two images. Other histogram similarities or distance such as the Earth Mover's Distance can also be used [23]. The top M most similar chest radiographs with the corresponding soft tissue and bone images in the database to a given chest radiograph in terms of similarity measure (equation (10)) are selected as exemplars for the estimation of priors.

2.7. Hierarchically Dense Matching of Chest Radiographs. To construct the priors in equations (5) and (6), we determined the dense corresponding fields and matched the pixels between the input and the chest radiographs of selected exemplars. Unlike the traditional dense matching problems such as stereo or nonrigid interpatient registration, in which the two images contain the same scene or objects, we attempted to densely match intrapatient chest radiographs containing different objects with varying appearances and shape. The variations in chest radiographs can make matching of the low-level image patches ambiguous.

To address the dense matching problem, several dense matching methods have been proposed which typically enforce both appearance agreement between matched pixels and geometric smoothness between neighboring pixels, such as SIFT Flow [15] and deformable spatial pyramid (DSP) [16]. SIFT Flow relies on the pixel-level Markov random field (MRF) model with a hierarchical optimization technique. DSP matching uses a pyramid graph model that simultaneously optimizes match consistency ranging from an entire image to coarse grid cells and to every single pixel. Typically, DSP is faster than SIFT Flow because DSP only optimizes the MRF energy in the coarse levels with direct local search in the pixel-level layer. However, DSP uses the downsampled local descriptors in the coarse grid cells that may cause the wrong matching, which cannot be corrected well in the following local search. The PatchMatch algorithm computes fast dense correspondences in another way [24]. For efficiency, this algorithm abandons the global optimization that enforces explicit smoothness on neighboring pixels. Instead, it progressively searches for correspondences by a randomized search technique; a reliable match at one pixel subsequently guides the matching locations of its nearby pixels, thereby implicitly enforcing geometric smoothness. Since the PatchMatch algorithm can only determine a local optimum because of the randomized search and the field propagation strategy, the final correspondence field estimated by PatchMatch highly relies on the initial estimation. The PatchMatch algorithm also discards the prior knowledge on the spatial layout of images, which starts at a totally random initialization.

Matching two images should determine the most similar local feature (match) from one image for each pixel to the other image with the geometric constraint. However, the effective geometric constraints are unclear. Intuitively, the significant matching between chest radiographs should have close appearance and should be located near the same anatomical sites simultaneously. We performed dense matching of chest radiographs in a hierarchical way similar to DSP matching but without the need of energy optimization similar to the PatchMatch algorithm.

The input chest radiograph is divided into nonoverlapping rectangular grid cells, and the chest radiographs in the database are divided into overlapping cells with the fixed step size analogous to the DSP matching algorithm. The similarity between grid cells is defined as the intersection of the BoW histogram. The grid cells should be large enough (e.g., 32×32 pixels) to estimate the reliable distribution of visual words and identify their anatomical sites. Given that all chest radiographs exhibit a similar spatial layout like that of the clavicles located at the top of the lung field and the hearts located between the left and right lungs, the search for similar grid cells was limited in the local regions of a 1/4 image area. By matching the grid cells, we obtained a very coarse corresponding field $\mathbf{T}$. Using $\mathbf{T}$ with random permutation as the initial estimation

---

Input: Two image A (source image) and B (target image);
Dense local descriptors F_A of A and F_B of B.
Output: Corresponding field **T**.
1: Divide A to the non-overlapping cells of size $w \times w$ and obtain the BoW histograms H_A^i for each cell i.
2: Divide B to overlapping cells of size $w \times w$ with step size s and obtain the BoW histograms H_B^j of each cell j.
3: Determine the most similar cell centered at (x_B, y_B) in B for each cell c_A in A.
4: Set $T(x, y)=(x_B, y_B)$ $((x, y) \in c_A)$ for each cell c_A in A and random permute of **T**.
5: Update **T** by field propagation as PatchMatch algorithm using the local descriptors F_A and F_B.
6: Update **T** by locally randomized search using the local descriptors F_A and F_B.
7: Repeat steps 5 and 6 a fixed number of times or until convergence.

ALGORITHM 1: Hierarchically dense matching.

(a)   (b)

(c)   (d)
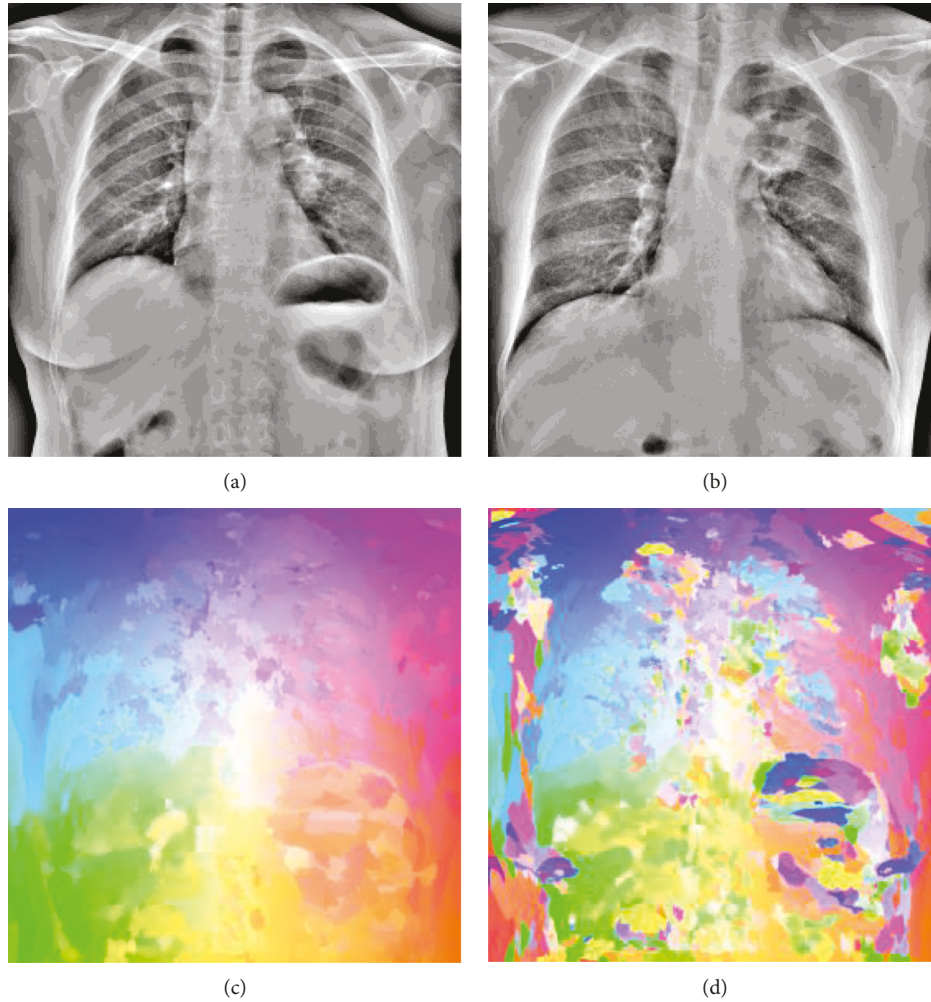
FIGURE 3: Visualization of corresponding fields.

of the corresponding field, we applied the field propagation and local randomized search as the PatchMatch algorithm to refine the corresponding field. More details of our hierarchically dense matching are described in Algorithm 1. The corresponding fields of two chest radiographs found by the proposed hierarchically dense matching and PatchMatch algorithms are presented in Figure 3. Obviously, our algorithm can achieve a smoother corresponding field. In

contrast, the corresponding field solved by the PatchMatch algorithm lacks consistency due to its overrandomization.

Figure 3 illustrates a visualization of corresponding fields by our proposed hierarchically dense matching and Patch-Match algorithms. Figures 3(a) and 3(b) show two normalized chest radiographs as the source image and target image for dense matching, respectively. Figures 3(c) and 3(d) illustrate the visualization of the corresponding fields solved by

our hierarchically dense matching and PatchMatch algorithms, respectively. Corresponding fields in Figures 3(c) and 3(d) are displayed with the same color mapping.

2.8. Optimization of Decomposition Energy Function with Exemplar-Based Priors. The MAP estimation of the soft tissue image **S** and the bone image **B** can be rewritten as

$$\{\mathbf{S}*, \mathbf{B}*\} = \arg\min_{\mathbf{B},\mathbf{S}} E(\mathbf{S}, \mathbf{B}), \tag{11}$$

where

$$E(\mathbf{S}, \mathbf{B}) = -\log p(\mathbf{Y} \mid \mathbf{S}, \mathbf{B}) - \log p(\mathbf{S}) - \log p(\mathbf{B})$$
$$= E_d(\mathbf{S}, \mathbf{B}) + E_p(\mathbf{S}) + E_p(\mathbf{B}), \tag{12}$$

where E_d and E_p are the data and prior terms, respectively. Ignoring the constant, we obtained

$$E_d(\mathbf{S}, \mathbf{B}) = \lambda \|\mathbf{Y} - \mathbf{S} - \mathbf{B}\|_2^2, \tag{13}$$

$$pcE_p(\mathbf{S}) = -\log \sum_x \exp\left(-\eta_S \sum_{i=1}^{M} \left\| R_x \mathbf{S} - R_{x+\mathbf{T}_i(x)} \mathbf{S}_i \right\|_2^2\right). \tag{14}$$

The prior in equation (14) can be considered induced from the density estimated by image-level samplings. As for patch-level samplings, the prior term $E_p(\mathbf{S})$ can be reformulated as

$$E_p(\mathbf{S}) = -\sum_x \log \sum_{i=1}^{M} \exp\left(-\eta_S \left\| R_x \mathbf{S} - R_{x+\mathbf{T}_i(x)} \mathbf{S}_i \right\|_2^2\right). \tag{15}$$

Compared to equation (14), the form of equation (15) is more flexible, hence adopted in our final decomposition model. Analogously, we can modify the prior term $E_p(\mathbf{B})$.

The gradients of $E(\mathbf{S}, \mathbf{B})$ with respect to **S** and **B** can be derived easily, and the energy function $E(\mathbf{S}, \mathbf{B})$ can be minimized by a gradient descent algorithm. However, the gradient descent algorithms usually need many iterations to converge. We proposed an iteratively reweighted least-squares (IRLS) [25] scheme to efficiently minimize the energy function $E(\mathbf{S}, \mathbf{B})$ by generating a sequence $\{\mathbf{S}_t, \mathbf{B}_t\}$ via

$$\{\mathbf{S}^{t+1}, \mathbf{B}^{t+1}\} = \arg\min_{\mathbf{B},\mathbf{S}} \lambda \|\mathbf{Y} - \mathbf{S} - \mathbf{B}\|_2^2$$
$$+ \eta_S \sum_x \sum_{i=1}^{M} w_{x,i}^s \left\| R_x \mathbf{S} - R_{x+\mathbf{T}_i(x)} \mathbf{S}_i \right\|_2^2 \tag{16}$$
$$+ \eta_B \sum_x \sum_{i=1}^{M} w_{x,i}^b \left\| R_x \mathbf{B} - R_{x+\mathbf{T}_i(x)} \mathbf{B}_i \right\|_2^2,$$

where the weights are

$$w_{x,i}^s = \frac{\exp\left(-\eta_S \left\| R_x \mathbf{S}^t - R_{x+\mathbf{T}_i(x)} \mathbf{S}_i \right\|_2^2\right)}{\sum_{j=1}^{M} \exp\left(-\eta_S \left\| R_x \mathbf{S}^t - R_{x+\mathbf{T}_j(x)} \mathbf{S}_j \right\|_2^2\right)},$$
$$\tag{17}$$
$$w_{x,i}^b = \frac{\exp\left(-\eta_B \left\| R_x \mathbf{B}^t - R_{x+\mathbf{T}_i(x)} \mathbf{B}_i \right\|_2^2\right)}{\sum_{j=1}^{M} \exp\left(-\eta_B \left\| R_x \mathbf{B}^t - R_{x+\mathbf{T}_j(x)} \mathbf{B}_j \right\|_2^2\right)}.$$

The solution $\{\mathbf{S}_{t+1}, \mathbf{B}_{t+1}\}$ can be obtained by solving the following linear equations:

$$\left(\lambda + \eta_S \sum_x R_x^T R_x\right) \mathbf{S} + \lambda \mathbf{B} = \lambda \mathbf{Y} + \eta_S \sum_{i=1}^{M} \sum_x w_{x,i} R_x^T R_{x+\mathbf{T}_i(x)} \mathbf{S}_i,$$

$$\lambda \mathbf{S} + \left(\lambda + \eta_B \sum_x R_x^T R_x\right) \mathbf{B} = \lambda \mathbf{Y} + \eta_B \sum_{i=1}^{M} \sum_x w_{x,i}^b R_x^T R_{x+\mathbf{T}_i(x)} \mathbf{B}_i.$$
$$\tag{18}$$

Since $w_{x,i} R_x^T$ is the operation to rearrange the weighted patches into an image and $R_x^T R_x$ is just a diagonal matrix, the linear equations can be easily solved element-wise. The initial solution of **S** and **B** can be obtained by substituting the two prior terms by their quadratic upper bound using Jensen inequality.

2.9. Algorithm Summary. The DES image triplets in an established database are denoted as the set $\{(\mathbf{Y}_i, \mathbf{S}_i, \mathbf{B}_i), i = 1, 2, \cdots, N\}$, which were preprocessed and normalized by the use of the approach described in Section 2.5. A PCA projection matrix **P** for local descriptors and a BoW codebook **D** were learned on the samples of local descriptors from the database. For each (normalized) chest radiograph $\mathbf{Y}_i$ in the database, the dense local descriptors F_i, the spatial pyramid representation H_i, and the BoW histograms of the subregions were computed by the use of **P** and **D** in advance.

The proposed decomposition procedure of a new chest radiograph **Y** can be summarized as follows:

Step 1. Preprocess and normalize the input chest radiograph **Y** according to equation (7). Let $\mathbf{Y}_0$ denote the base layer of **Y**. μ_d and σ_d are the intensity mean and standard deviation of $\mathbf{Y} - \mathbf{Y}_0$, respectively. The normalized **Y** is computed as $\mathbf{Y} \longleftarrow \mathbf{Y}_n = (\mathbf{Y}_d - \mu_d)/\sigma_d$.

Step 2. Compute the dense local descriptors F of **Y** by the use of the PCA projection matrix **P**.

Step 3. Compute the spatial pyramid representation H and the BoW histograms of subregions of $\mathbf{Y}_n$ by use of the codebook **D**.

Step 4. Select the top M most similar chest radiographs in the database in terms of similarity measure (equation (10)) as the exemplars of $\mathbf{Y}$.

Step 5. Solve the dense corresponding field $\mathbf{T}_k$ between $\mathbf{Y}$ and $\mathbf{Y}_k$ using Algorithm 1 for each exemplar k ($k = 1, 2, \cdots, M$).

Step 6. Construct the nonparametric priors for unknown soft tissue image $\mathbf{S}$ and bone image $\mathbf{B}$ according to equations (5) and (6).

Step 7. Optimize the energy function in equation (12) by the use of the IRLS scheme, and solve the soft tissue image $\mathbf{S}$ and bone image $\mathbf{B}$.

Step 8. Rescale the soft tissue image $\mathbf{S}$ and bone image $\mathbf{B}$, and compensate the base layer of the soft tissue image $\mathbf{S}$ as $\mathbf{S} \longleftarrow \sigma_d \mathbf{S} + \mathbf{Y}_0 + \mu_d, \mathbf{B} \longleftarrow \sigma_d \mathbf{B}$.

The final decomposition results of the input chest radiograph $\mathbf{Y}$ are $\mathbf{S}$ and $\mathbf{B}$ obtained in Step 8.

2.10. Experimental Settings. The experiments were conducted on a PC with a duo Intel Xeon CPU (3.2 GHz) and 16 GB RAM. The implementations were performed using Matlab 2016a with a VLFeat toolbox [26].

The weight coefficients for the three kinds of local descriptors were set to achieve the same variance for each dimension of the combined descriptors. To accelerate the image search and matching procedures, the dimensionality of the combined descriptors was reduced to 60 by PCA, whereas about 98% of variation of the descriptors was maintained. The codebook for BoW representations was generated by k-means clustering on the samples of local descriptors from the training data set. The size of each BoW codebook was set to 5000. The codebook was used to compute the BoW histograms for both the image search and hierarchical dense matching. To perform the hierarchically dense matching algorithm, the size w of subregion was set to 32×32 pixels, and the iteration number of corresponding field propagation and locally randomized search was set to 5. The size of sampling patches for constructing the priors from the actual soft tissue and bone images was set to 5×5 pixels.

We used a case-wise procedure to construct the exemplar-based priors and evaluate the performance of the decomposition results. The top M most similar cases to the testing chest radiograph among the training set were then selected as the exemplars. The maximum value of M was set to 7 in the experiments.

In the energy function of image decomposition, four parameters, namely, λ, η_S, η_B, and the number of exemplars M, were considered. λ is in the range of [10^{-1} to 10^6], and η_S is in the range of [10^{-6} to 0.5]. η_B was set as $2 \times \eta_S$. A large value of η_S would lead to numerical problems. The effect of different parameters was investigated in the following subsections. The average computation time of our decomposition procedure using the unoptimized implementation is 135.8 seconds when the number of selected exemplar images

is 5. Most of the computation time is spent in the stage of hierarchically dense matching, and it is dependent on the size of the image and the number of selected exemplars.

The decomposition performance of the soft tissue and bone was quantitatively evaluated using the following measures: The root mean squared error (rmse) is used to evaluate the reconstruction error of the estimated soft tissue/bone image relative to the actual (normalized) soft tissue/bone image, which is defined as

$$\text{rmse} = \sqrt{\frac{1}{n} \sum_x \left(\widehat{Z}(x) - Z(x) \right)^2}, \qquad (19)$$

where $\widehat{Z}$ is a reconstructed soft tissue/bone image, Z is the corresponding "ground truth" image, x denotes the pixel locations in Z, and n is the number of pixels in the image Z. A smaller value of rmse indicates a better estimation of the ground truth. The quality of bone suppression is also evaluated using the bone suppression ratio (bsr) which is defined as [10]

$$\text{bsr} = 1 - \frac{\sum_x \left(\widehat{\mathbf{S}}(x) - \mathbf{S}(x) \right)^2}{\sum_x \left(\mathbf{Y}(x) - \mathbf{S}(x) \right)^2}, \qquad (20)$$

where $\widehat{\mathbf{S}}$ is an estimation of the actual soft tissue image $\mathbf{S}$ and $\mathbf{Y}$ is the testing chest radiograph. bsr = 1 indicates perfect performance.

If the bone component is treated as a type of structural noise, then the bone suppression procedure of the chest radiograph is considered denoising or filtering. A well-known denoising performance measure called the structural similarity image measure (ssim) [27] can be also used to evaluate the quality of the decomposed soft tissue and bone images. The intensity ranges of images are rescaled into the range of [0 to 255], and the default setting parameters in the implementation (https://ece.uwaterloo.ca/~z70wang/research/ssim/) of ssim are used to compute the values of ssim.

3. Experimental Results

3.1. Effect of Hyperparameters. We varied the values of the four parameters λ, η_S, η_B, and M to investigate their effect and to determine the proper settings. Figure 4 shows the average measures of decomposition performance at different λ with fixed η_S ($\eta_S = 10^{-5}$) and fixed M ($M = 5$). The exemplar images were selected as described in Subsection 2.5. When the value of λ is large, the optimization of the energy function tends to make substantial contributions of the data term to the decomposed images. We observed that larger λ leads to better decomposition in terms of three performance measures. However, when the parameter λ becomes very large, the decomposition results can be extremely arbitrary and meaningless because of ignoring the use of the prior terms. An appropriate value of λ according to the experimental results is 100.

Figure 5 shows the average measures of decomposition performance at different η_S with fixed λ ($\lambda = 100$) and fixed
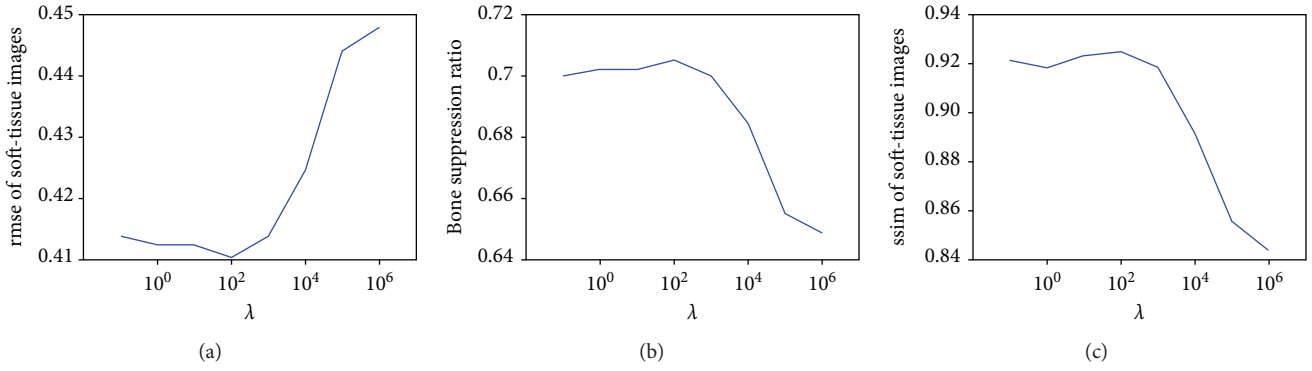
FIGURE 4: The effect on decomposition performance of parameter λ (weight of the data term).
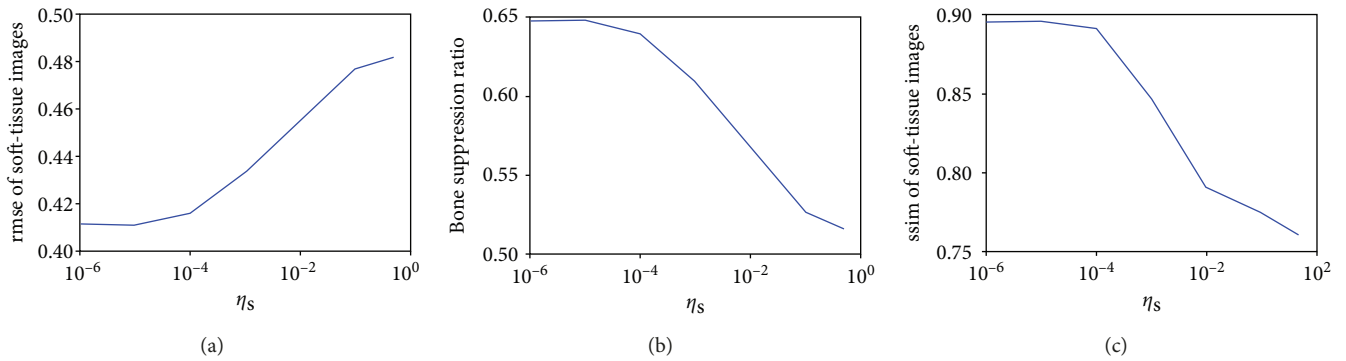
FIGURE 5: The effect on decomposition performance of parameter η_S for kernel density estimation.
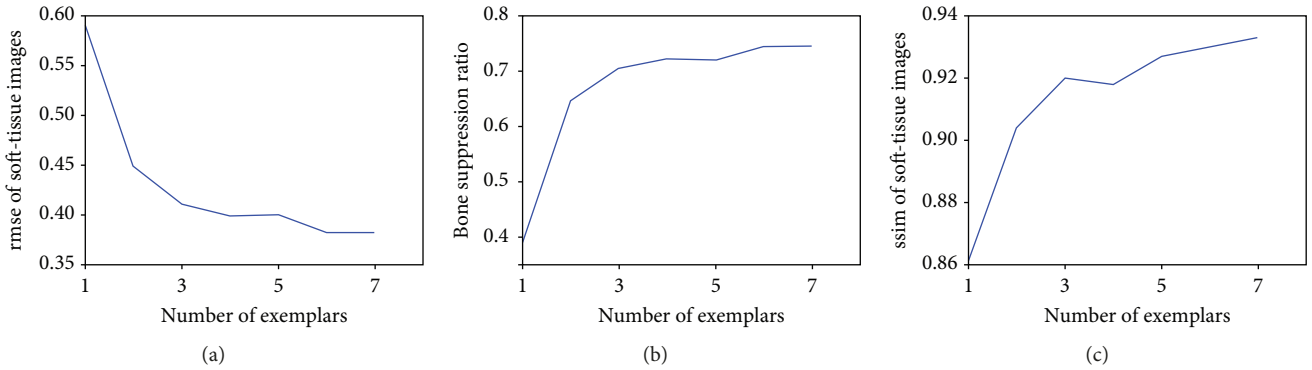
FIGURE 6: The effect on decomposition performance of the number (M).

M ($M = 5$). From Figure 5, we observed that the lower values of η_S and η_B led to better decomposition. In fact, the optimization of the log-sum-exp function tends to average the matched patches of each position when η_S and η_B have a low value. As the value of η_S and η_B increases, the optimization of the log-sum-exp function more closely approximates the min operation and the decomposed images looks sharper. However, the log-sum-exp functions with the large values of η_S or η_B also introduce artifacts in the decomposed images and results in worse decomposition performance. Based on these results, the parameters λ and η_S were set to 100 and 10^{-5} in the subsequent experiments, respectively.

The number of exemplars M is another crucial parameter for decomposition performance. Figure 6 shows that decomposition performance was improved significantly by increasing the number of exemplars. However, the computation cost of image matching and energy optimization would exponentially increase when many exemplars were used to construct the prior terms. As shown in Figure 6, the improvement in performance is relatively small when the number of exemplars is over 5. The number of exemplars M was set to 5 in subsequent experiments if M was not specified.

Some examples of decomposition results are illustrated in Figures 7–10. Figures 7 and 8 can be enlarged and viewed on
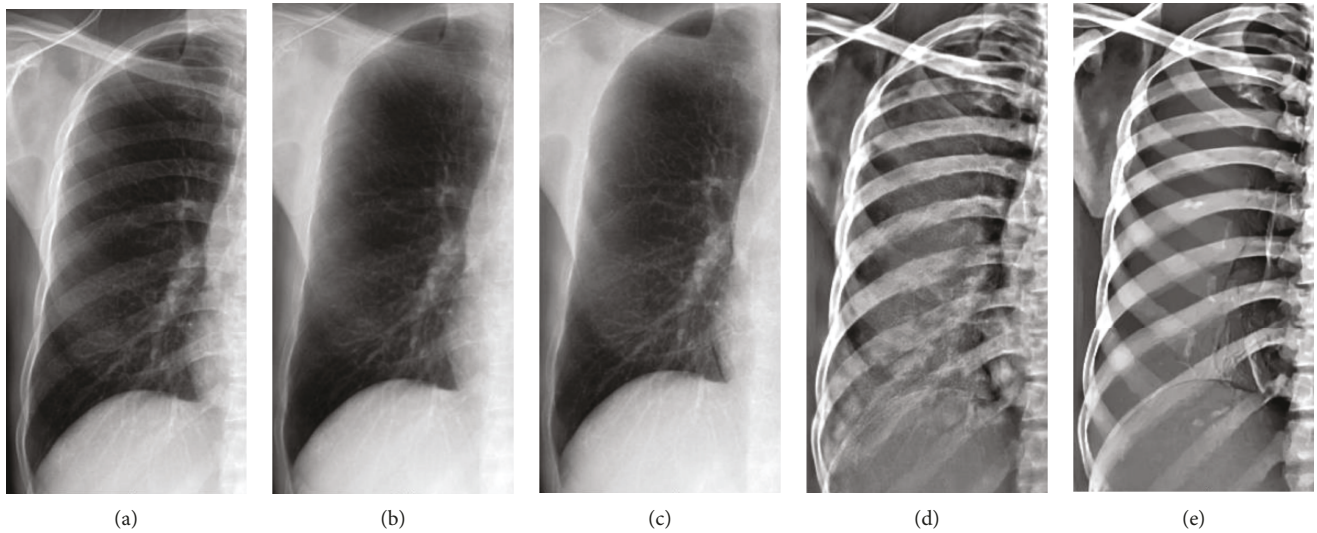
FIGURE 7: Decomposition results of a chest radiograph without motion artifacts: (a) the right lung field of a chest radiograph; (b) the decomposed soft tissue image; (c) the actual DES soft tissue image; (d) the decomposed bone image; (e) the actual DES bone image.
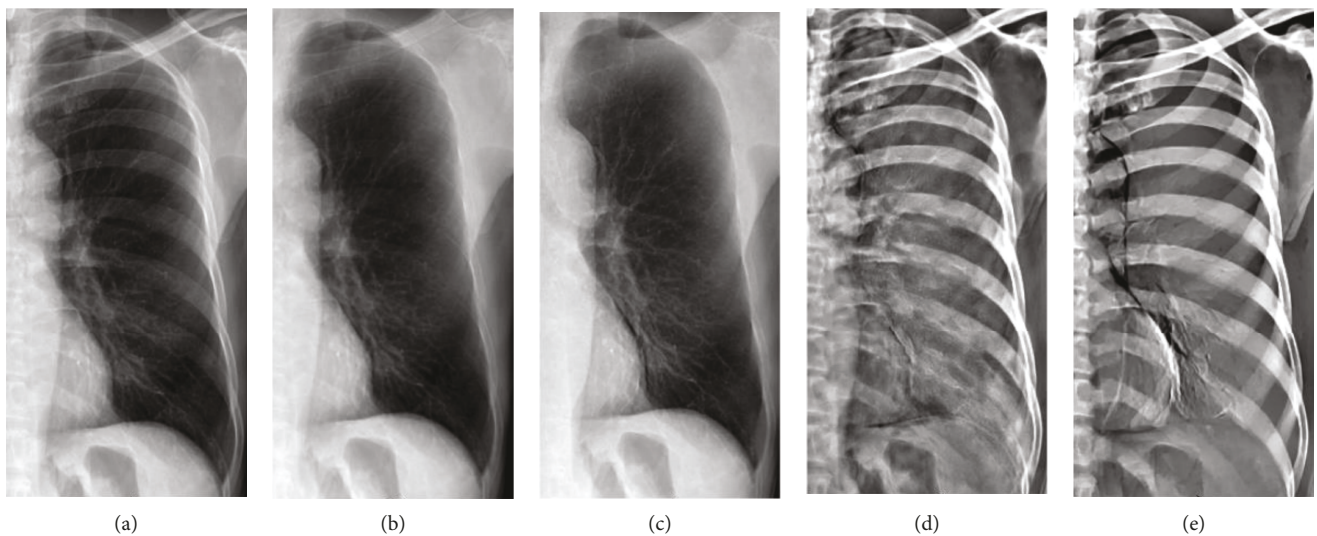
FIGURE 8: Decomposition results of a chest radiograph with motion artifacts: (a) the left lung field of a chest radiograph; (b) the reconstructed soft tissue image by use of our method; (c) the actual DES soft tissue image; (d) the reconstructed bone image by use of our method; (e) the actual DES bone image with obvious motion artifacts.

the screen for a better comparison. We observed that the ribs and clavicles are suppressed substantially and the visibility of the soft tissue is maintained in the reconstructed soft tissue images. Visually, the reconstructed soft tissue image and the actual image are similar. Comparing the reconstructed bone images with the actual bone images, some bone edges are more obscure where the bone edges are weak in the observed chest radiograph. In Figure 8, typical motion artifacts in the actual DES bone images were observed. Our decomposition method can reduce the motion artifacts to some extent, as shown in Figure 8(d), because of the smoothing effect of the weighted average of sampling patches. The use of the actual DES soft tissue and bone images with motion artifacts as the ground truth may lead to an overestimated reconstruction error. Figures 9 and 10 show examples

of decomposition results using different numbers of exemplars ($M = 1$, 3, and 5). Visual improvement of the estimated soft tissue and bone images is observed when more exemplars are used. Some block artifacts can be observed in the reconstructed soft tissue and bone images using fewer exemplars. These block artifacts were generated because of dissimilar patches in the exemplar chest radiographs for some patches in the input chest radiograph or mismatches between the patches. The selection of similar images as exemplars or using more exemplar images could ensure that each patch in the input chest radiograph has some possible similar patches in the exemplar images and could reduce the block artifacts and reconstruction error. As shown in Figure 9(c), the reconstructed soft tissue image is very similar to the corresponding DES soft tissue image shown in Figure 9(d), and

(a) $M = 1$, rmse = 0.46

(b) $M = 3$, rmse = 0.44

(c) $M = 5$, rmse = 0.41

(d) Ground truth

(e) Chest radiograph
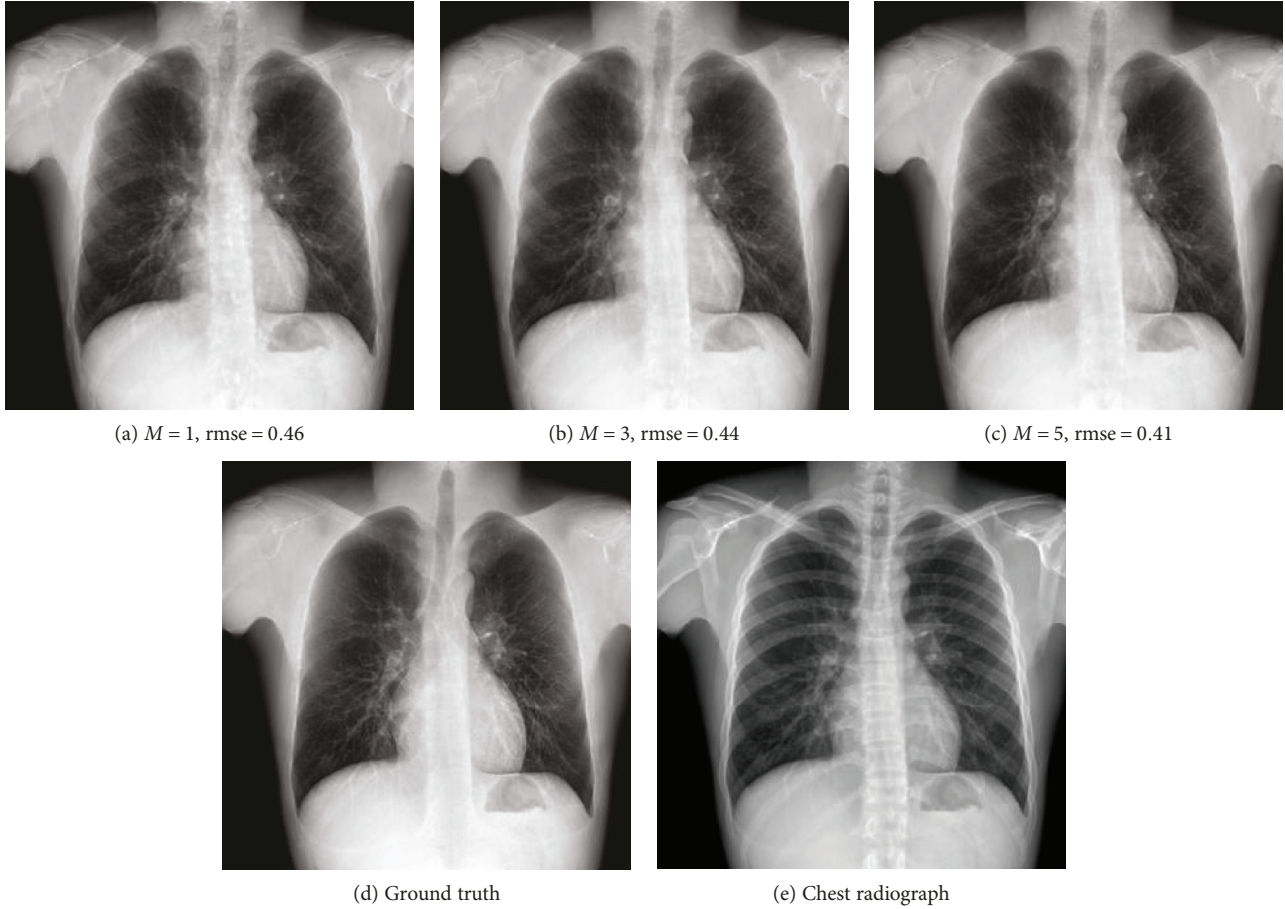
FIGURE 9: The reconstructed soft tissue images using the different numbers of exemplars. From left to right, the numbers of used exemplars (M) are 1, 3, and 5, respectively. rmse is the root mean squared error of the reconstructed soft tissue image. (a–c) are the reconstructed soft tissue images. (d) corresponds to the ground truth. The corresponding standard chest radiograph is (e).

the bone components of the corresponding chest radiograph shown in Figure 9(e) are substantially suppressed. In fact, the ssim index between Figures 9(c) and 9(d) is 0.915. A high ssim index indicates that most of the structures and details of the ground truth image are contained in the reconstructed image. Comparing Figure 9(c) with Figure 9(a), the bone component in Figure 9(c) is suppressed more completely than that in Figure 9(a). The decomposed bone image shown in Figure 10(c) looks clearer compared to that in Figure 10(a), which looks a little messy with fewer exemplars. With more exemplars, the reconstructed bone images show clearer rib edge and are more similar to the DES bone image shown in Figure 10(d).

We used our decomposition method to process the chest radiographs in the JSRT database which is the most commonly used database of chest radiographs for computer-aided detection and processing techniques [28]. Since the corresponding ground truth of the soft tissue and bone images of the JSRT database is unknown, the publicly available bone suppression results provided by Horvath [28] using the gradient modification method were used to be qualitatively compared with the results of our method. Figure 11 shows the decomposition results of two chest radiographs from the JSRT database. Visually, the reconstructed soft

tissue images of our method are more natural. When it is close to the thoracic edge, the soft tissue image reconstructed by the gradient modification method produced the shadows apparently. The two methods had advantages and disadvantages. The results of the gradient modification method depend on the segmentation of ribs and clavicles, which might be insensitive to the types of acquisition equipment of chest radiographs. However, the shadows of bones, which were not segmented, could not be removed. The results of our method depend on the appearance of the chest radiographs. Even if the images in the JSRT database are the scanned films and the number of DES exemplar is limited, our method could work well in most cases.

3.2. MAP Decomposition versus Locally Weighted Regression. Compared with the decomposition method that minimized the MAP energy function using the exemplar-based prior term, a more simple and direct method for estimating soft tissue and bone images is the weighted regression, which is analogous to label transfer [29]. Considering the sampling patches $\{p_i, i = 1, \cdots, M\}$ from the exemplar images based on the corresponding fields as the nearest neighbors, a soft tissue or bone image patch can be estimated by locally weighted regression as $\hat{\mathbf{p}} = \sum_{i=1}^{M} w_i \mathbf{p}_i$, where the weight w_i is

(a) $M = 1$, rmse = 0.46 (b) $M = 3$, rmse = 0.44 (c) $M = 5$, rmse = 0.41

(d) Ground truth (e) Chest radiograph
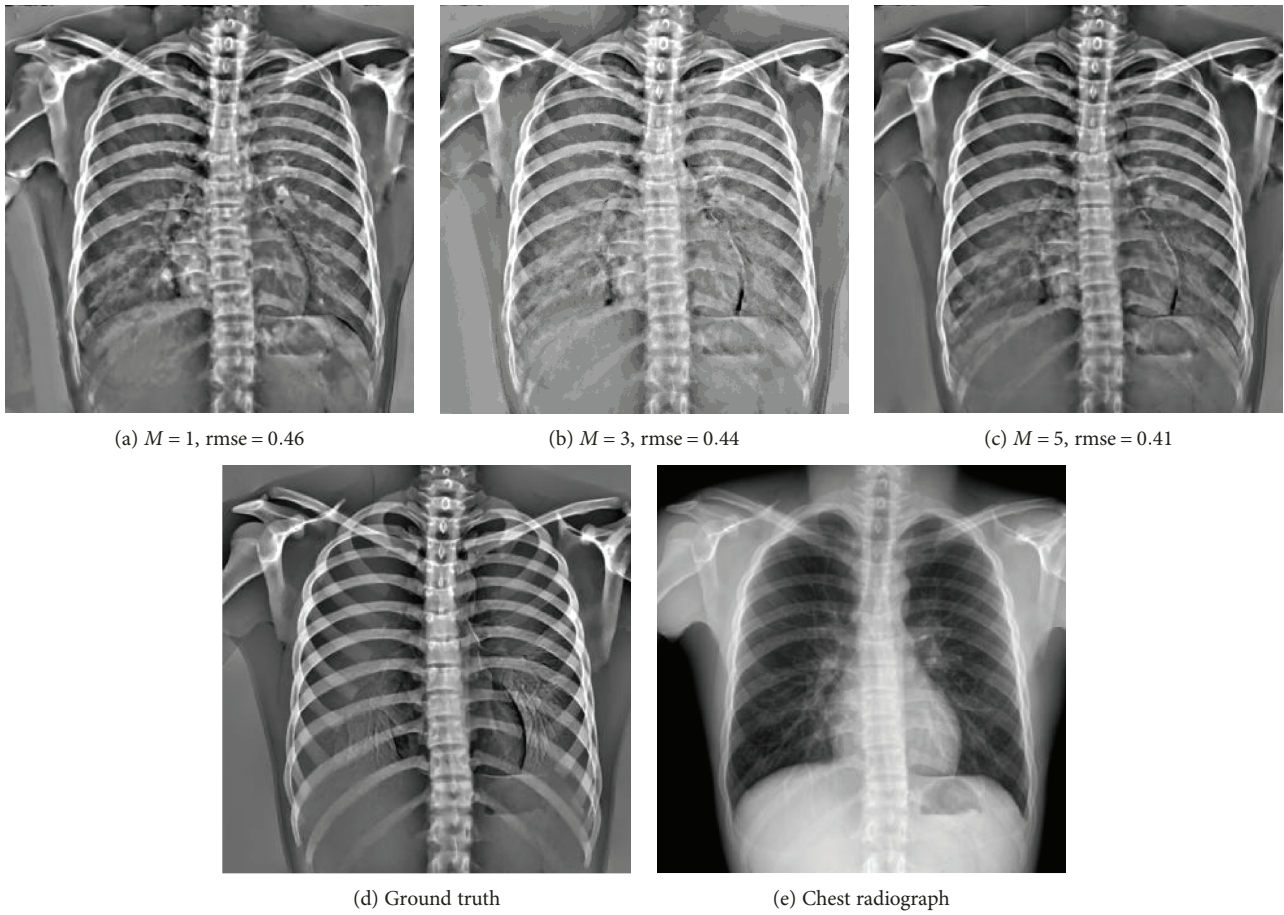
FIGURE 10: The reconstructed bone images using the different numbers of exemplars. From left to right, the numbers of used exemplars (M) are 1, 3, and 5, respectively. rmse is the root mean squared error of the reconstructed soft tissue image. (a–c) are the reconstructed bone images. (d) corresponds to the ground truth. The corresponding standard chest radiograph is shown in (e).

(a) (b) (c) (d) (e)
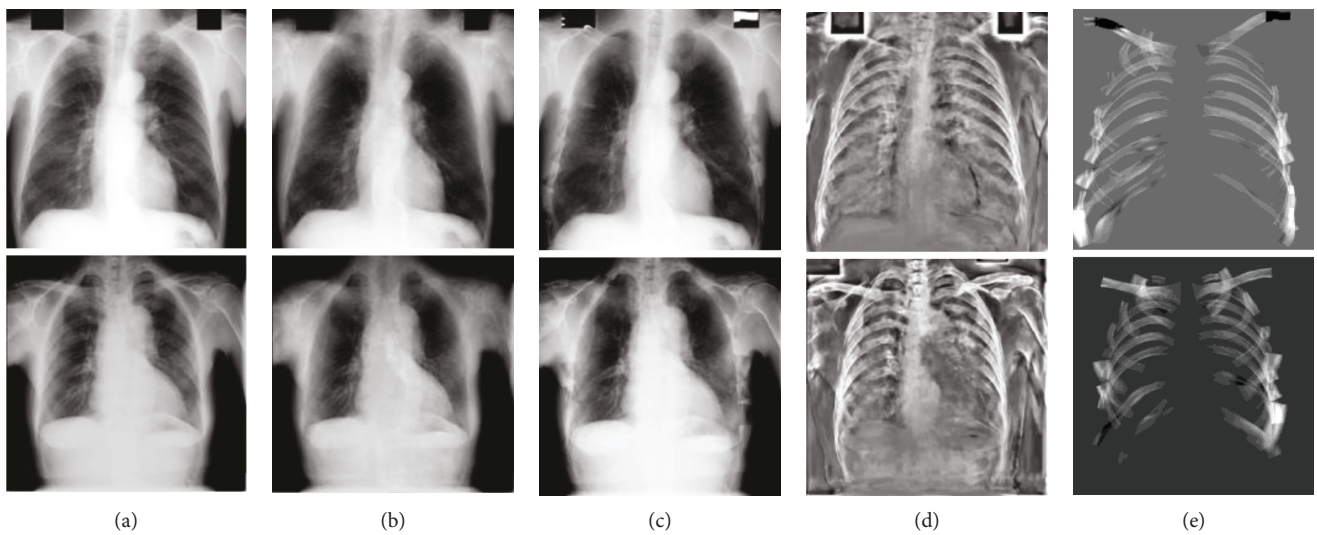
FIGURE 11: Decomposition results of two chest radiographs from the JSRT data set: (a) the original chest radiographs ("JPCLN063" and "JPCNN071"); (b) the reconstructed soft tissue images by the use of our method; (c) the bone-suppressed images by the use of the gradient modification method; (d) the reconstructed bone images by the use of our method; (e) the estimated bone structures by the use of the gradient modification method.

defined based on the matching error of the local descriptor. The result of locally weighted regression can be considered the minimum mean square estimation of the soft tissue or bone image patch. The entire soft tissue/bone image is reconstructed by rearranging all of the estimated patches. The locally weighted regression method is similar to the kNN regression method proposed by [7]. The main difference is the search method of kNN and the local descriptor used.

The mean and standard deviation of performance measures for MAP decomposition and locally weighted regression are listed in Table 1. From the results shown in Table 1, our method is significantly superior to the locally weighted regression. rmse is computed on the normalized soft tissue and bone images. The MAP decomposition method yields a lower rmse and a higher bone suppression ratio than the locally weighted regression. The values of the ssim of the reconstructed soft tissue images by two methods are 0.927 and 0.846, respectively. The high ssim indicates that the detail structures in the DES soft tissue image are preserved by two decomposition methods. Since the intensity variations of soft tissue images are significantly larger than those of bone images, the ssim of the reconstructed bone image is lower than the ssim of the reconstructed soft tissue images.

The decomposition results of a chest radiograph by the use of the MAP model and the locally weighted regression method are shown in Figure 12. The soft tissue images and bone images reconstructed by the MAP model in Figure 12 are visually much closer to the ground truth than that by the locally weighted regression method. And the reconstruction errors (rmse) of the soft tissue image estimated by the MAP model and the locally weighted regression are 0.41 and 0.44, respectively. Actually, the optimization of the MAP energy function with the data term tends to satisfy the constraint $Y = S + B$ and utilizes more information on the input chest radiograph to reduce the reconstruction error and generate higher fidelity results. By contrast, the locally weighted regression cannot ensure that $\|Y - S - B\|^2$ can be minimized definitely. Thus, the locally weighted regression can only yield worse estimation of the soft tissue and bone images than the MAP decomposition.

4. Discussion

In our MAP decomposition model, the prior terms are rendered in the log-sum-exp format. For small values of the parameter η_S or η_B, the prior terms can be considered the approximations to the averaging function of quadratic errors between image patches. From the experimental results, we observed that the small values of the parameter η_S or η_B could lead to better decomposition results of the chest radiograph in terms of the three performance measures. The optimal values of η_S and η_B can be dependent on the data set and the performance measures. It is interesting to investigate the other forms of the prior term using other kernel functions for density estimation or the robust loss functions as prior terms for decomposition. Combining the exemplar-based priors, the general image priors, such as total variation [11] and sparsity [30], would be helpful in further improving the

TABLE 1: The average performance of MAP decomposition and locally weighted regression on the validation set with 100 standard chest radiographs. bsr denotes the bone suppression ratio. rmse-S and ssim-S denote the root mean squared error (rmse) and the structural similarity image measure (ssim) for the reconstructed soft tissue, respectively.

Method	bsr	rmse-S	ssim-S
MAP decomposition	0.715	0.414	0.927
Weighted regression	0.704	0.441	0.846

decomposition model. Additionally, some methods on image quality improvement can be considered to further enhance the algorithm performance, such as convolution network-based processing [31], fuzzy similarity-based method [32], and sparse coding-based processing [33–35].

The basis of our method is the database of DES radiographs, which is used to estimate image priors. In theory, the estimation accuracy of image (patch) prior probability depends on the samples. However, even the soft tissue and bone components cannot be separated perfectly through using a DES system. Furthermore, a few motion artifacts are present in the soft tissue and bone images of two-exposure DES as a result of cardiac motion and breath. The soft tissue and bone components were also not successfully separated in the regions with motion artifacts. In this work, we acquired enough DES radiographs from Nanfang Hospital, Guangzhou, China, which is useful for that similar patches, for a patch in the source chest image can be found in the selected exemplars of the training set more possibly. From the experimental results, larger λ (weight of the data term) can lead to better decomposition in terms of the three performance measures. The data term had substantial contributions to decomposition performance, and the MAP decomposition model was effective for the separation of bone images from the chest radiographs. But this does not indicate that the prior terms are not helpful for decomposition since the decomposition results can be extremely arbitrary and meaningless without the prior terms. Actually, the decomposed soft tissue image S and bone image B only tend to satisfy the constraint $Y = S + B$ when the parameter λ becomes very large.

One bottleneck of our method is the large computation cost mainly because of dense matching between chest radiographs. Although the local descriptors and BoW histograms of the images in the database have been computed off-line and restored, the running time of our method (135.8 s per image of 512×512 pixels) is still longer than that of MTANN regression (1.63 s per image of 512×512 pixels). Actually, with the popularity of convolutional neural networks (CNN), we also proposed a cascade architecture of CNN (called CamsNet) [36] to improve the results of our MAP model and reach a better result.

The ultimate goal of decomposition or bone suppression of chest radiographs is to improve the performance of radiologists in diagnosing lung diseases. But this ultimate goal cannot be realized directly. Considering that the usefulness of DES soft tissue images had been proved, our decomposition

(a)

(b)

(c)

(d)

(e)

(f)

(g)
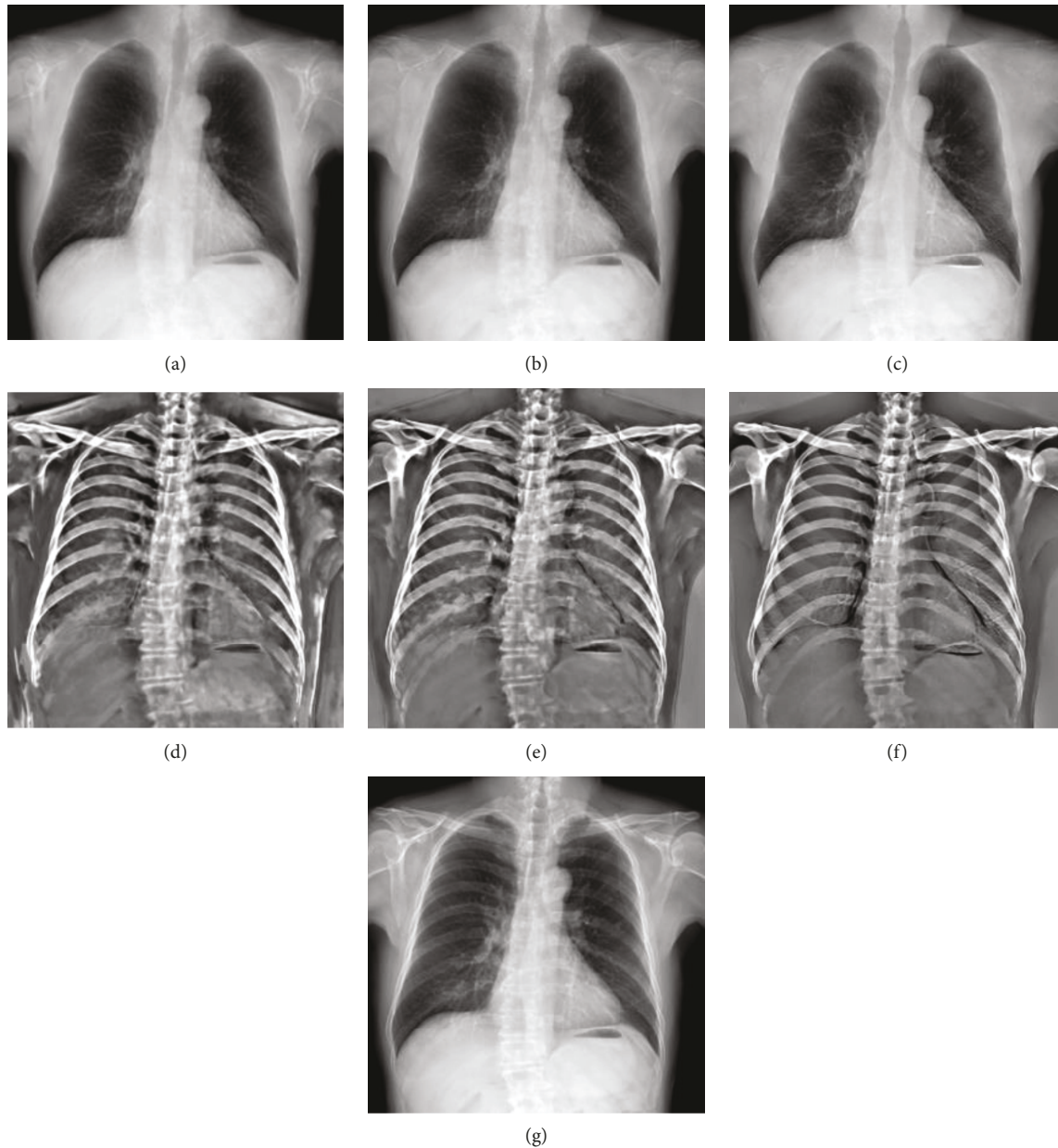
FIGURE 12: Comparison of the decomposition results through the MAP model and the locally weighted regression method: (a) the reconstructed soft tissue image through the locally weighted method; (b) the decomposed soft tissue image through the MAP model; (c) the DES soft tissue image of (g); (d) the reconstructed bone image through the locally weighted method; (e) the decomposed bone image through the MAP model; (f) the DES bone image of (g); (g) the standard chest radiograph.

method is aimed at producing the decomposition results similar to the DES soft tissue and bone images as possible. A very small reconstruction error (e.g., rmse) and a very high bone suppression ratio may indicate indirectly the useful decomposition results. However, preserving the details in the abnormal regions and enhancing the contrast of the nodules are important. The data (fidelity) term in the MAP decomposition model can provide a trade-off to balance structure preserving and smoothing. It would be helpful to integrate some general image priors, such as total variation, sparsity, or low rank for bone images with the MAP model. The decomposed bone image would be smoother, and more details of the input chest radiograph would be maintained in the decomposed soft tissue image. The detectability of nodules in the decomposed soft tissue images can be further improved by designing the decomposition energy functions using a certain probability of abnormality detection or optimizing the local descriptors for reducing the mismatches of image patches in abnormal regions. And a more specific nodule detection algorithm should be also developed for the decomposed soft tissue images. Furthermore, the usefulness of our decomposition results for improving the performance of radiologists in diagnosing lung diseases will be investigated in the future.

5. Conclusions

We presented a decomposition method of chest radiographs using the exemplar-based nonparametric priors of soft tissue and bone images. Using the real DES radiographs as the exemplars of a chest radiograph for decomposition, the nonparametric priors of the soft tissue and bone images were estimated on the samples of image patches, which were sampled based on dense matching of chest radiographs. Integrating the nonparametric priors into a MAP model, the soft tissue and bone images were reconstructed by minimizing the energy function with the proposed efficient optimization algorithm. Our method could produce soft tissue and bone images like the real DES system but only needed a single conventional chest radiograph as the input. Experiments on synthetic DES radiography and the JSRT database showed that our method could be used to suppress the bone structures in the chest radiographs, which would be potentially useful for radiologists to diagnose lung diseases in chest radiographs.

Data Availability

The image data used in this study were collected from two data sets. The first data set consisted of posterior-anterior DES chest radiographs acquired with a DES system (Revolution XR/d, GE) at Nanfang Hospital, Guangzhou, China, and so cannot be made freely available. The second one was the publicly available Japanese Society of Radiological Technology (JSRT) data set.

Conflicts of Interest

The authors have no relevant conflicts of interest to disclose.

Authors' Contributions

Yunbi Liu and Wei Yang contributed equally to this work.

Acknowledgments

References

[1] P. K. Shah, J. H. M. Austin, C. S. White et al., "Missed non–small cell lung cancer: radiographic findings of potentially resectable lesions evident only in retrospect," *Radiology*, vol. 226, no. 1, pp. 235–241, 2003.

[2] P. Vock and Z. Szucs-Farkas, "Dual energy subtraction: principles and clinical applications," *European Journal of Radiology*, vol. 72, no. 2, pp. 231–237, 2009.

[3] K. Suzuki, H. Abe, H. MacMahon, and K. Doi, "Image-processing technique for suppressing ribs in chest radiographs by means of massive training artificial neural network (MTANN)," *IEEE Transactions on Medical Imaging*, vol. 25, no. 4, pp. 406–416, 2006.

[4] S. Oda, K. Awai, K. Suzuki et al., "Performance of radiologists in detection of small pulmonary nodules on chest radiographs: effect of rib suppression with a massive-training artificial neural network," *American Journal of Roentgenology*, vol. 193, no. 5, pp. W397–W402, 2009.

[5] F. Li, R. Engelmann, L. Pesce, S. G. Armato, and H. MacMahon, "Improved detection of focal pneumonia by chest radiography with bone suppression imaging," *European Radiology*, vol. 22, no. 12, pp. 2729–2735, 2012.

[6] S. Chen and K. Suzuki, "Computerized detection of lung nodules by means of "virtual dual-energy" radiography," *IEEE Transactions on Biomedical Engineering*, vol. 60, no. 2, pp. 369–378, 2013.

[7] M. LOOG, B. VANGINNEKEN, and A. SCHILHAM, "Filter learning: application to suppression of bony structures from chest radiographs," *Medical Image Analysis*, vol. 10, no. 6, pp. 826–840, 2006.

[8] T. Rasheed, B. Ahmed, M. A. Khan, M. Bettayeb, S. Lee, and T.-S. Kim, "Rib suppression in frontal chest radiographs: a blind source separation approach," *2007 9th International Symposium on Signal Processing and Its Applications*, 2007, pp. 1–4, Sharjah, United Arab Emirates, Feb. 2007.

[9] G. Simkó, G. Orbán, P. Máday, and G. Horváth, "Elimination of clavicle shadows to help automatic lung nodule detection on chest radiographs," in *4th European Conference of the International Federation for Medical and Biological Engineering*, pp. 488–491, Springer, Berlin, Heidelberg, 2009.

[10] L. Hogeweg, C. I. Sanchez, and B. van Ginneken, "Suppression of translucent elongated structures: applications in chest radiography," *IEEE Transactions on Medical Imaging*, vol. 32, no. 11, pp. 2099–2113, 2013.

[11] S. Osher, A. Sole, and L. Vese, "Image decomposition and restoration using total variation minimization and the H^1," *Multiscale Modeling & Simulation*, vol. 1, no. 3, pp. 349–370, 2003.

[12] A. Levin and Y. Weiss, "User assisted separation of reflections from a single image using a sparsity prior," *IEEE Transactions on Pattern Analysis and Machine Intelligence*, vol. 29, no. 9, pp. 1647–1654, 2007.

[13] J. Bobin, J.-L. Starck, J. M. Fadili, Y. Moudden, and D. L. Donoho, "Morphological component analysis: an adaptive thresholding strategy," *IEEE Transactions on Image Processing*, vol. 16, no. 11, pp. 2675–2681, 2007.

[14] M. F. Tappen and C. Liu, "A Bayesian approach to alignment-based image hallucination," in *Computer Vision – ECCV 2012*, pp. 236–249, Springer, Berlin, Heidelberg, 2012.

[15] C. Liu, J. Yuen, A. Torralba, J. Sivic, and W. T. Freeman, "Sift flow: dense correspondence across different scenes," in *Computer Vision – ECCV 2008*, pp. 28–42, Springer, Berlin, Heidelberg, 2008.

[16] J. Kim, C. Liu, F. Sha, and K. Grauman, "Deformable spatial pyramid matching for fast dense correspondences," *Proceedings of the IEEE Conference on Computer Vision and Pattern*

Recognition, 2013, pp. 2307–2314, Portland, OR, USA, June 2013.

[17] A. Agrawal, R. Raskar, and R. Chellappa, "Edge suppression by gradient field transformation using cross-projection tensors," *2006 IEEE Computer Society Conference on Computer Vision and Pattern Recognition (CVPR'06)*, 2006, pp. 2301–2308, New York, NY, USA, June 2006.

[18] K. He, J. Sun, and X. Tang, "Guided image filtering," in *European Conference on Computer Vision*, pp. 1–14, Springer, Berlin, Heidelberg, 2010.

[19] M. Varma and A. Zisserman, "A statistical approach to texture classification from single images," *International journal of computer vision*, vol. 62, no. 1-2, pp. 61–81, 2005.

[20] D. G. Lowe, "Distinctive image features from scale-invariant keypoints," *International Journal of Computer Vision*, vol. 60, no. 2, pp. 91–110, 2004.

[21] G. Csurka, C. Dance, L. Fan, J. Willamowski, and C. Bray, "Visual categorization with bags of keypoints," *Workshop on statistical learning in computer vision, ECCV*, vol. 1, no. 1-22, pp. 1-2, 2004.

[22] S. Lazebnik, C. Schmid, and J. Ponce, "Beyond bags of features: spatial pyramid matching for recognizing natural scene categories," in *2006 IEEE Computer Society Conference on Computer Vision and Pattern Recognition (CVPR'06)*, pp. 2169–2178, New York, NY, USA, June 2006.

[23] Y. Rubner and C. Tomasi, "Texture-based image retrieval without segmentation," in *Proceedings of the Seventh IEEE International Conference on Computer Vision*, pp. 1018–1024, Kerkyra, Greece, Greece, Sept. 1999.

[24] C. Barnes, E. Shechtman, D. B. Goldman, and A. Finkelstein, "The generalized patchmatch correspondence algorithm," in *Computer Vision – ECCV 2010*, pp. 29–43, Springer, Berlin, Heidelberg, 2010.

[25] R. Wolke and H. Schwetlick, "Iteratively reweighted least squares: algorithms, convergence analysis, and numerical comparisons," *SIAM Journal on Scientific and Statistical Computing*, vol. 9, no. 5, pp. 907–921, 1988.

[26] A. Vedaldi and B. Fulkerson, "VLFeat: an open and portable library of computer vision algorithms," in *Proceedings of the 18th ACM international conference on Multimedia*, pp. 1469–1472, ACM New York, NY, USA, October 2010.

[27] Z. Wang, A. C. Bovik, H. R. Sheikh, and E. P. Simoncelli, "Image quality assessment: from error visibility to structural similarity," *IEEE Transactions on Image Processing*, vol. 13, no. 4, pp. 600–612, 2004.

[28] G. Horvath, 2013, http://www.mit.bme.hu/eng/events/2013/04/18/bone-shadow-eliminated-images-jsrt-database.

[29] C. Liu, J. Yuen, and A. Torralba, "SIFT flow: dense correspondence across scenes and its applications," *IEEE Transactions on Pattern Analysis and Machine Intelligence*, vol. 33, no. 5, pp. 978–994, 2011.

[30] S. Roth and M. J. Black, "Fields of experts," *International Journal of Computer Vision*, vol. 82, no. 2, pp. 205–229, 2009.

[31] W. Yang, H. Zhang, J. Yang et al., "Improving low-dose CT image using residual convolutional network," *IEEE Access*, vol. 5, pp. 24698–24705, 2017.

[32] Y. Chen, Y. Zhang, H. Shu et al., "Structure-adaptive fuzzy estimation for random-valued impulse noise suppression," *IEEE Transactions on Circuits and Systems for Video Technology*, vol. 28, no. 2, pp. 414–427, 2018.

[33] J. Liu, Y. Hu, J. Yang et al., "3D feature constrained reconstruction for low-dose CT imaging," *IEEE Transactions on Circuits and Systems for Video Technology*, vol. 28, no. 5, pp. 1232–1247, 2018.

[34] J. Liu, J. Ma, Y. Zhang et al., "Discriminative feature representation to improve projection data inconsistency for low dose CT imaging," *IEEE transactions on medical imaging*, vol. 36, no. 12, pp. 2499–2509, 2017.

[35] Y. Chen, L. Shi, Q. Feng et al., "Artifact suppressed dictionary learning for low-dose CT image processing," *IEEE Transactions on Medical Imaging*, vol. 33, no. 12, pp. 2271–2292, 2014.

[36] W. Yang, Y. Chen, Y. Liu et al., "Cascade of multi-scale convolutional neural networks for bone suppression of chest radiographs in gradient domain," *Medical Image Analysis*, vol. 35, pp. 421–433, 2017.

Research Article

Biomechanical Analysis of the Forces Exerted during Different Occlusion Conditions following Bilateral Sagittal Split Osteotomy Treatment for Mandibular Deficiency

Yuan-Han Chang [ID],[1] **Man-Yee Chan** [ID],[1,2] **Jui-Ting Hsu** [ID],[3] **Han-Yu Hsiao** [ID],[1] **and Kuo-Chih Su** [ID][4,5]

[1]*Department of Stomatology, Taichung Veterans General Hospital, Taichung, Taiwan*
[2]*School of Dentistry, College of Oral Medicine, Chung Shan Medical University, Taichung, Taiwan*
[3]*School of Dentistry, College of Medicine, China Medical University, Taichung, Taiwan*
[4]*Department of Biomedical Engineering, Hung Kuang University, Taichung, Taiwan*
[5]*Department of Medical Research, Taichung Veterans General Hospital, Taichung, Taiwan*

Correspondence should be addressed to Kuo-Chih Su; kcsu@vghtc.gov.tw

The bilateral sagittal split osteotomy (BSSO) technique is commonly used to correct mandibular deficiency. If the patient is exposed to excessive external forces after the procedure, occlusal changes or nonunion may occur. However, previous studies only focused on single external forces on the mandible and did not conduct relevant research on the forces exerted by different occlusion conditions. The main purpose of this study was to use finite element analysis methods to determine the biomechanics of four common occlusion conditions after BSSO surgical treatment. This study constructed a finite element analysis computer model of a miniplate implanted in the lower jaw. The structure of the model consisted of the mandible, miniplate, and screws. In addition, external forces were applied to the superficial masseter, deep masseter, medial pterygoid, anterior temporalis, middle temporalis, and posterior temporalis muscles to simulate the incisal clench, intercuspal position (ICP), right unilateral molar clench (RMOL), and right group function occlusion conditions. Subsequently, this study observed the effects of these conditions on the miniplate, screws, and mandible, including the von Mises stress values. The results showed that all of the different occlusion conditions that this study evaluated placed high stress on the miniplate. In the ICP and RMOL occlusion conditions, the overall mandibular structure experienced very high stress. The screw on the proximal segment near the bone gap experienced high stress, as did the screw on the buccal side. According to the present analysis, although the data were not directly obtained from clinical practice, the finite element analysis could evaluate the trend of results under different external forces. The result of this study recommended that patients without intermaxillary fixation avoid the ICP and RMOL occlusion conditions. It can be used as a pilot study in the future for providing clinicians more information on the biomechanics of implantation.

1. Introduction

In oral surgery clinics, malocclusion and associated facial bone deformities are common and primarily affect the appearance and occlusion of patients. According to previous studies, mandibular deficiency is a common phenomenon, particularly in developing adolescents, with a worldwide prevalence of 1.1-21.5% [1]. To correct mandibular deficiency, mandibular advancement is often performed via intraoral vertical ramus osteotomy (IVRO) and bilateral sagittal split osteotomy (BSSO) [2]. In IVRO, a vertical incision is made in the ramus, which divides the mandible into two parts (anterior and posterior), thereby moving the mandible to achieve a reduction effect. The advantage of IVRO is that

the operation is simple and fast. However, a disadvantage is that internal fixation of the mandible cannot be achieved with artificial bone screws, and thus, bone healing must be assisted by intermaxillary fixation. Therefore, patients cannot open their mouths for about 6 to 8 weeks after surgery [3]. As for BSSO, the horizontal cutting line is located above the medial side of the ramus and above the lingua, while the vertical cutting line is located at the distal side of the second molar on the lateral side of the mandible. Next, the two cutting lines are connected along the external oblique ridge. After cutting, the mandible is divided into two parts, a proximal segment and a distal segment, and fixed with miniplates. One advantage of BSSO over IVRO is that the bone has a larger contact area and higher stability. In addition, both mandibular advancement and setback can be achieved with BSSO surgery, as desired. Therefore, mandibular advancement with BSSO is the more common approach for treating mandibular deficiency [4]. Clinically, intermaxillary fixation for several days to weeks after mandibular orthognathic surgery can be performed. However, some physicians prefer to maintain an open airway for the patient after surgery and thus decide against intermaxillary fixation [5]. Consequently, if the mandible without intermaxillary fixation experiences excessive external forces, then changes in occlusion or poor bone healing may occur.

Previously, researchers have used biomechanical methods to evaluate the postoperative efficacy of BSSO. For instance, Hadi et al. [6] performed a general biomechanical analysis of bicortical screws in the mandible. Although their study did not investigate the effects after BSSO surgery, their research methods can be used as a reference framework for performing biomechanical experiments following BSSO surgery. Additionally, Nieblerová et al. [7] and Olivera et al. [8] used minipig and sheep mandibles to investigate the biomechanics of different BSSO reductions. However, the study samples were primarily animal based, and thus, the results of the study may not accurately reflect the situation in the human body. Oguz et al. [9] used a unilateral artificial pseudobone mandibular model to investigate the biomechanical effects of different plate reset patterns through biomechanical methods. Ribeiro-Junior et al. [10] used a similar approach to investigate the effects of different BSSO techniques, revealing that the locking miniplate approach had relatively better stability. Although locking miniplates have a good fixation effect, the prominent plate profile will not be accepted by patients. Therefore, facial bone fixation is still primarily based on miniplates. It should be noted that these studies mainly used in vitro biomechanics to investigate the effects of BSSO surgery, and as such, the external forces applied can only be simulated by a simple, single external force and the effects of muscles on actual chewing cannot be considered. Therefore, it is difficult for the results of in vitro studies to reflect the actual situation of different occlusion movements in human.

With advances in computer technology, finite element analysis has become a commonly used analytical method in the field of dental biomechanics because it can be used to simulate the biomechanics of different structures, materials, and force patterns. A prior study used finite element analysis

to investigate the efficacy of different reconstruction methods for the treatment of mandibular defects [11]. Additionally, other researchers have used finite element analysis to investigate various BSSO fixation methods and the effects of different materials (absorbable materials) on the strength and mechanics of fixation [12]. For instance, Erkmen et al. [13] investigated the effects of using miniplates and different fixation methods for advancement surgery, while another study evaluated whether locking miniplates have sufficient strength to complete internal fixation of the mandible [14]. Although many previous studies have used finite element analysis to investigate the biomechanical effects of BSSO fixation and provide recommendations to clinicians, most of the simulated models have been unilateral, the overall mandibular models are incomplete, and the applied external forces are simple, single external forces; hence, the simulated results likely do not reflect the actual conditions. Further, finite element analysis has been employed to investigate the effects of different external forces on implanted artificial total temporomandibular joints, focusing on the incisal clench (INC), intercuspal position (ICP), right unilateral molar clench (RMOL), left unilateral molar clench, right group function (RGF), and left group function occlusion conditions [15]. Therefore, the loading conditions and boundary conditions outlined in the present study will provide a reference for researchers in different occlusion conditions.

As mentioned above, prior studies have demonstrated that BSSO surgery is commonly used to treat mandibular deficiency. However, because most previous in vitro studies used a single external force, the effects of these forces on miniplates under different occlusion conditions cannot be easily measured, and thus, they remain unclear. Hence, the main purpose of this study was to use finite element analysis methods to simulate external forces from the mandibular muscles and investigate the effects of these forces on miniplate implantation under four common occlusion conditions. The results of this study will provide clinicians with mechanical references for different occlusion forces in the overall mandibular structure and miniplate after miniplate implantation in BSSO surgeries, ultimately helping clinicians to avoid surgical failure due to different occlusion conditions.

2. Materials and Methods

2.1. Building a Simulation Geometry Model. This study was designed to investigate the effects of four different occlusion conditions on the miniplate. To do this, this study constructed a finite element analysis computer model of the mandible with the miniplate. The models used in this study included four components, namely, the cortical bone of the mandible, cancellous bone, miniplate, and screws (Figure 1). The appearance of this study-constructed model was based on models of the mandible in previous studies [15], which were primarily composed of cortical bone and cancellous bone. The mandible model established in this study imports the CT images of the mandible to Mimics (Mimics Medical 19.0, Materialise, Leuven, Belgium), selects the peripheral contour of the mandibular cortical bone in Mimics using circles, and retracts the whole model by 2 mm to establish
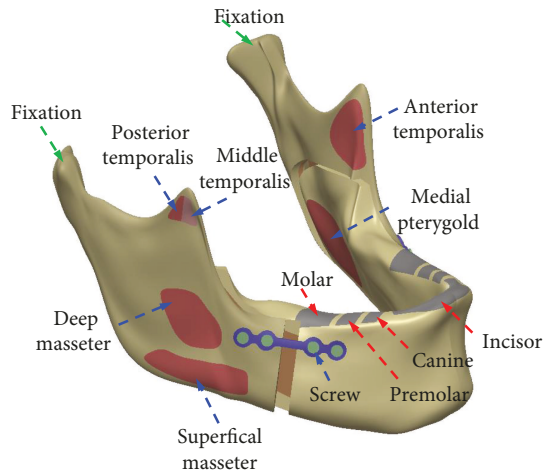
Figure 1: Finite element analysis models and sites experiencing muscular forces in the present study.

the contour of the cancellous bone structure. This study employed three-dimensional computer-aided design software (SOLIDWORKS 2016; Dassault Systemes SOLIDWORKS Corp., Waltham, MA, USA) for creating and modifying the computer model. The peripheral contours of mandibular cortical and cancellous bones are imported to SOLIDWORKS, and the complete solid model of mandibular cortical bone and cancellous bone is established using the loft function of SOLIDWORKS software. The computer model of the mandible was cut as described in previous studies [10], to simulate the treatment of mandibular deficiency by BSSO surgery. The distal segment was moved outward by 4 mm. In addition, the computer-aided design software SOLIDWORKS was used to combine two miniplates and eight screws (the sites and numbering of the eight different screws are shown in Figure 2(a)). After the three-dimensional computer model was constructed, it was imported into the finite element analysis software (ANSYS Workbench 19.0; ANSYS Inc., Canonsburg, PA, USA) for analysis.

2.2. Loading Conditions and Boundary Conditions. This study investigated four different occlusal conditions commonly found in clinical practice, namely, INC, ICP, RMOL, and RGF. Of these conditions, INC primarily simulated contact of the incisal edges, ICP simulated maximum intercuspation of the posterior teeth, RMOL simulated contact of the right (unilateral) posterior teeth, and RGF simulated lateral movement of the right posterior dentition. In finite element analysis, different boundary conditions and loading conditions must be provided based on these four different occlusion conditions. This study based the external force data and application methods on those used in previous studies [15, 16]. For the boundary conditions, the condyle was set as a fixed node and the displacement setting method was used to fix the x-, y-, and z-axis displacements to 0, which allows this point to rotate freely. For the loading conditions, external forces were applied to the superficial masseter (SM), deep masseter (DM), medial pterygoid (MP), anterior temporalis (AT), middle temporalis (MT), and posterior

temporalis (PT) muscles (Figure 1). The magnitude and direction of the external forces are shown in Table 1. In addition, fixation was applied at the incisor, canine, premolar, and molar tooth positions in the different occlusion conditions, as shown in Table 1. The sites of contact between the miniplate and screws and between the miniplate and mandible were set to "no separation," primarily to simulate the lack of separation between these surfaces, but also to allow for slight, frictionless sliding.

2.3. Material Properties of the Model. The research model was composed of four parts, namely, the cortical bone, cancellous bone, miniplate, and screws. The material properties used in this study were obtained from previous studies [17]. Table 2 shows the material properties in this study simulation. All materials were assumed to be homogeneous, isotropic, and linear elastic. Two independent parameters, i.e., Young's modulus (E) and Poisson's ratio (ν), were used to characterize the properties of the materials. The simulated miniplate material was composed primarily of titanium alloy. The bones were divided into the cortical bone and cancellous bone. Moreover, all of the finite element analysis computer models in this study used tetrahedral meshes (Figure 2(b)). The software used for mesh in this study was ANSYS Workbench 19.0. After the meshes passed the convergence test, all models reached the 5% stop criteria of the convergence test [18, 19]. The numbers of nodes and meshes were 144,969 and 74,878, respectively. Therefore, the finite element mesh model used herein to investigate the effects of different occlusion conditions on miniplate implantation was reasonable.

Following finite element analysis, this study utilized the von Mises stress values as an observational index. The von Mises stress distributions of the miniplate, eight screws, and mandibular screw positions on the left and right sides of the mandible were observed to investigate the biomechanical effects of the four different occlusion conditions after BSSO treatment for mandibular deficiency.

3. Results

After finite element analysis, this study obtained the overall stress distributions on the mandible under the four different occlusion conditions, as shown in Figure 3. This figure reveals that high stress occurred at the miniplate under all four occlusion conditions. The mandibular stress was particularly high in the ICP and RMOL conditions.

Figure 4 shows the stress distributions on the left and right miniplates under the four occlusion conditions. High stress primarily occurred in the region between the miniplates (the bone gap at the mandibular joint), especially at the site of the screw in the proximal segment and at the corner of the miniplate in the distal segment. Among the four conditions, the ICP and RMOL conditions in particular put high stress on the miniplate. Table 3 shows the maximum von Mises stress values for the miniplates in the four different occlusion conditions.

Figure 5 shows the stress distributions on the eight screws used for miniplate fixation (screw positions numbered as shown in Figure 2(a)). High stress was mainly observed at
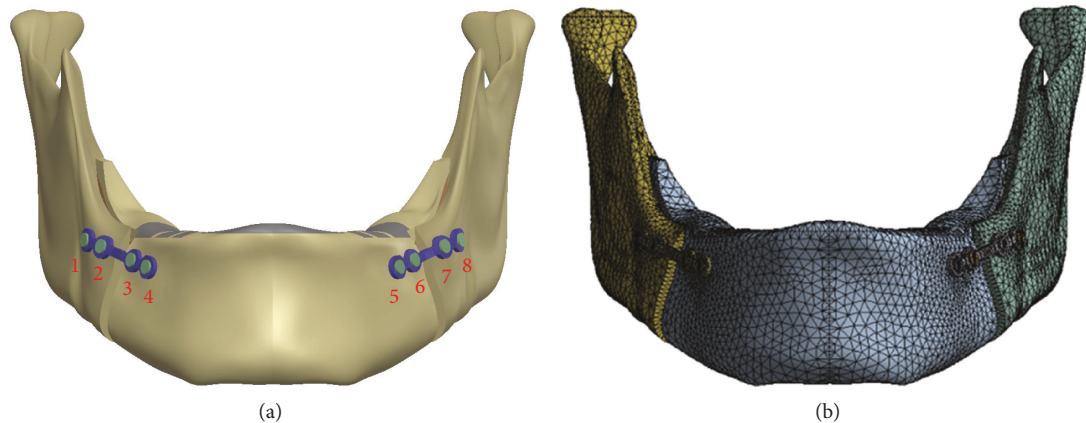
FIGURE 2: (a) Sites and numbers of the different screws after mandibular miniplate implantation. (b) Mesh of the computer model used in the present study.

the junction of the miniplate and screws. Among the four occlusion conditions, higher stress on the screws was observed under the ICP and RMOL conditions, especially near the junction of the screws and miniplate. Table 4 shows the maximum von Mises stress values on the eight screws under the four different occlusion conditions.

Figure 6 shows the stress distributions on the mandible at the screw insertion positions (b1–b8 indicate the positions of the different screws and the corresponding sites in the mandible). High stress on the mandible was produced primarily on the buccal side. The ICP and RMOL conditions appeared to place higher stress on the mandible than did the other conditions. Table 5 shows the maximum von Mises stress values on the mandible at the eight screw insertion sites in the four different occlusion conditions.

4. Discussion

To treat mandibular deficiencies, the BSSO surgical procedure is often performed. However, this surgical treatment requires destruction of the mandible border, because the mandible border is the strongest part of the mandible and can resist bending forces. Therefore, it is essential that the fixation strength of the miniplate in the mandible is sufficient. Because of the limitations of previous in vitro experiments, including the use of only single forces, conducting relevant research on the effects of different occlusion conditions has been difficult, and thus, no relevant references exist. To help resolve this, the present study used finite element analysis to investigate the strength of the combination of the mandible and miniplate under four common occlusion conditions. The data in the study will provide clinicians with a reference basis for the stress incurred on the screws, miniplate, and mandible under different occlusion conditions following miniplate implantation.

Herein, regarding the overall stress distributions of the mandible, this study noted that following miniplate fixation, the mandible experienced external forces when clenched, which placed high stress on the miniplate. This high stress can primarily be explained by Hooke's law. If the mandible and miniplate were displaced, the stress would be proportional to Young's modulus. In the present study, Young's modulus of the miniplate and cortical bone was 110,000 and 17,000 MPa, respectively, indicating that in the overall structure, the miniplate experienced higher stress. The results of this study show that the values for the miniplate in the four groups are smaller than the yield strength of the titanium alloy (tensile strength of 1100 MPa [20]), and hence, the miniplate is not easily deformed under normal occlusion loading conditions. Further, of the four different occlusion conditions, the INC and RGF conditions placed less stress on the mandible than did the other conditions. The INC condition mainly simulated contact of the incisal edges, and because the muscles that produce this action apply little force, the mandible only experienced some high stress at the incisors. As the RGF condition simulated lateral movement of the right posterior dentition, the vertical force applied by the muscle to the mandible was also small (the force observed on the tooth is about 100 N according to previous literature [16]) and only the right posterior tooth area experienced relatively high stress. In addition, much higher stress is produced on mandible when ICP and RMOL condition. The ICP condition simulated maximum intercuspation of the posterior teeth. According to the previous literature, because of the small lever-arm relationship in the posterior tooth area (with the temporomandibular joint as the fulcrum), a high occlusion force occurs in the posterior tooth area (~700 N) [16], and thus, this study used a large external force for the muscle boundary condition setting. Consequently, obvious high stress was observed in the posterior tooth area of the mandible, along with high stress distributions in the mandible; these results are similar to those reported in previous studies [16]. The RMOL condition simulated contact of the right (unilateral) posterior teeth. This action is an unbalanced occlusion condition. As such, in addition to the occlusal forces concentrated in the posterior tooth area, the external force applied by the muscles is also large. Therefore, high stress occurred at the posterior tooth contact area and throughout the entire mandible. Additionally, since the occlusion is unbalanced, high non-occlusal stress occurred in the left side of the retromolar area, which may have been caused by the high stress that is produced

TABLE 1: The loading conditions, size, and direction of the muscular forces produced by the different occlusion conditions and sites of tooth fixation in the present study. This table is reproduced from Huang et al. [15] and Korioth and Hannam [16].

| Clenching tasks | Side | Direction | Muscular force (N) | | | | | | Constraint |
			SM	DM	MP	AT	MT	PT	
Incisal clench (INC)	Right	Force	76.2	21.2	136.3	12.6	5.7	3.0	Constrained the incisor regions
		Fx	-15.8	-11.6	66.3	-1.9	-1.3	-0.6	
		Fy	-31.9	7.6	-50.9	-0.6	2.9	2.6	
		Fz	67.3	16.1	107.8	12.5	4.8	1.4	
	Left	Force	76.2	21.2	136.3	12.6	5.7	3.0	
		Fx	15.8	11.6	-66.3	1.9	1.3	0.6	
		Fy	-31.9	7.6	-50.9	-0.6	2.9	2.6	
		Fz	67.3	16.1	107.8	12.5	4.8	1.4	
Intercuspal position (ICP)	Right	Force	190.4	81.6	132.8	154.8	91.8	71.1	Constrained the canine and premolar regions
		Fx	-39.4	-44.6	64.6	-23.1	-20.4	-14.8	
		Fy	-79.8	29.2	-49.6	-6.8	45.9	60.8	
		Fz	168.3	61.9	105.1	153.0	76.8	33.7	
	Left	Force	190.4	81.6	132.8	154.8	91.8	71.1	
		Fx	39.4	44.6	-64.6	23.1	20.4	14.8	
		Fy	-79.8	29.2	-49.6	-6.8	45.9	60.8	
		Fz	168.3	61.9	105.1	153.0	76.8	33.7	
Right unilateral molar clench (RMOL)	Right	Force	137.1	58.8	146.8	115.3	63.1	44.6	Constrained the right molars
		Fx	-28.4	-32.1	71.4	-17.2	-14.0	-9.3	
		Fy	-57.4	21.0	-54.8	-5.1	31.5	38.1	
		Fz	121.2	44.5	116.1	114.0	52.8	21.1	
	Left	Force	114.2	49.0	104.9	91.6	64.1	29.5	
		Fx	23.6	26.7	-51.0	13.7	14.2	6.1	
		Fy	-47.9	17.5	-39.1	-4.0	32.0	25.2	
		Fz	101.0	37.1	83.0	90.5	53.6	14.0	
Right group function (RGF)	Right	Force	34.3	29.4	12.2	104.3	61.2	46.9	Constrained the right canine, premolars, and molars
		Fx	-7.1	-16.0	6.0	-15.5	-13.6	9.8	
		Fy	-14.4	10.5	-4.6	-4.6	30.6	40.1	
		Fz	30.3	22.3	9.7	103.0	51.2	22.2	
	Left	Force	51.4	21.2	132.8	11.1	5.7	4.5	
		Fx	10.6	11.6	-64.6	1.7	1.3	0.9	
		Fy	-21.5	7.6	-49.6	-0.5	2.9	3.9	
		Fz	45.4	16.1	105.1	10.9	4.8	2.2	

SM: superficial masseter; DM: deep masseter; MP: medial pterygoid; AT: anterior temporalis; MT: middle temporalis; PT: posterior temporalis. All raw data were obtained from Huang et al. [15] and Korioth and Hannam [16].

TABLE 2: Material properties used in the present study.

	Young's modulus (MPa)	Poisson's ratio
Cancellous bone	1000	0.3
Cortical bone	17000	0.3
Miniplate	110000	0.3
Screw	118000	0.3

by bending or torsion. After BSSO surgery, the teeth are usually fixed in the ideal occlusion position (intermaxillary fixation); however, to improve patient life quality of post operation and maintain an open airway, many clinicians have opted not to perform intermaxillary fixation in recent years [5]. According to these study findings, after BSSO, patients should be advised to consume liquids and soft foods and to avoid ICP and RMOL occlusion to reduce the force on the mandible.

In the current study, the stress distributions on the miniplate showed that high stress mainly occurred in the middle part of the miniplate (the point of contact with the mandible). As previously indicated by Chuong et al. [21], the primary reason for this is that the miniplate area produces two bending forces and two torsion forces (Figure 7). Since both sides of the miniplate are fixed using screws, the miniplate is affected by torsion in the middle area, thereby producing higher stress. The miniplate is also subjected to an external force. Because of the geometric shape of the miniplate, high
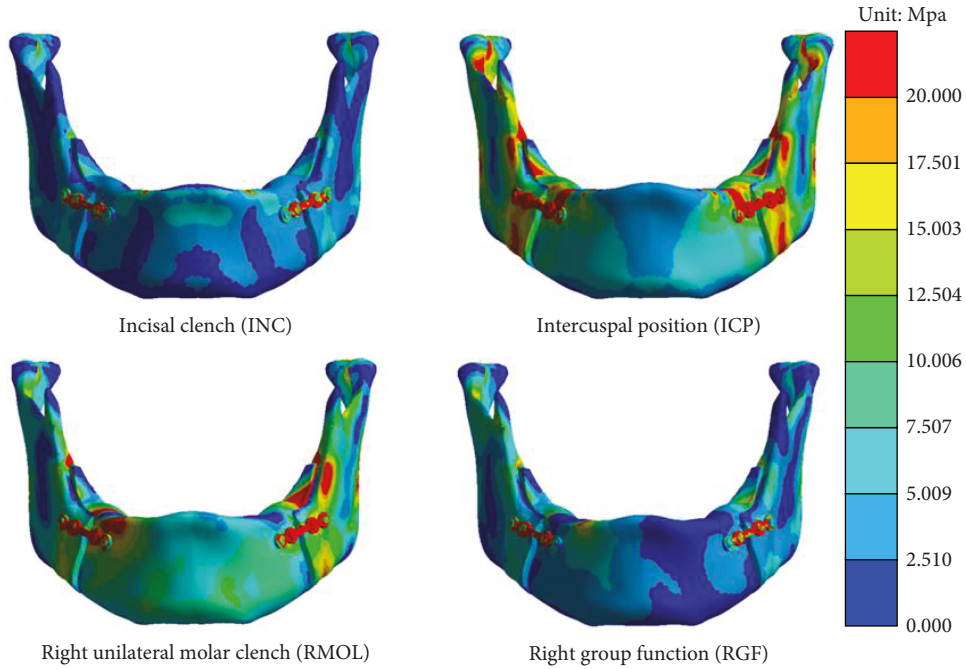
FIGURE 3: Overall stress distributions in the mandibular region under the four different occlusion conditions.
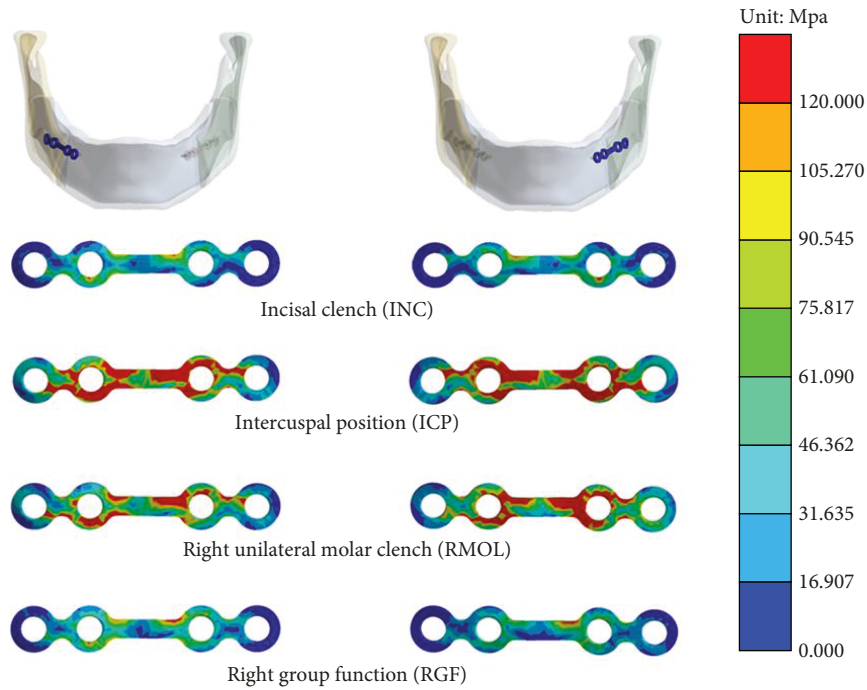
FIGURE 4: Stress distributions on the right and left miniplates under the four different occlusion conditions.

stress is generated where the cross-sectional area changes. However, the high stress that this study observed on the miniplate in the present study was less than the yield strength of the titanium alloy, and hence, the miniplate was not deformed under the four different occlusion conditions that this study evaluated.

When observing the stress distributions on the screws, this study found that the two screws near the middle of the

TABLE 3: Maximum von Mises stress values on the miniplates.

	Peak von Mises stress values on the right-side miniplates (MPa)	Peak von Mises stress values on the left-side miniplates (MPa)
INC	134.02	153.56
ICP	443.75	491.00
RMOL	302.60	372.80
RGF	157.10	138.58
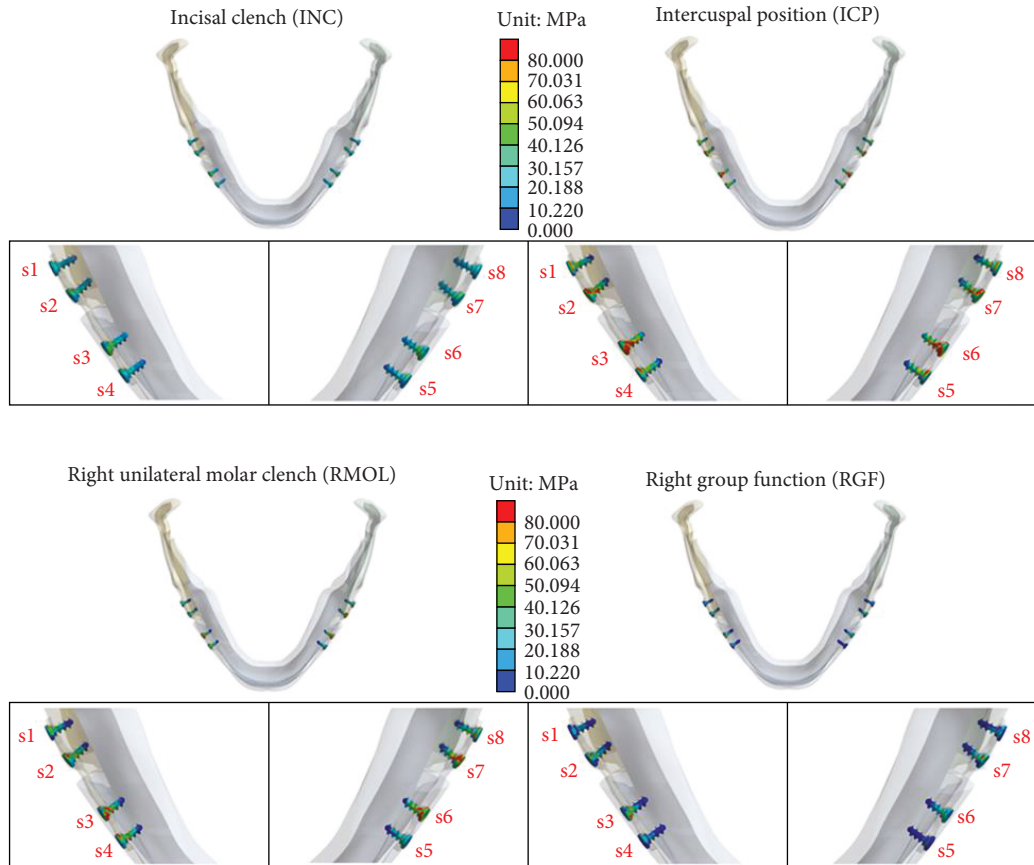
Figure 5: Stress distributions on the eight screws under the four different occlusion conditions.

Table 4: Maximum von Mises stress values on the eight screws.

	Peak von Mises stress on the s1 screw (MPa)	Peak von Mises stress on the s2 screw (MPa)	Peak von Mises stress on the s3 screw (MPa)	Peak von Mises stress on the s4 screw (MPa)	Peak von Mises stress on the s5 screw (MPa)	Peak von Mises stress on the s6 screw (MPa)	Peak von Mises stress on the s7 screw (MPa)	Peak von Mises stress on the s8 screw (MPa)
INC	118.950	169.530	120.050	64.761	66.414	116.790	165.190	117.220
ICP	365.220	588.470	406.780	187.420	207.540	392.390	577.830	356.560
RMOL	280.500	356.330	275.180	168.350	177.800	428.110	544.040	230.680
RGF	97.732	222.130	167.530	53.090	67.689	153.370	199.390	67.678

miniplate experienced higher stress than did the other screws, likely because the miniplate was being pulled to the screw that provided fixation of the mandible under the external bending and torsion forces. Thus, the two screws close to the middle of the miniplate experienced higher stress, especially the screw which is near the bone gap to the proximal segment (number 2 or 7). These findings suggest that clinicians should pay careful attention to the high stress that may be placed on the screw during miniplate fixation. Further, to achieve overall postimplant stability, a thicker screw should be used or the strength of the miniplate at that site should be enhanced.

When observing the stress distributions in the mandible at the screw insertion sites, this study noticed that the high stress sites were similar to those on the screws, primarily near the buccal side. The principles underlying this high stress are related to Hooke's law. During occlusion, when pulling by the miniplate produces displacement, the screw also pulls on the mandible and the surface of the mandibular screw hole (buccal side) will be deformed. Therefore, according to Hooke's law (the mandible has the same Young's modulus), high stress is produced near the buccal side. The deformation of the screw hole loosens the screw and miniplate, resulting in excessive movement between the bones, causing bone nonunion and potentially surgical failure, which may even require removal of the miniplate and refixation. These study findings indicate that it may be advisable to use thicker screws for fixation to reduce the stress on the screw and the likelihood of mandible deformation (the hole for screw insertion), as this will help
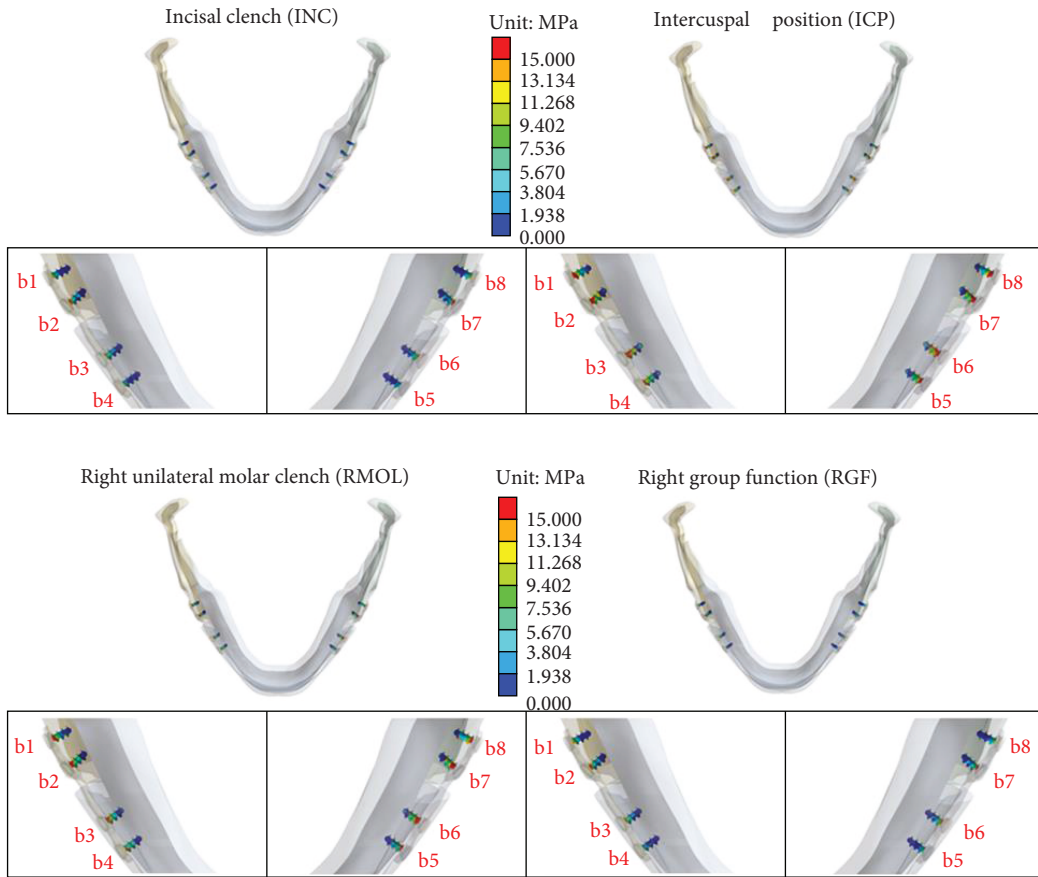
FIGURE 6: Stress distributions at the screw insertion sites in the mandible under the four different occlusion conditions.

TABLE 5: Maximum von Mises stress values at the screw insertion sites.

	Peak von Mises stress at b1 on the mandible (MPa)	Peak von Mises stress at b2 on the mandible (MPa)	Peak von Mises stress at b3 on the mandible (MPa)	Peak von Mises stress at b4 on the mandible (MPa)	Peak von Mises stress at b5 on the mandible (MPa)	Peak von Mises stress at b6 on the mandible (MPa)	Peak von Mises stress at b7 on the mandible (MPa)	Peak von Mises stress at b8 on the mandible (MPa)
INC	20.324	39.124	29.273	15.191	26.173	25.474	39.034	20.462
ICP	66.423	126.500	102.480	43.784	52.865	86.761	125.960	66.597
RMOL	48.194	82.709	61.630	48.399	115.490	98.718	109.400	65.414
RGF	22.321	41.563	39.653	14.452	30.620	26.072	38.142	16.680

to reduce surgical failure and increase the overall stability of the mandible.

This study using finite element analysis to investigate the forces involved when implanting a miniplate to treat mandibular deficiency has some limitations related to the biomechanical analysis of the different occlusion conditions. First, all of the material properties in this study were assumed to be homogeneous, isotropic, and linearly elastic in order to simplify the simulation, and thus, the material properties were set by referring to previous studies [15, 19]. Second, some of the models were simplified in the present study, that is, this study only observed the effects in the mandible, not in the entire skull, and no teeth were constructed. This study opted to use this simplified model because the main area of interest in the current study was the miniplate implantation site and such simplification can reduce the computer simulation time. To perform the stress and strain analysis of the tooth root or periodontal ligament and alveolar bone, we must establish a complete tooth model. However, this study mainly is aimed at investigating the efficacy of miniplate fixation on the mandible after BSSO surgery in 4 common occlusal conditions. This study was not aimed at investigating the biomechanical behavior of the teeth or periodontal areas. Therefore, this study did not consider the establishment of a tooth model. This study only fixed the mandible in the occlusal planes of different tooth positions. The literature has several reports on this method [15, 22]. The model used in this study was mainly designed with reference to
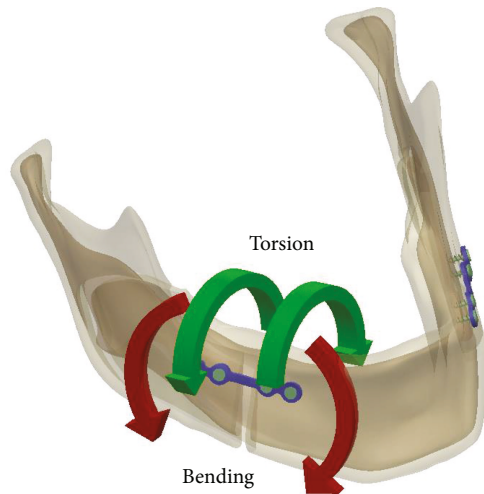
FIGURE 7: The miniplate region produces two bending forces and two torsion forces.

previous studies and simulated 4 occlusal modes, namely, INC, ICP, RMOL, and RGF. In this method, we fixed the tooth positions, utilized the external force on the mandible (giving boundary conditions by simulating muscle contractions) and applied restraint (using tooth position fixation as load conditions). However, due to these simplifications, this study finding may not directly replicate reality; nevertheless, clear trends can be identified for the topics of interest in the study.

Here, this study used finite element analysis and visual observations to investigate the biomechanical forces exerted on the miniplate, screws, and mandible under different occlusion conditions. The results showed that among the four evaluated occlusion conditions, the ICP and RMOL conditions in particular stressed and deformed the mandible and miniplate. Although the values identified in the present study are likely different from those in actual clinical situations, these study findings will provide a reference basis both for the maxillofacial surgeons when performing the BSSO surgery to treat mandibular deficiencies and for the patients during the recovery period. Patients should be advised to avoid specific occlusion movements to reduce the incidence of failure after surgical implantation and to improve their prognosis. This study data will also provide a biomechanical basis for the design and development of miniplates in the future.

5. Conclusion

The effects of different occlusal conditions on the miniplate, screws, and mandible after BSSO surgery for treating mandibular deficiency were investigated through finite element analysis. The results showed that the implanted miniplate exhibited high stress under various occlusion conditions. In the ICP and RMOL occlusion conditions, the overall mandibular structure experienced very high stress. According to this study model, the screw near the bone gap in the proximal segment experienced high stress. High stress was also generated at the site near the buccal side. The results of the present

study, in addition to providing a biomechanical basis for the forces generated on the miniplate, screws, and mandible following BSSO surgery, will also improve the design of miniplates and screws in the future to reduce the stress that is exerted on the screws and mandible. Moreover, patients are advised to avoid ICP and RMOL occlusion in order to reduce the incidence of miniplate implantation failure and to improve patients' prognoses.

Data Availability

The data used to support the findings of this study are available from the corresponding author upon request.

Conflicts of Interest

The authors declare that there is no conflict of interest regarding the publication of this paper.

Authors' Contributions

The authors Yuan-Han Chang and Man-Yee Chan contributed equally to this work.

Acknowledgments

References

[1] S. T. Daokar, G. Agrawal, C. Chaudhari, and S. Yamyar, "Ortho-surgical management of severe skeletal class II Div 2 malocclusion in adult," *Orthodontic Journal of Nepal*, vol. 7, no. 1, pp. 44–50, 2018.

[2] I. Yoshioka, A. Khanal, K. Tominaga, A. Horie, N. Furuta, and J. Fukuda, "Vertical ramus versus sagittal split osteotomies: comparison of stability after mandibular setback," *Journal of Oral and Maxillofacial Surgery*, vol. 66, no. 6, pp. 1138–1144, 2008.

[3] L. H. Guernsey and R. W. DeChamplain, "Sequelae and complications of the intraoral sagittal osteotomy in the mandibular rami," *Oral Surgery, Oral Medicine, Oral Pathology*, vol. 32, no. 2, pp. 176–192, 1971.

[4] J. Hartlev, E. Godtfredsen, N. T. Andersen, and T. Jensen, "Comparative study of skeletal stability between postoperative skeletal intermaxillary fixation and no skeletal fixation after bilateral sagittal split ramus osteotomy: an 18 months retrospective study," *Journal of Oral and Maxillofacial Research*, vol. 5, no. 1, 2014.

[5] L. Krekmanov, J. Lilja, and M. Ringqvist, "Sagittal split osteotomy of the mandible without postoperative intermaxillary fixation: a clinical and cephalometric study," *Scandinavian Journal of Plastic and Reconstructive Surgery*, vol. 23, no. 2, pp. 115–124, 2009.

[6] G. Hadi, B. G. Karine, C. Yves, and L. Pierre, "Stability of osteosynthesis with bicortical screws placed in a triangular

shape in mandibular sagittal split 5 mm advancement osteotomy: biomechanical tests," *British Journal of Oral and Maxillofacial Surgery*, vol. 48, no. 8, pp. 624–628, 2010.

[7] J. Nieblerová, R. Foltán, T. Hanzelka et al., "Stability of the miniplate osteosynthesis used for sagittal split osteotomy for closing an anterior open bite: an experimental study in minipigs," *International Journal of Oral and Maxillofacial Surgery*, vol. 41, no. 4, pp. 482–488, 2012.

[8] L. B. d. Olivera, E. Sant´Ana, A. J. Manzato, F. L. B. Guerra, and G. W. Arnett, "Biomechanical in vitro evaluation of three stable internal fixation techniques used in sagittal osteotomy of the mandibular ramus: a study in sheep mandibles," *Journal of Applied Oral Science*, vol. 20, no. 4, pp. 419–426, 2012.

[9] Y. Oguz, E. R. Watanabe, J. M. Reis, R. Spin-Neto, M. A. Gabrielli, and V. A. Pereira-Filho, "In vitro biomechanical comparison of six different fixation methods following 5-mm sagittal split advancement osteotomies," *International Journal of Oral and Maxillofacial Surgery*, vol. 44, no. 8, pp. 984–988, 2015.

[10] P. D. Ribeiro-Junior, O. Magro-Filho, K. A. Shastri, and M. B. Papageorge, "In vitro biomechanical evaluation of the use of conventional and locking miniplate/screw systems for sagittal split ramus osteotomy," *Journal of Oral and Maxillofacial Surgery*, vol. 68, no. 4, pp. 724–730, 2010.

[11] T. Nagasao, J. Miyamoto, T. Tamaki, and H. Kawana, "A comparison of stresses in implantation for grafted and plate-and-screw mandible reconstruction," *Oral Surgery, Oral Medicine, Oral Pathology, Oral Radiology*, vol. 109, no. 3, pp. 346–356, 2010.

[12] F. Sarkarat, M. H. K. Motamedi, B. Bohluli, N. Moharamnejad, S. Ansari, and H. Shahabi-Sirjani, "Analysis of stress distribution on fixation of bilateral sagittal split ramus osteotomy with resorbable plates and screws using the finite-element method," *Journal of Oral and Maxillofacial Surgery*, vol. 70, no. 6, pp. 1434–1438, 2012.

[13] E. Erkmen, B. Simsek, E. Yücel, and A. Kurt, "Comparison of different fixation methods following sagittal split ramus osteotomies using three-dimensional finite elements analysis. Part 1: advancement surgery-posterior loading," *International Journal of Oral and Maxillofacial Surgery*, vol. 34, no. 5, pp. 551–558, 2005.

[14] F. R. L. Sato, L. Asprino, P. Y. Noritomi, J. V. L. da Silva, and M. de Moraes, "Comparison of five different fixation techniques of sagittal split ramus osteotomy using three-dimensional finite elements analysis," *International Journal of Oral and Maxillofacial Surgery*, vol. 41, no. 8, pp. 934–941, 2012.

[15] H. L. Huang, K. C. Su, L. J. Fuh et al., "Biomechanical analysis of a temporomandibular joint condylar prosthesis during various clenching tasks," *Journal of Cranio-Maxillofacial Surgery*, vol. 43, no. 7, pp. 1194–1201, 2015.

[16] T. W. Korioth and A. G. Hannam, "Mandibular forces during simulated tooth clenching," *Journal of Orofacial Pain*, vol. 8, no. 2, pp. 178–189, 1994.

[17] C. H. Lee, C. M. Shih, K. C. Huang, K. H. Chen, L. K. Hung, and K. C. Su, "Biomechanical analysis of implanted clavicle hook plates with different implant depths and materials in the acromioclavicular joint: a finite element analysis study," *Artificial Organs*, vol. 40, no. 11, pp. 1062–1070, 2016.

[18] K. M. Su, M. H. Yu, H. Y. Su, Y. C. Wang, and K. C. Su, "Investigating biomechanics of different materials and angles of blades of forceps for operative delivery by finite element

analysis," *Journal of Mechanics in Medicine and Biology*, vol. 16, no. 4, article 1650046, 2016.

[19] K. C. Su, C. H. Chang, S. F. Chuang, and E. Y. K. Ng, "Biomechanical evaluation of endodontic post-restored teeth—finite element analysis," *Journal of Mechanics in Medicine and Biology*, vol. 13, no. 1, article 1350012, 2013.

[20] J. Enderle and J. Bronzino, *Introduction to Biomedical Engineering*, Academic Press, Boston, MA, USA, 3rd Edition edition, 2012.

[21] C. J. Chuong, B. Borotikar, C. Schwartz-Dabney, and D. P. Sinn, "Mechanical characteristics of the mandible after bilateral sagittal split ramus osteotomy: comparing 2 different fixation techniques," *Journal of Oral and Maxillofacial Surgery*, vol. 63, no. 1, pp. 68–76, 2005.

[22] S. M. Park, J. W. Lee, and G. Noh, "Which plate results in better stability after segmental mandibular resection and fibula free flap reconstruction? Biomechanical analysis," *Oral Surgery, Oral Medicine, Oral Pathology and Oral Radiology*, vol. 126, no. 5, pp. 380–389, 2018.

Research Article

The Evaluation of Different Radiological Measurement Parameters of the Degree of Collapse of the Vertebral Body in Vertebral Compression Fractures

Wei-En Hsu [iD],[1] Kuo-Chih Su [iD],[2,3] Kun-Hui Chen [iD],[1] Chien-Chou Pan [iD],[1,4] Wen-Hsien Lu [iD],[1,5] and Cheng-Hung Lee [iD][1,6]

[1]*Department of Orthopedics, Taichung Veterans General Hospital, Taichung, Taiwan*
[2]*Department of Medical Research, Taichung Veterans General Hospital, Taichung, Taiwan*
[3]*Department of Biomedical Engineering, Hung Kuang University, Taichung, Taiwan*
[4]*Department of Rehabilitation Science, Jenteh Junior College of Medicine, Nursing, and Management, Miaoli County, Taiwan*
[5]*Department of Orthopedics, Feng Yuan Hospital, Taichung, Taiwan*
[6]*Department of Food Science and Technology, Hung Kuang University, Taichung, Taiwan*

Correspondence should be addressed to Cheng-Hung Lee; leechenghung0115@gmail.com

Received 14 February 2019; Revised 3 April 2019; Accepted 21 April 2019; Published 8 May 2019

Guest Editor: Yuan-Chiao Lu

For compression fracture, vertebral body height loss (VBHL) and kyphotic angle (KA) are two important imaging parameters for determining the prognosis and appropriate treatment. This study used previous measurement methods to assess the degree of VBHL and KA, compare and examine differences between various measurement methods, and examine the correlation between relevant measurement parameters and intravertebral cleft (IVC) in the vertebral body. The radiographic images (lateral view of the T-L spine) of 18 patients with a single-level vertebral compression fracture were reviewed. We measured 9 characteristic lengths and angles on plain radiographs, including anterior vertebral height (AVH) and AVH of the adjacent upper and lower levels, middle vertebral height (MVH) and MVH of the adjacent upper and lower levels, posterior vertebral height (PVH), and vertebral body width, and assessed 6 parameters, including vertebral compression ratio (VBCR), percentage of anterior height compression (PAHC), percentage of middle height compression (PMHC), kyphotic angle (KA), calculated kyphotic angle (CKA), and IVC. The results showed that VBCR is a simple and rapid method of VBHL assessment, but it may result in an underestimation of the degree of VBHL compared to PAHC. When PMHC < 40% or kyphotic angle > 15°, the probability of IVC occurring on the vertebral body was higher which means the higher risk of vertebral body instability. The results of this study could provide a reference for surgeons when using imaging modalities to assess the degree of vertebral body collapse.

1. Introduction

As the population ages, the prevalence of osteoporosis also gradually increases, and the resulting medical cost increases every year. Vertebral compression fracture is one of the important complications of osteoporosis [1, 2]. In clinical practice, acute lower back pain is a classical presentation of the disease. Among imaging modalities, radiography is the most widely used tool for the diagnosis and assessment of compression fractures. Vertebral body height loss (VBHL) and kyphotic angle (KA) are two important imaging

parameters for determining the prognosis and appropriate treatment [3]. The degrees of collapse of the vertebral body may affect the direction of treatment (nonsurgical management, like rest, bracing, and pain control drug, or surgery, like vertebra augmentation, instrumentation, or fusion). As VBHL increases, the vertebra may become more unstable. In addition to its effects on stability, KA can negatively affect sagittal alignment. Data have shown that a KA of >15°–30° or height loss of >50% resulted in vertebral body instability, which may require a more invasive treatment such as vertebral augmentation [4–6].

The definition and measurement methods for these two important imaging parameters are still controversial, and no conclusion has been reached thus far [7]. Previously, researchers used different measurement methods to assess the degree of vertebral body collapse by using posterior wall height as the reference vertebral body compression ratio (VBCR) or the percentage of anterior height compression (PAHC), which uses the mean height of segments adjacent to a healthy vertebral body as the reference value [8–11]. However, differences in the range of vertebral body collapse may result in measurement errors. In addition to the degree of vertebral body collapse, the intravertebral cleft (IVC) can represent osteonecrosis of the vertebral body, which has a higher probability of progressing to advanced kyphosis [12]. However, thus far, to the best of our knowledge, no study has examined the correlation between IVC and VBHL.

The aforementioned literature demonstrates that different data will be obtained if different measurement methods are used. In addition, differences in deformity may also result in measurement errors. However, no related study has examined and analyzed the differences and limitations of different measurement methods. Therefore, the aim of this study was to use previous measurement methods to assess the degree of vertebral body collapse, compare and examine differences between various measurement methods, and examine the correlation between relevant measurement parameters and IVC in the vertebral body.

2. Materials and Methods

2.1. Collection of Materials. This study quantitatively analyzed radiographic images (lateral view of the T-L spine) obtained before single-level vertebroplasty in patients who had osteoporotic vertebral compression fractures treated between June 2013 and January 2015 at the Department of Orthopedics, Taichung Veterans General Hospital, Taiwan. The radiographic images of 18 patients who underwent single-level vertebroplasty were examined. Seven patients were male, and 11 were female. These 18 sets of radiographic images were obtained from 101 images by excluding images with poor preoperative radiographic quality, having difficulty for taking measurements, showing a compression fracture in two or more vertebral levels, showing a nonosteoporotic vertebral compression fracture (bone tumor, metastasis, or infection), or showing a previous spine surgery or combination with other surgeries (instrumentation or fusion). Clinical parameters such as age, sex, height, body weight, and vertebral level of the 18 patients were recorded.

2.2. Measurement of Imaging Parameters. This study mainly measured 9 characteristic lengths and angles on plain radiographs. The image was digitalized and could be reviewed via professional software, SmartIris (SmartIris 1.3.0.14, Taiwan Electronic Data Processing Corp.), which contains a lot of tools, including measurement of distance and angle and zoom-in or zoom-out. With this assistance of this professional software, the image can be enlarged to show the detail which we want to measure. The distance and angle could be
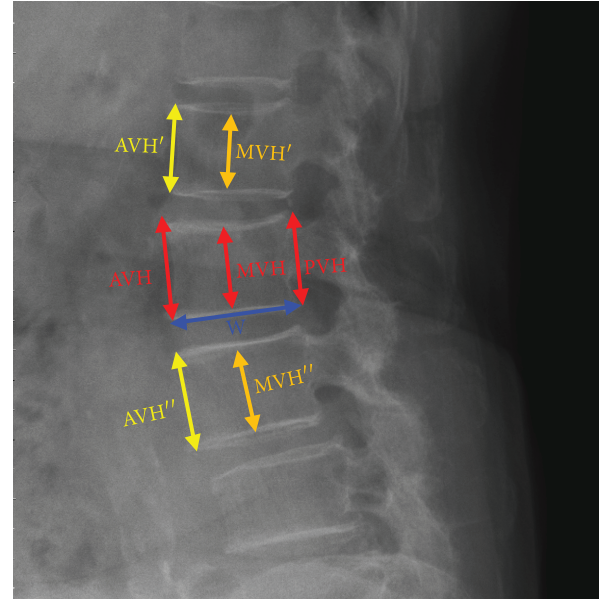
(a)

Vertebral compression ratio

$$VBCR = \frac{AVH}{PVH} \times 100\%$$

Percentage of anterior height compression

$$PAHC = \frac{AVH}{[(AVH'+AVH'')/2]} \times 100\%$$

Percentage of middle height compression

$$PMHC = \frac{MVH}{[(MVH'+MVH'')/2]} \times 100\%$$

Calculation of kyphotic angle

$$CKA = \tan^{-1}[\frac{(PVH-AVH)}{W}]$$

(b)

FIGURE 1: (a) This study mainly measures the characteristic lengths on plain radiographs (AVH: anterior vertebral height; MVH: middle vertebral height; PVH: posterior vertebral height; W: vertebral body width). (b) Parameters examined in this study (VBCR, PAHC, PMHC, and CKA).

measured accurately. These parameters included anterior vertebral height (AVH) and AVH of the adjacent upper and lower levels (AVH$'$ and AVH$''$, respectively), middle vertebral height (MVH) and MVH of the adjacent upper and lower levels (MVH$'$ and MVH$''$, respectively), posterior vertebral height (PVH), vertebral body width (W; Figure 1), and KA (Figure 2). The lengths and angles measured using these 9 measurements were used to assess the degree of vertebral body collapse. Six observation markers were used: (1) VBCR = AVH/PVH × 100%; VBCR is mainly used to calculate the AVH-to-PVH ratio; (2) PAHC = AVH/[(AVH$'$ + AVH$''$)/2] × 100%; PAHC mainly calculates the ratio of AVH to the mean of AVH of the adjacent upper and lower levels; (3) percentage of middle height compression (PMHC) = MVH/[(MVH$'$ + MVH$''$)/2]; PMHC mainly calculates the ratio of MVH to the mean MVH of the
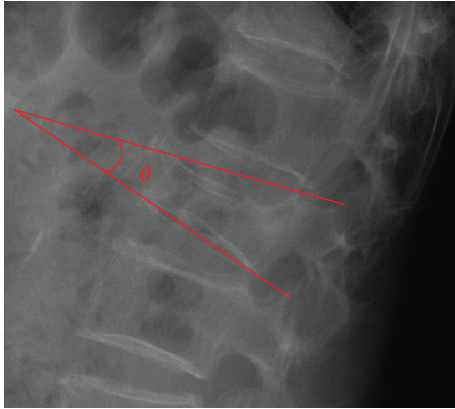
FIGURE 2: Kyphotic angle measurements.
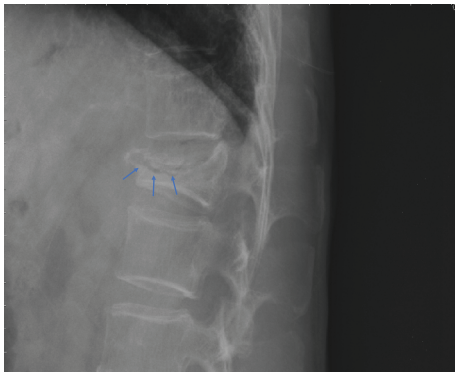
FIGURE 3: Lateral plain radiograph of the thoracolumbar spine. The arrows point to the crescent-shaped shadow in the vertebral body, that is, the IVC.

adjacent upper and lower segments; (4) KA; (5) calculated KA $(CKA) = \tan^{-1}[(PVH - AVH)/W]$; and (6) IVC (Figure 3).

This study measured the length and angle data of the vertebral body after collapse in the 18 sets of radiographs and obtained 6 markers for examining vertebral body collapse. The analyzed markers can be used to compare the differences between the PAHC and VBCR measurements. In addition, PMHC, KA, and CKA were used to assess associations with IVC occurrence.

3. Results

In this study, we used 18 sets of images for radiographic (lateral view of the T-L spine) measurements. Table 1 mainly shows the relevant data of the patients (age, sex, height, body weight, and number of images of the vertebral bodies at different levels).

Figure 4 mainly shows the mean VBCR (range, 22.94%–84.75%; mean, 54.21%±17.13%) and PAHC (range, 20.00%–77.82%; mean, 54.21%±17.13%) of the 18 sets of radiographs. The marker results show that the VBCRs are greater than the PAHC, with differences ranging from −2.5% to 27.74%.

Table 2 shows the calculated PMHC, KA, and CKA of the 18 sets of radiographs. The PMHC ranged from 14.23% to

TABLE 1: Patient characteristics.

Age (years)	78.94 ± 7.92	
Sex	Male: 7, female: 11	
Height (cm)	156.7 ± 6.57	
Body weight (kg)	58.8 ± 12.90	
	T9	1
The number of images	T12	6
of the vertebral bodies	L1	8
at different levels	L3	2
	L5	1

FIGURE 4: The values of VBCRs and PAHC measured from 18 sets of radiographs.

TABLE 2: The PAHC, KA, CKA, and IVC data obtained in this study.

Imaging sample No.	PMHC (%)	KA (°)	CKA (°)	Whether IVC occurs
1	22.55	10	13.90	No
2	26.23	16	17.23	No
3	64.98	18	19.46	No
4	37.65	18	16.97	Yes
5	14.23	19	18.19	Yes
6	74.37	6	9.92	No
7	63.92	14	10.07	No
8	85.51	10	12.36	No
9	43.09	17	19.62	No
10	38.93	15	15.76	Yes
11	40.68	15	17.52	Yes
12	65.38	12	12.69	No
13	20.38	24	26.91	Yes
14	63.18	12	14.43	No
15	25.94	19	22.83	Yes
16	29.09	13	12.56	No
17	44.00	5	4.82	No
18	70.08	12	14.00	No

74.37% (mean, 46.12%±21.35%). The KAs ranged from 4.81° to 26.91° (mean, 14.95 ± 5.45). CKAs ranged from 5.00° to 23.80° (mean, 13.86 ± 6.93). In addition, in Table 2, whether IVC occurred in each group is indicated.

4. Discussion

In this study, we mainly used the geometric data of radiographic measurements to examine different assessment markers and assess vertebral body collapse. Of the markers used, VBCR, PAHC, and KA were based on assessment methods in previous studies, while PMHC and CKA are new parameters examined in this study.

Previous studies pointed out that most physicians usually use VBCR to assess VBHL [8]. However, the Spine Trauma Study Group recommends the use of PAHC measurement in the assessment of VBHL [9]. In this study, we observed and compared the results of VBCR and PAHC and found that VBCRs are generally higher than PAHC (−2.5% to 27.74%). The main reason for this is that compression fractures may involve the entire vertebral body, resulting in a decrease in the height of the entire vertebral body. Therefore, the use of PVH to assess vertebral body height may result in an underestimation of the degree of collapse. By contrast, PAHC mainly measures the mean of the heights of adjacent segments and will therefore not be affected by vertebral body collapse and not result in measurement errors.

In addition, our study calculated PMHC to represent the degree of vertebral body collapse. In most studies that assessed VBHL, AVH was mostly used to represent the degree of collapse in the entire vertebral body [8, 9]. However, clinical observations showed that vertebral body collapse at the middle region is often the region with the most severe collapse [13]. This may be because the bone at the middle region is softer. Therefore, we proposed PMHC as a marker of the degree of collapse at the middle region of the vertebral body. Our study also found that PMHC was associated with IVC. When PBMC was <40% (degree of collapse, >60%), the probability of IVC was higher (62.5%, 10% in the group with PMHC of >40%). Several studies suggested that IVC will increase the risk of vertebral body instability [14–16]. Therefore, we believed that in addition to PAHC, PMHC may be another important marker to assess vertebral compression fractures. However, more reliable studies are needed to elucidate the clinical role of PMHC.

In addition to being a measurement marker for assessing vertebral body collapse, KA also affects sagittal alignment [17, 18]. However, endplate deformation may sometimes occur during vertebral body collapse, and angles are not easy to measure, which can result in measurement errors. On the other hand, some researchers suggested that the endplates at the top and bottom of adjacent segments can be used to measure Cobb's angle [19]. However, this measurement method will be affected by disk deformity. In our study, we proposed the use of the anterior and posterior heights of the vertebral body and vertebral body width to estimate the kyphotic angle. This can be used as an alternative method when the angle cannot be measured. The CKA calculation results presented in this study show similar trends as the kyphotic angle measurement results in previous studies (difference, <2° in most case). However, larger errors will occur in CKA measurement during severe middle collapse of the vertebral body, as PVH and AVH are not parallel. Previous studies proposed that a reduction of 4 cm in vertebral body height will result in more than 15° of kyphotic deformity [20], while our study found that KA may be increased by 1° when there is a height difference of 7 mm between PVH and AVH. In addition, our study also found that the greater the kyphotic angle or CKA (when the angle is greater than about 15°), the greater the probability of IVC occurring at the vertebral body.

Our study used radiography for measurements, which may have some limitations. The height of adjacent segments must be used as a reference in PAHC measurements. Therefore, at present, it is only applicable to measurements for compression fractures at adjacent segments of healthy vertebral bodies. Higher-quality studies are required to determine whether this method can be extended to compression fractures in multiple segments. In addition, our study only focused on osteoporotic vertebral compression fractures and excluded compression fractures due to other factors or due to the presence of images with poor quality. Therefore, the number of reviewed images was low, and the most reviewed levels were mainly T12 and L1, which are also the most common sites for osteoporotic vertebral compression fractures. Therefore, the data obtained have reference values.

In this study, we used radiographic images to assess 6 parameters related to the vertebral body. VBCR only requires AVH and PVH measurements and is a simple and rapid method of VBHL assessment. However, when the collapse involves the posterior wall, the use of VBCR may result in an underestimation of the degree of VBHL. By contrast, although more parametric measurements are required for PAHC, it can assess VBHL with higher accuracy. More studies are expected to examine markers of severity of osteoporotic vertebral compression fractures, and a unified measurement standard is needed in the future so that clinicians can have reference data for assessment of the degree of collapse of the vertebral body and determining treatment directions.

5. Conclusion

We used radiographic images to measure the 9 characteristic lengths and angles of vertebral bodies to assess the degree of VBHL. These data were used to calculate the 6 assessment markers. The study results showed that values obtained with VBCR assessment were greater than those obtained with the PAHC. When the measured PMHC was <40%, the probability of observing IVC on the vertebral body was higher. When the measured KA or CKA was greater, the probability of IVC occurring on the vertebral body was higher. The results of this study can provide a reference for surgeons when using imaging modalities to assess the degree of vertebral body collapse.

Data Availability

The data used to support the findings of this study are available from the corresponding author upon request.

Conflicts of Interest

The authors declare that there is no conflict of interest regarding the publication of this paper.

Authors' Contributions

The authors Wei-En Hsu and Kuo-Chih Su contributed equally to this work.

Acknowledgments

References

[1] H. Frost, "Clinical management of the symptomatic osteoporotic patient," *The Orthopedic Clinics of North America*, vol. 12, no. 3, pp. 671–681, 1981.

[2] Y. Lee and K. M. Yip, "The osteoporotic spine," *Clinical Orthopaedics and Related Research*, vol. 323, pp. 91–97, 1996.

[3] K. E. Ensrud and J. T. Schousboe, "Vertebral fractures," *New England Journal of Medicine*, vol. 364, no. 17, pp. 1634–1642, 2011.

[4] M. Chadha and R. Bahadur, "Steffee variable screw placement system in the management of unstable thoracolumbar fractures: a third world experience," *Injury*, vol. 29, no. 10, pp. 737–742, 1998.

[5] P. C. McAfee, H. A. Yuan, B. E. Fredrickson, and J. P. Lubicky, "The value of computed tomography in thoracolumbar fractures. An analysis of one hundred consecutive cases and a new classification," *The Journal of Bone and Joint Surgery*, vol. 65, no. 4, pp. 461–473, 1983.

[6] M. R. Mikles, R. P. Stchur, and G. P. Graziano, "Posterior instrumentation for thoracolumbar fractures," *Journal of the American Academy of Orthopaedic Surgeons*, vol. 12, no. 6, pp. 424–435, 2004.

[7] A. R. Vaccaro, D. H. Kim, D. S. Brodke et al., "Diagnosis and management of thoracolumbar spine fractures," *Journal of Bone and Joint Surgery-American Volume*, vol. 85, no. 12, pp. 2456–2470, 2003.

[8] S. Sadiqi, J. J. Verlaan, A. M. Lehr et al., "Measurement of kyphosis and vertebral body height loss in traumatic spine fractures: an international study," *European Spine Journal*, vol. 26, no. 5, pp. 1483–1491, 2017.

[9] O. Keynan, C. G. Fisher, A. Vaccaro et al., "Radiographic measurement parameters in thoracolumbar fractures: a systematic review and consensus statement of the spine trauma study group," *Spine*, vol. 31, no. 5, pp. E156–E165, 2006.

[10] T. Isomi, M. M. Panjabi, Y. Kato, and J.-L. Wang, "Radiographic parameters for evaluating the neurological spaces in experimental thoracolumbar burst fractures," *Journal of Spinal Disorders*, vol. 13, no. 5, pp. 404–411, 2000.

[11] J. Mumford, J. N. Weinstein, K. F. Spratt, and V. K. Goel, "Thoracolumbar burst fractures. The clinical efficacy and outcome of nonoperative management," *Spine*, vol. 18, no. 8, pp. 955–970, 1993.

[12] K.-N. Chou, B.-J. Lin, Y.-C. Wu, M.-Y. Liu, and D.-Y. Hueng, "Progressive kyphosis after vertebroplasty in osteoporotic vertebral compression fracture," *Spine*, vol. 39, no. 1, pp. 68–73, 2014.

[13] S. E. Ahn, K. N. Ryu, J. S. Park, W. Jin, S. Y. Park, and S. B. Kim, "Early bone marrow edema pattern of the osteoporotic vertebral compression fracture: can be predictor of vertebral deformity types and prognosis?," *Journal of Korean Neurosurgical Society*, vol. 59, no. 2, pp. 137–142, 2016.

[14] M. C. Wiggins, M. Sehizadeh, T. K. Pilgram, and L. A. Gilula, "Importance of intravertebral fracture clefts in vertebroplasty outcome," *American Journal of Roentgenology*, vol. 188, no. 3, pp. 634–640, 2007.

[15] J.-S. Jang, D.-Y. Kim, and S.-H. Lee, "Efficacy of percutaneous vertebroplasty in the treatment of intravertebral pseudarthrosis associated with noninfected avascular necrosis of the vertebral body," *Spine*, vol. 28, no. 14, pp. 1588–1592, 2003.

[16] G. Wang, H. Yang, and K. Chen, "Osteoporotic vertebral compression fractures with an intravertebral cleft treated by percutaneous balloon kyphoplasty," *The Journal of Bone and Joint Surgery. British volume*, vol. 92-B, no. 11, pp. 1553–1557, 2010.

[17] B. B. Pradhan, H. W. Bae, M. A. Kropf, V. V. Patel, and R. B. Delamarter, "Kyphoplasty reduction of osteoporotic vertebral compression fractures: correction of local kyphosis versus overall sagittal alignment," *Spine*, vol. 31, no. 4, pp. 435–441, 2006.

[18] H. A. Yuan, C. W. Brown, and F. M. Phillips, "Osteoporotic spinal deformity," *Journal of Spinal Disorders & Techniques*, vol. 17, no. 3, pp. 236–242, 2004.

[19] T. R. Kuklo, D. W. Polly Jr, B. D. Owens, S. M. Zeidman, A. S. Chang, and W. R. Klemme, "Measurement of thoracic and lumbar fracture kyphosis: evaluation of intraobserver, interobserver, and technique variability," *Spine*, vol. 26, no. 1, pp. 61–66, 2001.

[20] A. Papaioannou, N. B. Watts, D. L. Kendler, C. K. Yuen, J. D. Adachi, and N. Ferko, "Diagnosis and management of vertebral fractures in elderly adults," *The American Journal of Medicine*, vol. 113, no. 3, pp. 220–228, 2002.

Research Article

A Prototype Intraoral Periapical Sensor with High Frame Rates for a 2.5D Periapical Radiography System

Che-Wei Liao [iD],[1,2] **Ker-Jer Huang,**[2] **Jyh-Cheng Chen** [iD],[3] **Chih-Wei Kuo,**[2] **Yin-Yi Wu** [iD],[2] **and Jui-Ting Hsu** [iD][4,5]

[1]*Graduate Institute of Biomedical Sciences, China Medical University, Taichung 404, Taiwan*
[2]*Materials & Electro-Optics Research Division, National Chung-Shan Institute of Science & Technology, Taoyuan City 407, Taiwan*
[3]*Department of Biomedical Imaging and Radiological Sciences, National Yang-Ming University, Taipei 112, Taiwan*
[4]*School of Dentistry, College of Dentistry, China Medical University, Taichung 404, Taiwan*
[5]*Department of Bioinformatics and Medical Engineering, Asia University, Taichung 413, Taiwan*

Correspondence should be addressed to Yin-Yi Wu; davidwu0801@gmail.com and Jui-Ting Hsu; jthsu@mail.cmu.edu.tw

X-ray radiography is currently used in dentistry and can be divided into two categories: two-dimensional (2D) radiographic images (e.g., using periapical film, cephalometric film, and panoramic X-ray) and three-dimensional (3D) radiographic images (e.g., using dental cone-beam computed tomography (CBCT)). Among them, 2D periapical film images are most commonly used. However, 2D periapical film compresses 3D image information into a 2D image, which means that depth cannot be identified from the image. Such compressed images lose a considerable amount of information, reducing their clinical applicability. A 2.5D periapical radiography system prototype was developed by our research team. Our previous study indicated that this prototype could be used to capture images at different depths of an object. However, the prototype was limited by its commercially available intraoral periapical sensor, which had a low temporal resolution and could not capture multiple images in a short period of time. Therefore, the total time required for image capture was too long for practical clinical application. The present study developed a high-frame-rate intraoral periapical sensor with a sensor imaging speed of up to 15 Hz. The primary components of the developed intraoral periapical sensor include a scintillator, complementary metal oxide semiconductor chip, component circuit board, and video processing board. The external dimensions of the sensor are $41 \times 26 \times 6.6$ mm^3. The performance of the developed high-frame-rate intraoral periapical sensor was verified through qualified and quantified analyses using line pairs. The results showed that the resolution of the developed intraoral periapical sensor could reach 18 lp/mm. The sensor was further installed in our 2.5D periapical radiography system to conduct image capturing. The results indicated that the developed sensor could be used for high-frame-rate imaging to incorporate tomosynthesis to obtain reconstructed slice images of different depths. The developed sensor has the potential for clinical dentistry applications in the future.

1. Introduction

Since X-ray was discovered by Wilhelm Conrad Röntgen more than 100 years ago, it has been widely applied in medicine. X-ray can be used for noninvasive medical examinations and is one of the methods often used to assess hard tissue before surgery [1]. X-ray imaging requires a sensor to capture the image. In the early days of X-ray technology, radiographic films were applied to capture images. In the past 30 years, sensors for X-ray imaging have gradually been digitalized [2], and digital radiography can now be divided into three categories, namely, computed radiography (CT), indirect digital radiography, and direct digital radiography [3, 4]. In dentistry, the most common application of X-rays is periapical film, which has advantages such as high resolution, easy operation, and low costs [5, 6]. However, periapical film can only provide two-dimensional (2D) images; specifically, three-dimensional (3D) tissue compressed projection can only be displayed in a 2D image. In such 2D images, 3D tissues with different depths are relatively difficult to

(a)   (b)
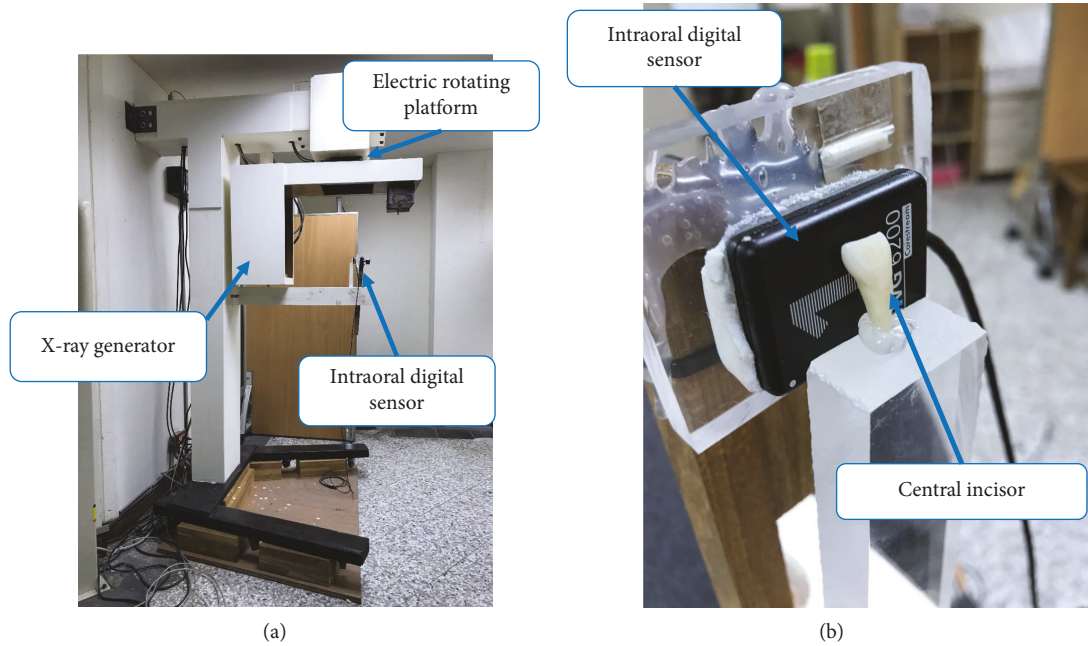
FIGURE 1: Prototype of the intraoral digital tomosynthesis system: (a) entire view and (b) close view (figure reproduced with permission).

distinguish, and image distortion may be caused in the compression process, thereby often limiting the clinical applicability [7, 8].

To overcome the shortcomings of image compression in periapical film, scholars have conducted experiments using tomosynthesis in imaging [9]. In 2013, Li et al. [7] conducted a laboratory experiment with a pig's mandible. A film was placed on the posterior mandible, and the X-ray tube was rotated at a limited angle of ±30°. These 2D projection images were reconstructed through tomosynthesis to obtain numerous slice images of different depths. Shan et al. [10] and Inscoe et al. [11, 12] used a carbon nanotube X-ray source array to develop stationary digital tomosynthesis for dental imaging. In their studies [10–12], the feasibility of stationary intraoral tomosynthesis was demonstrated. They built prototype stationary intraoral tomosynthesis imaging systems, which were evaluated and found to meet all the manufacturers' specifications. In addition, our team built a prototype of a 2.5D periapical radiography system in 2018 [13]. Adopting the tomosynthesis approach, we placed a canine in front of a commercially available intraoral periapical sensor and rotated the X-ray tube (±60°) to obtain various 2D projection images. The images were reconstructed using tomosynthesis. Our results proved that tomosynthesis can be applied in dentistry to obtain slice images of different depths [14–16]. However, in the experiment, we also found that the commercially available intraoral periapical sensor possessed relatively low temporal resolution and that the system could not continuously capture images multiple times in a short period. Because the original purpose of the commercially available intraoral periapical sensor was not continuous capture of high-frame-rate images, it took tens of minutes to capture a set of images, making it unsuitable for clinical application. Therefore, in order for our proposed 2.5D periapical radiography system to be used as a diagnostic tool in dentistry, it

requires a high temporal resolution sensor that can continuously capture multiple images in a short period.

Currently, high-frame-rate sensors are used in technology such as CT, CBCT, and micro-CT [5, 17, 18], all of which employ large sensors that cannot be placed in the mouth. Therefore, this study developed a high-frame-rate intraoral periapical sensor capable of frame rates of up to 15 Hz. The developed sensor was applied to the 2.5D periapical radiography system developed by this research team.

2. Materials and Methods

In our previous study [13], we developed a prototype 2.5D periapical radiography system (Figure 1) combining a commercially available intraoral periapical sensor, an X-ray tube, and a supporting frame. A total of 121 canine 2D projection images were taken at a limited angle of ±60°. The images were reconstructed using tomosynthesis to obtain slice images of the canine at different depths. However, the commercial intraoral periapical sensor used in the prototype requires cooling for a few seconds between takes to avoid overheating. The process of capturing a set of images in the range of ±60° therefore took tens of minutes to complete, making the system unsuitable for clinical applications. The present study therefore designed a high-frame-rate intraoral periapical sensor capable of frame rates of up to 15 Hz. The proposed sensor could greatly shorten the shooting interval, thereby enhancing its clinical applicability.

2.1. Components of the High-Frame-Rate Intraoral Periapical Sensor. The intraoral component of the proposed high-frame-rate intraoral periapical sensor can be divided into four parts, namely, the scintillator, complementary metal oxide semiconductor (CMOS) chip, component circuit board, and video processing board (Figure 2). The top layer

(a) (b)
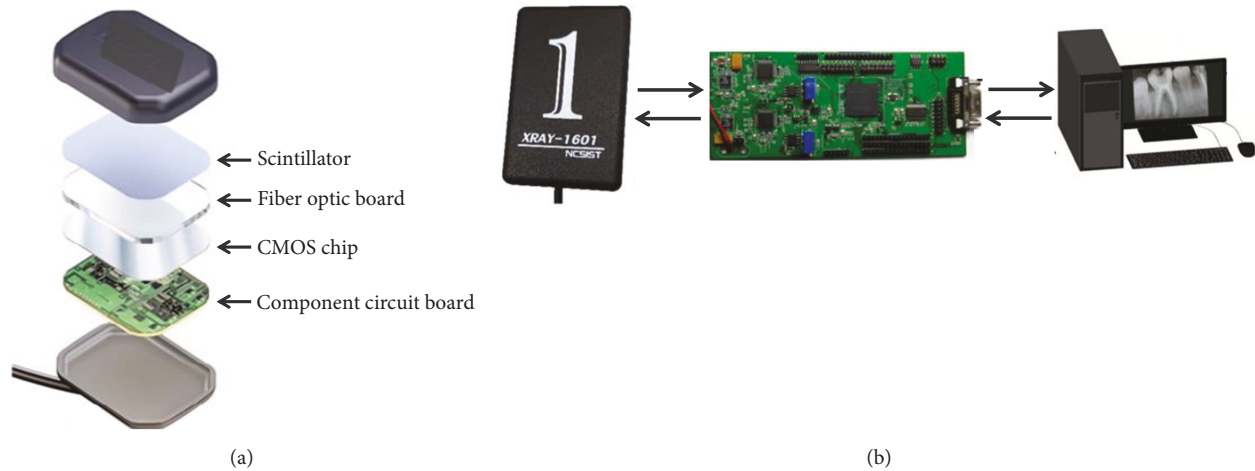
FIGURE 2: (a) The major components of the high-frame-rate intraoral periapical sensor and (b) the high-frame-rate intraoral periapical sensor, video processing board, and control computer.

(a) (b)
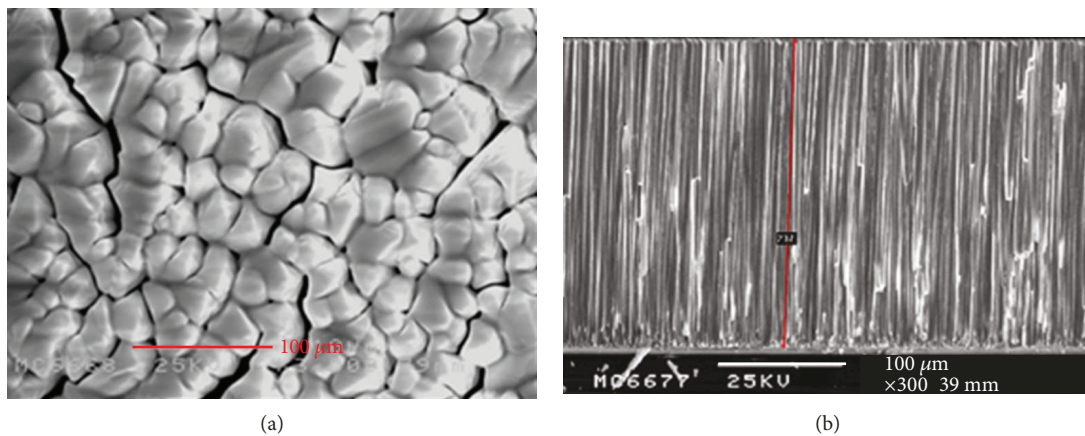
FIGURE 3: Scanning electron microscope images of the thin-film scintillator: (a) top view and (b) cross-sectional side view.

is the scintillator. The scintillator converts the X-ray intensity to visible light of different grayscales, and the visible light signals are then converted from photon signals to electric signals through the coupling layer and complementary metal oxide semiconductor (CMOS) sensor array. Subsequently, the electric signals from the CMOS sensor array are transmitted to a video processing board (outside the subject's mouth) through a USB 3.0 cable. The electric (analog) signals of the CMOS sensor array are then converted into digital signals, which are transmitted to the computer for imaging (Figure 2).

2.1.1. Process of Scintillator. CsI scintillator columns exhibit high absorption capacity for X-rays. These columns can be applied in scintillation detectors for capturing simultaneous short-wave images as well as for digitalizing images. A pure CsI scintillator has an extremely short luminescence decay time (3.5 ns); however, incorporation of a thallium activator can greatly improve the crystal luminescence efficiency, thereby facilitating coupling between the optical emission and photomultiplier. In addition to enhancing the photoelectron conversion efficiency of the scintillator, changing the refractive index of the X-ray in the anodic aluminum oxide

template can increase the residence time of the X-ray in the CsI(Tl) crystal and improve the photoelectron conversion efficiency of the scintillator.

In this study, we used the thermal evaporation method and adjusted the controlling process parameters to grow a columnar CsI film. After the CsI(Tl) powder was uniformly mixed, the powder was made into a compressed tablet by using a tablet press machine and sintered to remove moisture and impurities in the powder through annealing. The powder can be made more compact through the compressing process, thereby reducing the amount of air in the tablet. The purpose of the tablet compression was to prevent the air from being rapidly expanded due to the heat during the evaporation process, which may have caused powder splash that would affect the quality of the scintillator. Annealing using different temperature parameters can effectively eliminate thin-film cracking, formation of voids on the film, and a disordered structure of the interface (Figure 3).

2.1.2. CMOS Chip and Component Circuit Board. Once the scintillator produces visible light, the optical signals are transmitted to the CMOS image sensor by the continuous shooting fiber optic board. The CMOS is a mixed integrated

XRAY_READY

Digital timing control

HSR   HSR

| V S R | V M U X | 504X1500 CMOS APS array | 504X1500 CMOS APS array | V M U X | V S R |

Video AMP | CDS | CDS | Video AMP

Analog Video_L   Analog Video_R

(b)

Input light

APS ciruit

CDS

V-Amp

ADC

Digital output

Analog output

Cell stage   Column stage   Output stage

(a)
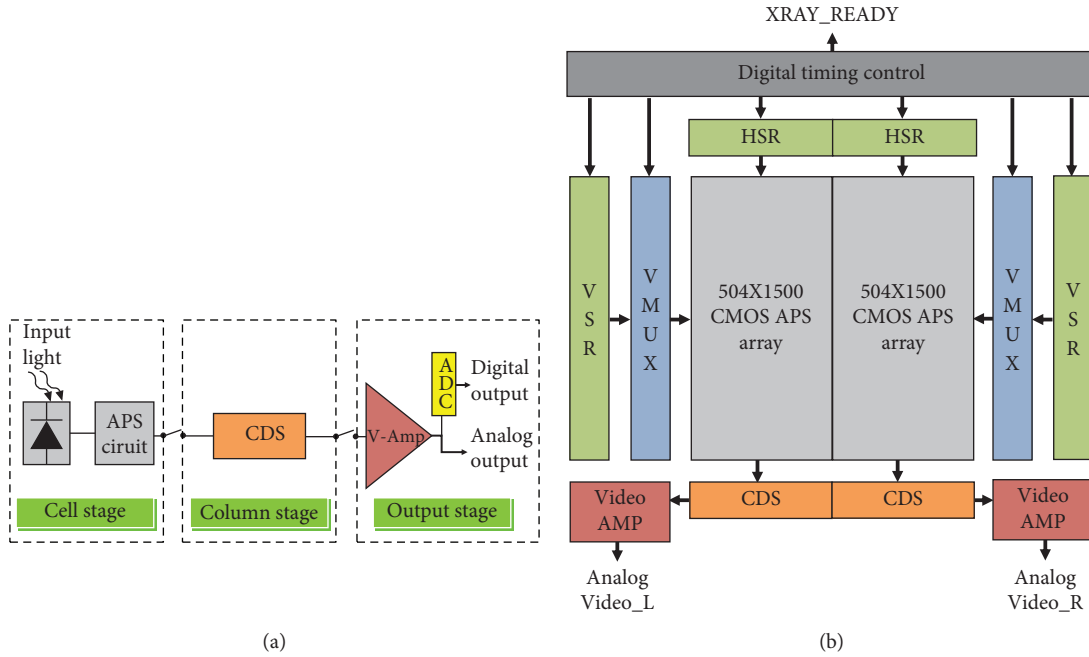
FIGURE 4: (a) CMOS image sensor signal processing flow chart and (b) architecture of the chip export signals.

circuit that includes an analog circuit and a digital circuit. The analog circuit processes optical signals and includes four electric circuit modes, namely, a photon-to-electron transformation circuit (active pixel sensor (APS)), pixel signal collection circuit (correlated double sampling (CDS)), pixel signal amplification circuit (video output amplifier (V-Amp)), and analog-to-digital conversion circuit (ADC). CMOS image sensing utilizes the photoelectric effect to excite electrons in the silicon crystal from the valence to conduction bands, and the optical signal strength is measured by the amount of photocurrent generated during the process. The CMOS image sensor uses the N+-to-PSUB PN interface as a light sensor. Figure 4(a) shows a flow chart of the signal processing of the CMOS image sensor. The architecture of the CMOS chip signal export is illustrated in Figure 4(b). To improve the image export rate, the chip signal is synchronously processed by a dual-channel setting and exported through Analog Video_L and Analog Video_R. Regarding the circuit of the AD9244 analog-to-digital converter in the video processing board, V_Out1 is the chip output signal of one of the channels; however, it is also the input signal for the video processing board. After being transmitted through the sample-and-hold circuit, the signal is transmitted to the AD9244BSTZ-40 chip, and the final output digital image data format is 14 bits.

2.1.3. Video Processing Board. The chip imaging architecture requires a matching video processing board. The primary function of the matched video processing board is to output signals to the A/D converter chip on the external video processing board through the serial transmission of chipsets. Subsequently, the video processing board converts the signals into digital signals and transmits them through CameraLink, a high-speed data transmission interface, to output the image information to a computer for data storage. The image

output format is TIFF, the image size is 1000×1496 pixels with a pixel size of $20\,\mu$m, and the image format is 14 bits. Another function of the video processing board is to synchronously control the X-ray tube. Because the video processing board controls the X-ray tube exposure, the board also controls the synchronization timing of the chipset exposure, meaning that the chipset and X-ray tube can be synchronously activated to accurately control the chipset and begin receiving signals. Table 1 lists the characteristic features of the developed high-frame-rate intraoral periapical sensor.

2.2. Quantitative Performance of the High-Frame-Rate Intraoral Periapical Sensor. The developed intraoral periapical sensor was also used to capture images of two phantoms to verify image quality. The phantoms were line pairs. From the images of the line pairs, the calculated modulation transfer function (MTF) could be used to measure the actual resolution of the sensor.

2.3. Applying the High-Frame-Rate Intraoral Periapical Sensor in the Prototype 2.5D Periapical Radiography System. We installed the high-frame-rate intraoral periapical sensor on our previously developed 2.5D periapical radiography system prototype (Figure 5) [13]. The image sample was a human third molar. For details regarding the prototype, refer to our previous study [13]. The scanning parameters were as follows: distance between the X-ray source and rotation axis was 350 mm; distance between the sensor and rotation axis was 5 mm; the voltage was 80 kVp; the current was 5 mA; exposure time was 0.2 second; the angle of the X-ray tube was ±30°; and images were taken every 2°. A total of 31 images were taken, and these 31 2D projection images were used to reconstruct images through tomosynthesis.

TABLE 1: The characteristic features of the high-frame-rate intraoral periapical sensor. Measurements of trabecular bone microarchitectural parameters based on the micro-CT and dental CBCT images.

Number	Item	Specification
1	Process	UMC 0.35 μm CIS with stitching (8 inches)
2	Frame resolution	1008×1500
3	Sensitive area	$20.16\,\mathrm{mm} \times 30\,\mathrm{mm}$
4	Pixel size	$20\,\mu$m
5	Output type	Serial
6	Interface (chip to video processing board)	Analog
7	Interface (video processing board to system)	CameraLink
8	Color	Gray
9	Frame rate (max)	≤15 Hz
10	Pixel data rate	15 MHz
11	Pixel sampling resolution	16384 (14 bits)
12	Voltage	3.3 V
13	Power of chip	165 mW
14	Number of pads	68
15	Chip size	$20.68\,\mathrm{mm} \times 32.92\,\mathrm{mm}$
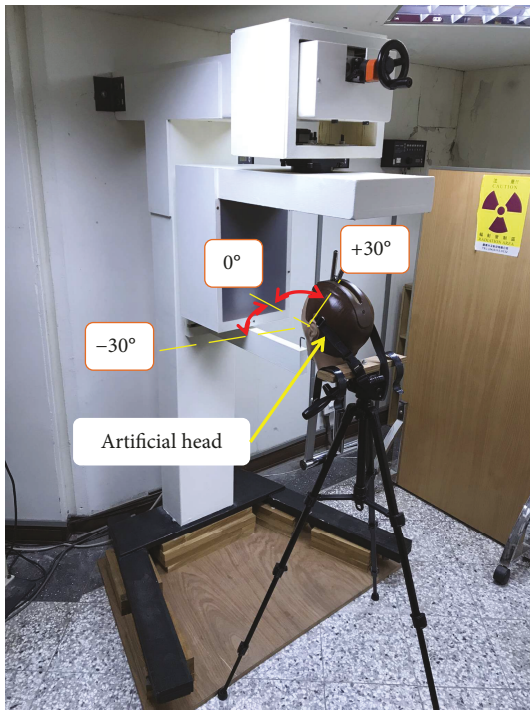
FIGURE 5: 2.5D periapical radiography system and X-ray tube scanning ranges.

3. Results

3.1. The Performance of the High-Frame-Rate Intraoral Periapical Sensor. This high-frame-rate intraoral periapical sensor utilized two methods for image quality evaluation, namely, line pairs and an aluminum step wedge. From the line pair images (Figure 6(a)), image quality was quantized using the MTF, the value of which was lower than 0.09 at

19 lp/mm (Figure 6(b)); thus, the resolution of the developed intraoral periapical sensor was 18 lp/mm.

3.2. The Performance of the 2.5D Periapical Radiography System Using the High-Frame-Rate Intraoral Periapical Sensor. The high-frame-rate intraoral periapical sensor was installed in the 2.5D intraoral periapical sensor prototype designed by our research team. The X-ray tube scanned the 2D projection images of the human third molar at an angle of 30°. Figure 7 illustrates that the more the X-ray tube deviates from the orthogonal axis (0°) of the sensor, the more severe the deformation of the 2D projection images becomes. At ±30°, an image was captured every 2°, for a total of 31 images taken in approximately 4 s. Clear outlines of the dentin and enamel of the third molar can be observed in each of the 2D projection images; thus, the outline was not distorted or blurred when shooting at a high frame rate.

The 2D projection images captured by the X-ray tube at 0° were equivalent to the images captured using clinical periapical film. In images captured using periapical film, 3D images of tissue are compressed into a 2D image (Figure 8(a)). Figures 8(b)–8(d) present the reconstructed images utilizing the 31 2D projection images taken of the third molar at different depths. These images display the anteroposterior relationship between different parts of the molar, and the structure of the internal tissue, such as the dentin, enamel, and pulp cavity, is also present in the images. These images provide more information regarding the molar than the 2D periapical film image does (Figure 8(a)).

4. Discussion

Our research team previously conducted in vitro tests to verify the feasibility of our 2.5D periapical radiography system [13]. By using an X-ray tube, an intraoral periapical sensor, a supporting frame, and electronic control equipment, we

(a)

(b)

(c)
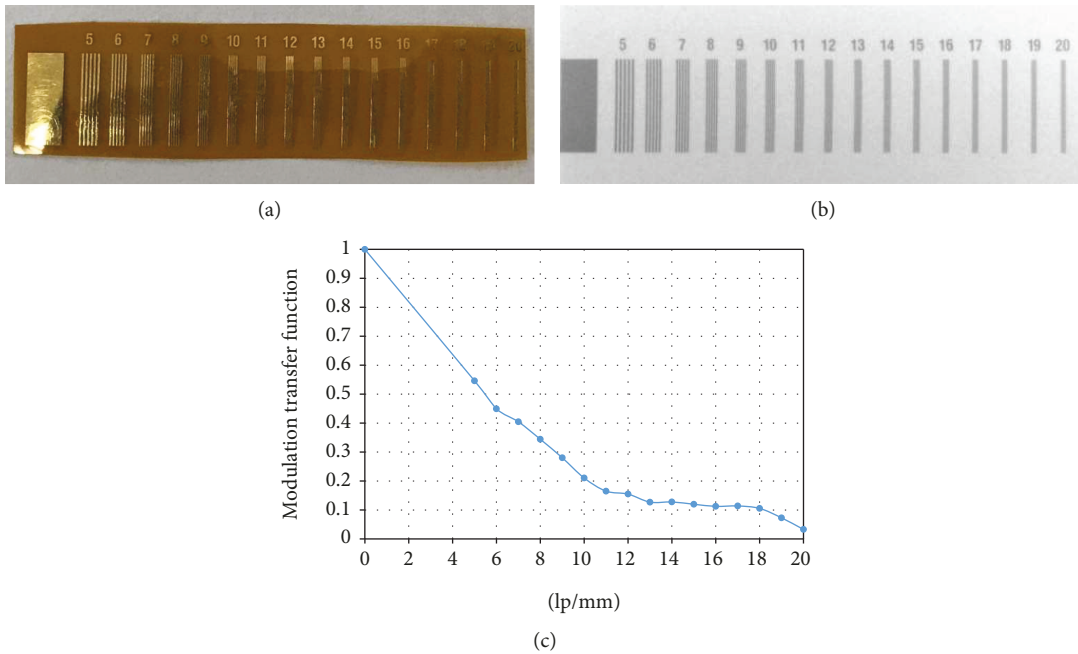
Figure 6: (a) The line pair phantom, (b) the image of the line pair phantom, and (c) the curve of modulation transfer function.
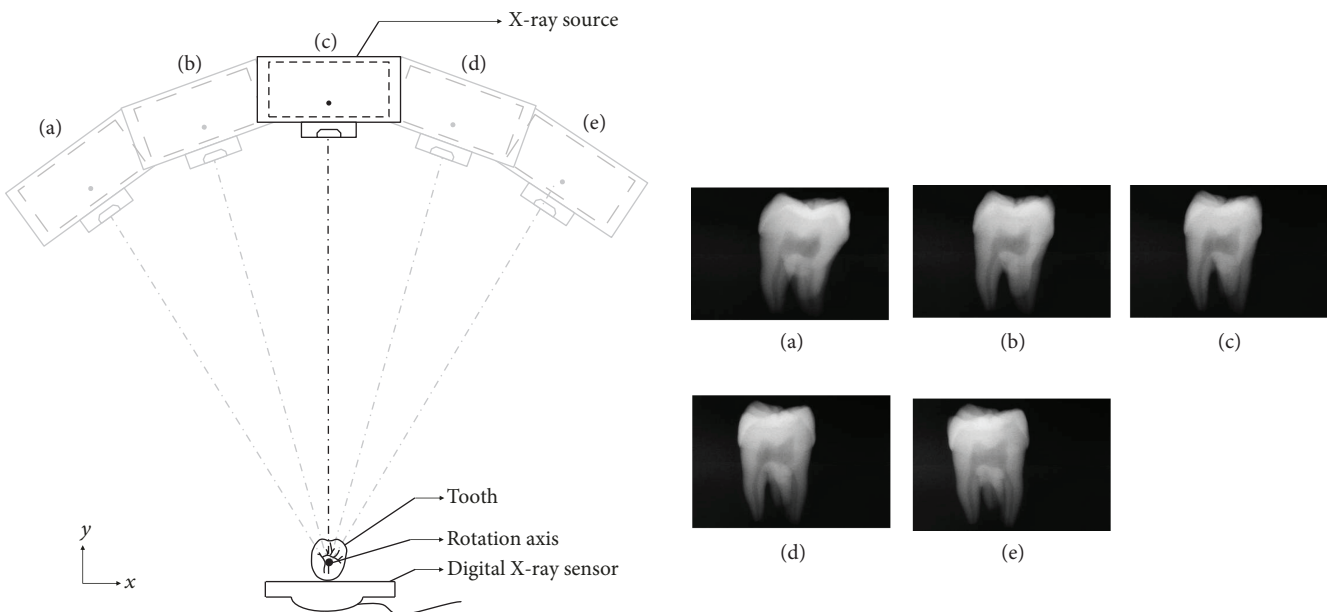
Figure 7: X-ray tube captures 2D projection images of the third molar at different angles.

captured multiple 2D projection images of a tooth. These projection images were used to reconstruct images by adopting tomosynthesis to obtain slice images of different depths of the tooth. Images captured using this method provided more image information than those captured with conventional periapical film, and the images from the 2.5D periapical radiography system were not affected by the image superposition that occurs with a 2D periapical film. However, we also found that the 2.5D periapical radiography system prototype was unsuitable for current clinical applications because the temporal resolution of the commercially

available intraoral periapical sensor was low and the sensor required a few seconds between each shot, resulting in an overall shooting time of tens of minutes. Therefore, the present study developed a high-frame-rate intraoral periapical sensor with a frame rate of up to 15 Hz. The preliminary test results indicated that the system could perform a tomosynthesis scan of ±30° in only 4 s, which greatly improves the potential for clinical application of our 2.5D periapical radiography system.

Periapical film has the advantages of high resolution, easy operation, and low costs [6]; however, its ultimate limitation
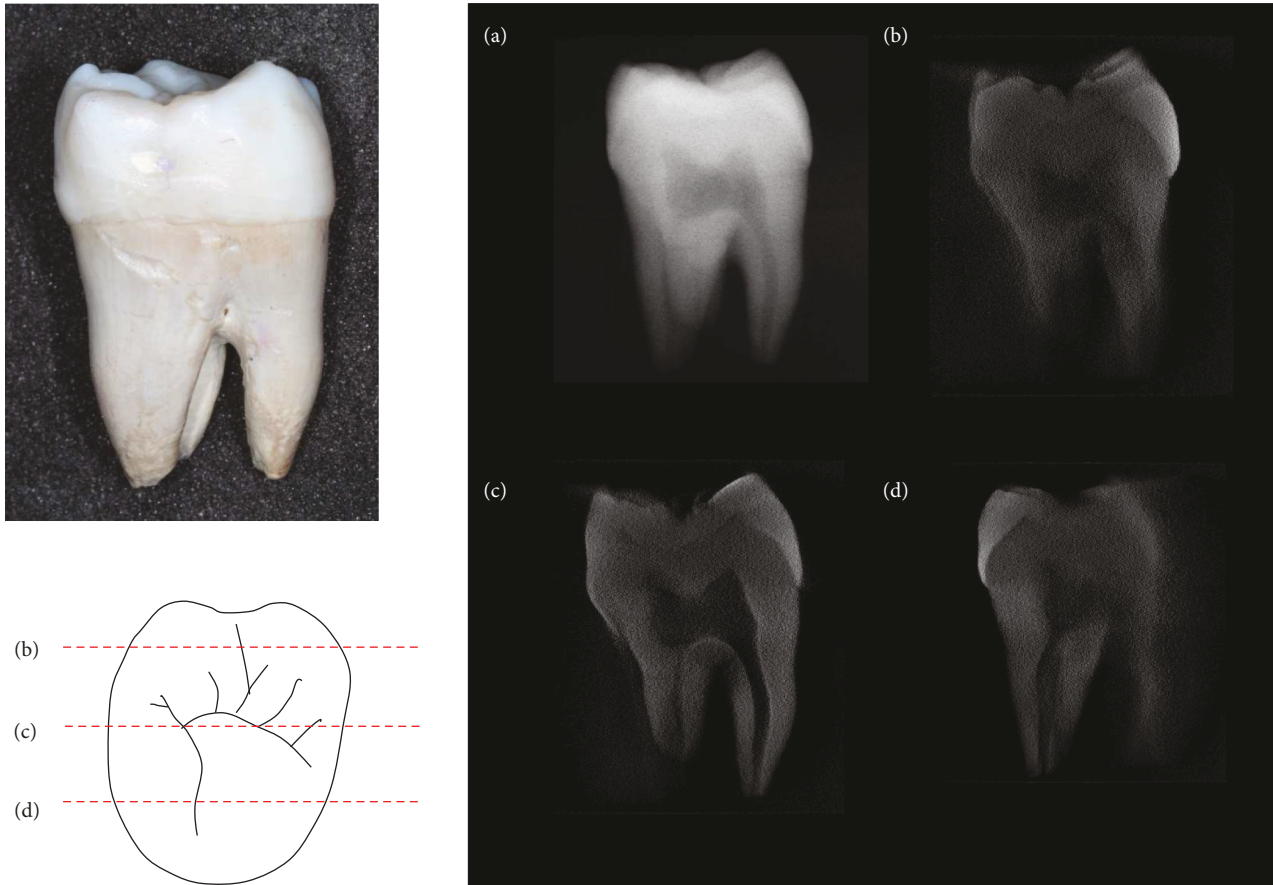
FIGURE 8: (a) Periapical radiology image of the third molar and (b–d) the reconstructed slice images at different depths from the sensor surface.

is that it can only capture 2D images. Our research team previously showed the feasibility of a 2.5D periapical radiography system [13] using a commercial sensor (RVG6200-SIZE1, Carestream Dental, Stuttgart, Germany) and an X-ray tube of ±60° to obtain 2D projection images every 1°. The obtained 2D projection images of a canine were then used to reconstruct images of the canine at different depths. The reconstructed images obtained using tomosynthesis were similar to those obtained by using an X-ray tube to perform 360° scanning incorporating the background projection method; the dentin and enamel outlines could be distinguished in the images. In a previous study [13], we demonstrated that tomosynthesis could be applied to dentistry. As early as 1996, Webber et al. [19] had already used an intraoral CCD X-ray transducer to indicate that tomosynthesis might be applicable to dentistry. In 2013, Li et al. [7] constructed a desktop intraoral digital tomosynthesis system in the laboratory and conducted an experiment on a pig mandible. By placing a sensor in the posterior mandible, the results of their study also indicated the feasibility of tomosynthesis in dentistry. Currently, tomosynthesis is mostly applied to mammography [15] [20], with no commercially available products found in dentistry. A possible reason for this is that no high-frame-rate intraoral periapical sensor currently exists. Therefore, this study sought to develop such a sensor.

Currently, high-frame-rate sensors with imaging speeds of up to 10 Hz are available [21, 22]; however, these are mostly used in CT, dental CBCT, or micro-CT [23–25]. Moreover, these sensors are at least 12×7 or 15×15 cm^2, which means they are too large to be placed in the mouth. Intraoral periapical sensors used in modern dentistry are not designed for high-frame-rate capture; thus, manufacturers do not provide information on maximum sensor frame rates. Our previous study found that interval between shots of less than 5 s using a commercial sensor led the system to overheat. Therefore, development of a high-frame-rate intraoral periapical sensor is necessary if our 2.5D periapical radiography system is to be used for future clinical applications. In addition to use in our 2.5D periapical radiography system, the high-frame-rate intraoral periapical sensor developed in the present study can be applied to a micro-CT machine [13] or used in industrial quality management that requires capturing high-frame-rate images.

The line pair phantom was used in this study to quantify the image quality. According to the analysis results, the resolution of the intraoral periapical sensor was 18 lp/mm. In our previous study [13], we employed the RVG6200-SIZE1 commercial intraoral digital sensor (Carestream Dental, Stuttgart, Germany) to build a prototype 2.5D periapical radiography system. The line pair phantoms were used to

measure the resolution of the commercial sensor, with a result of 18 lp/mm, which was similar with the developed high-frame-rate intraoral periapical sensor. Figure 7 displays 2D projection images of the third molar captured by the X-ray tube at different angles. Because the high-frame-rate intraoral periapical sensor was fixed in place, the larger the shooting angle of the X-ray tube was, the more severe the image distortion of the teeth became. However, the outlines and boundaries of the dentin and enamel on these distorted images could still be identified. These projection images were taken by the moving X-ray tube, and due to the high-frame-rate capture, each image was blur free.

In this study, the images reconstructed from the 31 2D projection images using tomosynthesis revealed slice images of the third molar at different depths (Figures 8(b)–8(d)). Compared with 2D periapical film images (Figure 8(a)), the images captured using the new method obtained more information from the tooth, and the images were unaffected by compression of the 3D structure of the tissue into a 2D periapical film image (Figure 8(a)), meaning that the images could still show the anteroposterior relationship of the tooth. Mammography also uses tomosynthesis to capture images by scanning at limited angles to obtain reconstructed images [26, 27]; these limited angles mean that the reconstructed slice images are not always clear. The farther from the rotation axis the slice images are taken, the more blurred the slice images become.

In this study, the milliampere seconds per projection was 1.0 mAs for a total exposure of 31 mAs, which is twice of the 15.75 mAs achieved by the previous stationary intraoral digital tomosynthesis system developed by Shan et al. [10]. However, the X-ray tube output for the total exposure in the present study (31 mAs) was half that of another digital tomosynthesis system developed by Ziegler et al. [9], which was 67.2 mAs. Regardless, the X-ray tube output of all intraoral digital tomosynthesis systems should be much less than that of dental CBCT.

The frame rate of a CMOS sensor can be affected by many factors, such as pixel size, X-ray output power, and design of the sensor (e.g., fill factor, quantum efficiency, and signal processing). The intraoral periapical sensor developed in the present study could capture images at 15 Hz, which was sufficient for our 2.5D periapical radiography system. In addition, from the experimental results, the image quality of the intraoral periapical sensor developed in this study was of reasonable quality. However, several aspects should be refined for potential clinical use. The primary concern is that this study used a single tooth to conduct the experiment; thus, no bones or other teeth around the tooth were present to interfere with the images. However, if the system is applied to clinical use, the sensor will be placed in the patient's mouth, which means that there will be many bones and hard tissue of adjacent teeth around the target tooth. This makes the shooting conditions more complex than that of a single tooth. More robust experiments should be performed to verify whether the shooting conditions affect the image quality. In addition, the scanning region of this system is smaller than that of a 2D periapical X-ray due to the X-ray tube requiring exposure in different positions (e.g., a range

between ±30°), resulting in the scanning width being less than approximately 80% of the 2D periapical X-ray. Furthermore, the computer operation interface of the high-frame-rate intraoral periapical sensor is relatively complicated; the interface should be improved to increase user friendliness in the future, making system operation easier for dentists and medical image radiologists.

5. Conclusion

The developed high-frame-rate intraoral periapical sensor requires further improvement for use in capturing images in a patient's mouth. However, the sensor can greatly reduce shooting time using our 2.5D periapical radiography system to less than 5 s, proving its potential for use in future clinical applications.

Data Availability

The datasets generated during the current study are available from the corresponding author on reasonable request.

Conflicts of Interest

The authors declare that they have no competing interests.

Authors' Contributions

The fifth author and sixth author equally contributed to this work.

Acknowledgments

References

[1] N. Shah, N. Bansal, and A. Logani, "Recent advances in imaging technologies in dentistry," *World Journal of Radiology*, vol. 6, no. 10, pp. 794–807, 2014.

[2] B. Vandenberghe, R. Jacobs, and H. Bosmans, "Modern dental imaging: a review of the current technology and clinical applications in dental practice," *European Radiology*, vol. 20, no. 11, pp. 2637–2655, 2010.

[3] H. G. Chotas, J. T. Dobbins III, and C. E. Ravin, "Principles of digital radiography with large-area, electronically readable detectors: a review of the basics," *Radiology*, vol. 210, no. 3, pp. 595–599, 1999.

[4] J. A. Seibert, "Digital radiography: the bottom line comparison of CR and DR technology," *Applied Radiology*, vol. 38, no. 5, pp. 21–29, 2009.

[5] T. Kiljunen, T. Kaasalainen, A. Suomalainen, and M. Kortesniemi, "Dental cone beam CT: a review," *Physica Medica*, vol. 31, no. 8, pp. 844–860, 2015.

[6] E. Metsälä, A. Henner, and M. Ekholm, "Quality assurance in digital dental imaging: a systematic review," *Acta Odontologica Scandinavica*, vol. 72, no. 5, pp. 362–371, 2014.

[7] L. Li, Z. Chen, Z. Zhao, and D. Wu, "X-ray digital intra-oral tomosynthesis for quasi-three-dimensional imaging: system, reconstruction algorithm, and experiments," *Optical Engineering*, vol. 52, no. 1, article 013201, 2013.

[8] C. C. L. Wyatt and M. J. Pharoah, "Imaging techniques and image interpretation for dental implant treatment," *International Journal of Prosthodontics*, vol. 11, no. 5, 1998.

[9] C. M. Ziegler, M. Franetzki, T. Denig, J. Mühling, and S. Hassfeld, "Digital tomosynthesis-experiences with a new imaging device for the dental field," *Clinical Oral Investigations*, vol. 7, no. 1, pp. 41–45, 2003.

[10] J. Shan, A. W. Tucker, L. R. Gaalaas et al., "Stationary intraoral digital tomosynthesis using a carbon nanotube X-ray source array," *Dentomaxillofacial Radiology*, vol. 44, no. 9, article 20150098, 2015.

[11] C. R. Inscoe, E. Platin, S. M. Mauriello et al., "Characterization and preliminary imaging evaluation of a clinical prototype stationary intraoral tomosynthesis system," *Medical Physics*, vol. 45, no. 11, pp. 5172–5185, 2018.

[12] C. R. Inscoe, G. Wu, D. E. Soulioti et al., "Stationary intraoral tomosynthesis for dental imaging," in *Medical Imaging 2017: Physics of medical imaging*, Orlando, Florida, USA, March 2017.

[13] C. W. Liao, C. J. Hsieh, H. L. Huang et al., "Prototype of a 2.5D periapical radiography system using an intraoral computed tomosynthesis approach," *Biomedical Engineering: Applications, Basis and Communications*, vol. 30, no. 1, article 1850004, 2018.

[14] M. Abreu Jr., L. Yi-Ching, and A. L. Abreu, "Comparative diagnostic performance of TACT® slices and its multiple source images: an in vitro study," *Dentomaxillofacial Radiology*, vol. 33, no. 2, pp. 93–97, 2004.

[15] O. Olsen and P. C. Gøtzsche, "Cochrane review on screening for breast cancer with mammography," *The Lancet*, vol. 358, no. 9290, pp. 1340–1342, 2001.

[16] M. Martínez-Alonso, M. Carles-Lavila, M. J. Pérez-Lacasta et al., "Assessment of the effects of decision aids about breast cancer screening: a systematic review and meta-analysis," *BMJ Open*, vol. 7, no. 10, article e016894, 2017.

[17] D. G. Grant, "Tomosynthesis: a three-dimensional radiographic imaging technique," *IEEE Transactions on Biomedical Engineering*, vol. BME-19, no. 1, pp. 20–28, 1972.

[18] D. W. Holdsworth and M. M. Thornton, "Micro-CT in small animal and specimen imaging," *Trends in Biotechnology*, vol. 20, no. 8, pp. S34–S39, 2002.

[19] R. L. Webber, R. A. Horton, T. E. Underhill, J. B. Ludlow, and D. A. Tyndall, "Comparison of film, direct digital, and tuned-aperture computed tomography images to identify the location of crestal defects around endosseous titanium implants," *Oral Surgery, Oral Medicine, Oral Pathology, Oral Radiology, and Endodontology*, vol. 81, no. 4, pp. 480–490, 1996.

[20] S. Suryanarayanan, A. Karellas, S. Vedantham et al., "Evaluation of linear and nonlinear tomosynthetic reconstruction methods in digital mammography," *Academic Radiology*, vol. 8, no. 3, pp. 219–224, 2001.

[21] Q. Cao, A. Sisniega, M. Brehler et al., "Modeling and evaluation of a high-resolution CMOS detector for cone-beam CT of the extremities," *Medical Physics*, vol. 45, no. 1, pp. 114–130, 2018.

[22] A. Jain, H. Takemoto, M. D. Silver et al., "Region-of-interest cone beam computed tomography (ROI CBCT) with a high resolution CMOS detector," in *Medical Imaging 2015: Physics of Medical Imaging*, vol. 9412, Orlando, Florida, USA, March 2015.

[23] R. Baba, K. Ueda, and M. Okabe, "Using a flat-panel detector in high resolution cone beam CT for dental imaging," *Dentomaxillofacial Radiology*, vol. 33, no. 5, pp. 285–290, 2004.

[24] G. Cao, Y. Z. Lee, R. Peng et al., "A dynamic micro-CT scanner based on a carbon nanotube field emission x-ray source," *Physics in Medicine & Biology*, vol. 54, no. 8, pp. 2323–2340, 2009.

[25] W. A. Kalender and Y. Kyriakou, "Flat-detector computed tomography (FD-CT)," *European Radiology*, vol. 17, no. 11, pp. 2767–2779, 2007.

[26] L. T. Niklason, B. T. Christian, L. E. Niklason et al., "Digital tomosynthesis in breast imaging," *Radiology*, vol. 205, no. 2, pp. 399–406, 1997.

[27] T. Wu, R. H. Moore, E. A. Rafferty, and D. B. Kopans, "A comparison of reconstruction algorithms for breast tomosynthesis," *Medical Physics*, vol. 31, no. 9, pp. 2636–2647, 2004.

Research Article

Host Mesh Fitting of a Generic Musculoskeletal Model of the Lower Limbs to Subject-Specific Body Surface Data: A Validation Study

Katja Oberhofer [ID],[1] **Silvio Lorenzetti** [ID],[1,2] **and Kumar Mithraratne** [ID][3]

[1]*Institute for Biomechanics, Department of Health Sciences and Technology, ETH Zurich, Leopold-Ruzicka-Weg 4,*
 8093 Zürich, Switzerland
[2]*Swiss Federal Institute of Sport, Magglingen, Switzerland*
[3]*The Bioengineering Institute, University of Auckland, Auckland, New Zealand*

Correspondence should be addressed to Katja Oberhofer; katja.oberhofer@hest.ethz.ch

Challenges remain in accurately capturing the musculoskeletal geometry of individual subjects for clinical and biomechanical gait analysis. The aim of this study was to use and validate the Host Mesh Fitting (HMF) technique for fitting a generic anatomically based musculoskeletal model to 3D body surface data of individual subjects. The HMF technique is based on the free-form idea of deforming geometrically complex structures according to the deformation of a surrounding volumetric mesh. Using the HMF technique, an anatomically based model of the lower limbs of an adult female subject (29 years) was customized to subject-specific skin surface data of five typically developing children (mean age 10.2 years) and six children with Cerebral Palsy (CP) (mean age 9.6 years). The fitted lengths and volumes of six muscle-tendon structures were compared against measures from Magnetic Resonance (MR) images for validation purposes. The HMF technique resulted in accurate approximations of the lower limb shapes of all subjects in both study groups. The average error between the MR data and the fitted muscle-tendon lengths from HMF was $4 \pm 4\%$ in children without CP and $7 \pm 5\%$ in children with CP, respectively. The average error between the MR data and the fitted muscle volumes from HMF was $28 \pm 19\%$ in children without CP and $27 \pm 28\%$ in children with CP, respectively. This study presents a crucial step towards personalized musculoskeletal modelling for gait analysis by demonstrating the feasibility of fitting a generic anatomically based lower limb model to 3D body surface data of children with and without CP using the HMF technique. Additional improvements in the quality of fit are expected to be gained by developing age-matched generic models for different study groups, accounting for subject-specific variations in subcutaneous body fat, as well as considering supplementary data from ultrasound imaging to better capture physiological muscle tissue properties.

1. Introduction

Computer models of the musculoskeletal system have widely been applied to biomechanical and clinical gait analysis. Musculoskeletal modelling has provided means to quantify muscle and joint function during walking that cannot be measured otherwise. In particular, muscular weaknesses or bilateral asymmetries can result in altered and potentially harmful internal tissue loading which cannot be investigated based on external observation alone. By combining data from optical motion capture with computational models of the musculoskeletal system, crucial insights have been gained into, e.g., muscle-tendon length changes during walking in patients with Cerebral Palsy (CP) to help in the targeted treatment intervention [1], as well as served as intermediate step for calculating muscle-tendon forces and joint loading to assist with rehabilitation intervention and monitoring [2].

Generic musculoskeletal models of the lower limbs have traditionally been adopted and crudely scaled to subject-specific dimensions in order to analyze biomechanical

parameters such as joint forces, muscle-tendon lengths, or lengthening velocities during gait for individual subjects [1, 3, 4]. Thereby, the term "generic" refers to a reference model or data set, commonly resembling the anatomy of an adult male or female subject without musculoskeletal injury or disease. In recent years, more advanced optimization algorithms have been introduced in an effort to improve the accuracy of musculoskeletal modelling results for personalized gait analysis [5–8]. Yet, the most widely used fitting algorithms remain based on the positions of bony anatomical landmarks, assuming that the skeletal system sufficiently reflects the subject-specific architecture of the entire musculoskeletal system.

There is growing evidence that the fitting of musculoskeletal models based on bony anatomical landmarks may lead to incorrect conclusions, especially for clinical gait analysis in patients with severe musculoskeletal impairments due to conditions such as CP. Muscle architecture has been found to be significantly altered due to CP [9–11], and bone deformities, commonly observed in children with CP, have been shown to significantly affect joint kinematics, muscle-tendon lengths, and muscle moment arms during walking [12, 13]. Furthermore, bone deformities in the distal segments have been related to altered joint kinematics in the proximal joints and vice versa [14], and changes in the path of one muscle-tendon structure may affect the paths of neighboring muscles and hence the dynamics of the entire multibody musculoskeletal system. Such local differences in musculoskeletal architecture cannot be captured using generic musculoskeletal models that are simply scaled based on the positions of bony anatomical landmarks.

Magnetic Resonance (MR) and ultrasound imaging provide additional insights into the musculoskeletal architecture of individual subjects and have been considered for application to clinical gait analysis. Novel algorithms have been developed to automatically segment MR images based on previous knowledge from generic image data sets [15, 16]; and fitting techniques have been introduced to morph generic models of individual organs to a limited number of subject-specific MR images [17–19]. Yet, the implementation of image-based fitting algorithms to widespread clinical practice has often been a challenge due to long acquisition times of MR imaging as well as high imaging and computational costs. The integration of ultrasound imaging to gait analysis is considered more feasible; yet, ultrasound imaging is confined to a small imaging field of view, e.g., calf muscles, and thus requires additional means of fitting the entire multibody musculoskeletal system to individual subjects [20].

The aim of this study was to use a free-form deformation technique known as Host Mesh Fitting (HMF) for fitting generic musculoskeletal models to 3D body surface data of individual subjects and assess its accuracy in an effort to address the persisting limitations in musculoskeletal modelling for personalized gait analysis. The HMF technique was initially introduced to develop subject-specific 3D models of individual organs [18] and was later applied and validated for predicting the deformation of muscle-tendon structures in the lower limbs during walking [21]. The present work extends on these previous efforts by aiming to fit a generic

musculoskeletal model of the lower limbs of an adult female subject to 3D body surface data of children with and without CP and compare the fitted lengths and volumes of six muscle-tendon structures with the subject-specific muscle-tendon lengths and volumes derived from MR data. The use of 3D body surface data and HMF for fitting musculoskeletal models to individual subjects is expected to be particularly suited for gait analysis in population groups where bony anatomical landmarks are not sufficiently accurate and MR scanning not applicable due to time, cost, or ethical constraints.

2. Materials and Methods

2.1. Volumetric Host Mesh Fitting. In the following, the theoretical principles of the HMF technique are summarized. Given a generic 3D model of the musculoskeletal system with embedded tissue structures (e.g., muscles-tendon structures and bones of the lower limbs) and subject-specific skin surface data, the HMF process is divided into four steps (Figure 1).

In Step I "Model registration," the generic lower body mesh is aligned and homogenously scaled to subject-specific dimensions by calculating an overall affine transformation matrix using the conventional positions of bony anatomical landmarks. The affine transformation matrix comprises rotation, scaling, shearing, and translation and is obtained by minimizing the distances between bony anatomical landmarks of the generic model and manually annotated subject-specific bony landmarks. In Step II "Recording local muscle position," the material positions of the muscle-tendon structures of the generic model are calculated with respect to the surrounding 3D lower body mesh in preparation for skin mesh fitting. In Step III "Data fitting of skin mesh," the registered lower body mesh is customized to subject-specific 3D body surface data to find the optimum mesh nodal degrees of freedom (i.e., mesh nodal parameters, including nodal positions as well as nodal derivatives in the case of bicubic-linear interpolation functions). In brief, the HMF objective function $F(\mathbf{u}_n)$ is set up to find the optimum mesh nodal parameters $\mathbf{u}_n$ that minimize the Euclidean distances between the subject-specific data points and their projections onto the lower body mesh in a least-square sense as follows:

$$F(\mathbf{u}_n) = \sum_{d=1}^{D} \left(\sum_{n=1}^{N} [\varphi_n(p_d)\mathbf{u}_n] - s_d \right)^2 + \delta(\mathbf{u}_n, \gamma_i), \quad (1)$$

whereby p_d denotes the coordinates of the projection points $d = 1, \ldots, D$ with respect to the lower body mesh, and s_d is the corresponding global coordinates of the subject-specific target points, and $\delta(\mathbf{u}_n, \gamma_i)$ is a 3D smoothing constraint called Sobolev function with user-defined penalty parameters $\gamma_i \in [0, 1]$ for controlling arc lengths, curvatures in element coordinate directions, surfaces area terms, and volume of the lower body mesh. Further details to the HMF objective function and 3D smoothing constraints can be found in [18, 21]. Finally,
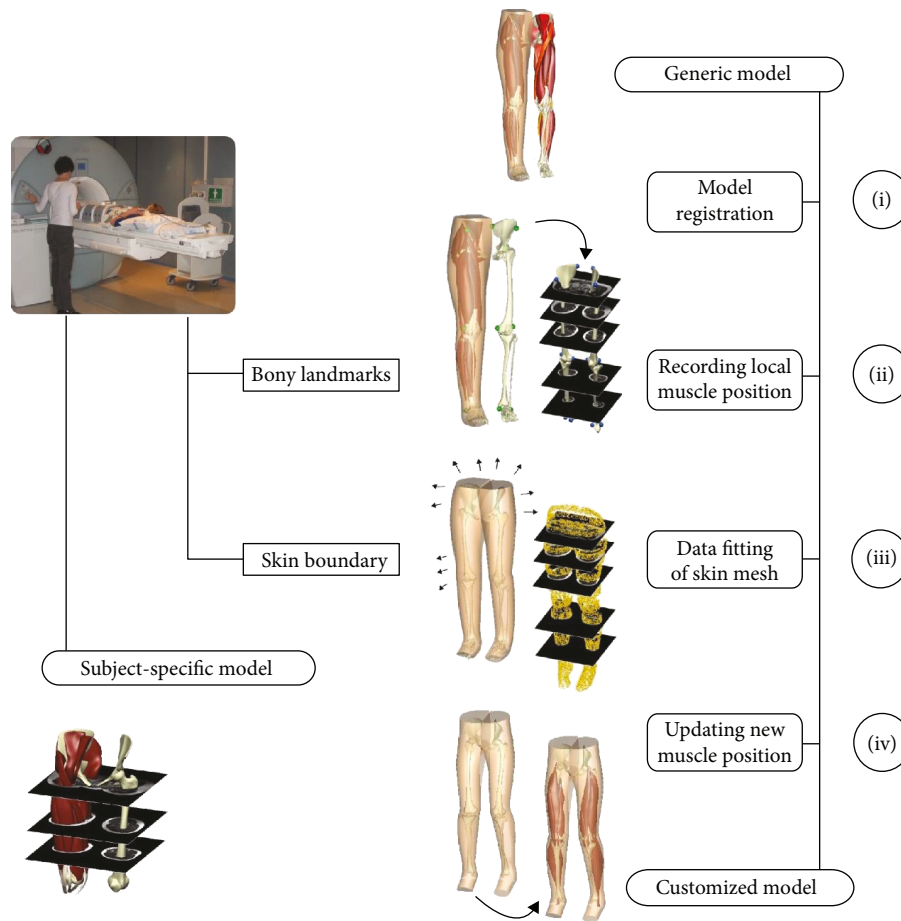
FIGURE 1: The HMF technique is divided into four steps: (I) model registration based on bony landmarks; (II) recording of muscle-tendon nodal parameters with respect to generic lower body mesh; (III) customization of lower body mesh to subject-specific body shape data; and (IV) updating muscle-tendon nodal parameters according to customized skin mesh. Previously acquired MR images of children with and without CP [11] were used for validation purposes in the present work.

in Step IV "Updating new muscle position," the spatial positions of the muscle-tendon structures are calculated according to the customized position of the lower body mesh. This is carried out under the assumption that the material positions of the muscle-tendon structures with respect to the surrounding 3D lower body mesh do not change during customization.

The HMF algorithm is implemented in the modelling environment CMISS (http://www.cmiss.org). CMISS is an interactive computational modelling environment for Continuum Mechanics, Image analysis, Signal processing, and System identification, which has extensively been used for high-order subject-specific modelling of the musculoskeletal system [11, 18, 21, 22]. CMISS has been developed as part of the International Union of Physiological Sciences (IUPS) Physiome Project [17, 19] and is currently being redeveloped into the open source package Open-CMISS to make it more modular, extendable, easier to understand, and able to run on modern distributed-memory high-performance computers (http://www.opencmiss.org).

2.2. Validation. The accuracy of the HMF technique was assessed by fitting a generic lower limb model to subject-specific data of children with and without CP and comparing the predicted muscle-tendon lengths and volumes of the fitted model with subject-specific MR data. A generic lower limb model of an adult female subject, which was previously manually developed based on subject-specific MR data [21], was used (age 29 y, height 165 cm, and weight 63 kg) for this purpose. The lower limb model comprised all lower limb bones, 20 muscles-tendon structures, and a volumetric representation of the skin boundary surface of each leg. All geometries of the musculoskeletal lower limb model were represented using high-order finite element meshes with bicubic-linear interpolation functions. Cubic interpolation functions preserve the continuity of the first derivatives of the geometric coordinates with respect to the element coordinates, which makes them ideal for smoothly approximating the curved surfaces of biological tissue with a minimum number of elements [21].

MR images of the lower limbs of six children with CP (mean age 9.6 years) and five typically developing children (mean age 10.2 years) were acquired on a Siemens 1.5T MAGENTOM Avanto System. Ethical approval was given by the NZ Northern Y Regional Ethics Committee, reference number NTY/06/07/064. Written consent was obtained from

all children and their parents or guardians. Subject characteristics and scan protocol have previously been outlined in detail [11]. The image processing tools within CMISS were employed to automatically segment the skin boundary surfaces of the lower limbs. The positions of the following bony landmarks on the skin surface were manually identified according to standard protocols [23]: right/left asis, sacrum, medial/lateral epicondyles, and medial/lateral malleoli. The bony landmarks were used to register the generic model to the subject-specific surface data (Step I, Figure 1). The lower body mesh was then customized to subject-specific skin surface data and the new configuration of each muscle-tendon structure was calculated according to the customized lower body mesh (Steps II-IV, Figure 1).

Muscle-tendon lengths and volumes of the fitted models were numerically derived and compared with subject-specific measures from MR images for validation purposes. The following six muscles were included in the analysis: soleus, gastrocnemius, semimembranosus and semitendinosus (represented as one muscle), biceps femoris, and the vasti group. Muscle-tendon lengths were defined as the average arc lengths between the most distal and most proximal ends of the muscle-tendon meshes, normalized with respect to segmental lengths. Muscle volumes were derived by performing numerical quadrature over the parameterized meshes (Fernandez et al., 2005), divided by body mass. The fitting error E_{HMF} was defined as the relative difference in muscle-tendon length l, i.e., muscle volume V, between the fitted values from HMF and the subject-specific values derived from the MR images:

$$
\begin{aligned}
E_{\text{HMF}}^{l} &= \frac{|l_C - l_{\text{MRI}}|}{l_{\text{MRI}}}, \\
E_{\text{HMF}}^{V} &= \frac{|V_C - V_{\text{MRI}}|}{V_{\text{MRI}}}.
\end{aligned}
\tag{2}
$$

2.3. *Statistical Analysis.* Statistical analysis was performed to assess the significance of the differences in muscle-tendon lengths and volumes between the fitted and the subject-specific values from MR imaging. All parameters were tested for a normal distribution prior to data comparison using the Kolmogorov and Smirnov method [24]. A repeated measure analysis of variance (ANOVA) with Tukey-Kramer multiple post hoc test [25] was performed to analyze the pairwise differences in muscle-tendon lengths and volumes between the fitted and the subject-specific measures from MR imaging. The data of the children with CP and without CP were analyzed independently as two different groups. Statistical analysis was performed using the statistical software Graph-Pad IntStat. The level of significance was set at $p < 0.05$ for all statistical test.

3. Results

A generic lower limb model of an adult female subject was fitted to skin surface data of children with and without CP using the HMF technique. Eleven bony landmarks and an average number of 1,858,218 (±845) data points on the skin

boundary of each subject were used for the fitting process. The HMF technique resulted in smooth approximations of the lower body shapes of all subjects in both study groups (Figure 2). The average Root Mean Square (RMS) error between the fitted lower body mesh and the subject-specific surface data from MR imaging was 3.7 ± 1.08 mm.

The average normalized muscle-tendon lengths derived from HMF compared to the subject-specific values from MR images are given in Table 1. Statistical analysis revealed that HMF led to accurate predictions of muscle-tendon lengths in the children without CP for all muscles except rectus femoris. In the children with CP, HMF led to accurate predictions of muscle-tendon lengths for soleus, biceps femoris, and the vasti group, while significant differences were obtained between the fitted and the MR-based values for gastrocnemius, semimembranosus-semitendinosus, and rectus femoris. The average fitting error (equation (2)) in muscle-tendon lengths from HMF was 4 ± 4% in the group of children without CP and 7 ± 5% in the children with CP, respectively.

The average normalized muscle volumes derived from HMF compared to the subject-specific values from MR images are given in Table 2. Overall, the prediction of muscle volumes was poor, with an average fitting error (equation (2)) of 28 ± 19% in children without CP and 27 ± 28% in children with CP, respectively. Statistical analysis revealed significant differences in the predicted muscle volumes from HMF compared to MR imaging for four muscles in the children without CP (soleus, biceps femoris, rectus femoris, and vasti group) and for two muscles in the children with CP (biceps femoris, semimembranosus-semitendinosus).

4. Discussion

The aim of this study was to address current limitations in subject-specific musculoskeletal modelling for personalized gait analysis by applying and validating the HMF technique to fit a generic model to subject-specific 3D body surface data. The HMF technique extends scaling of generic musculoskeletal models based on bony anatomical landmarks in that it comprises an affine transformation (rotation, translation, and scaling) followed by model customization to account for subject-specific variations in lower limb shape. High accuracies were obtained in the fitted lower limb shapes in both study groups with the RMS error between the subject-specific 3D body surface data and the fitted lower limb mesh being less than 5 mm for all data points. The accuracies in muscle-tendon lengths are also considered promising for having the potential to improve gait analysis results, with an average RMS error of 4 ± 4% in the children without CP and 7 ± 5% in the children with CP, respectively (Table 1). The average RMS errors in muscle-tendon lengths in both study groups are below, or around the lower range, of previously reported errors in muscle-tendon length predictions using generic musculoskeletal models for clinical gait analysis, e.g., 6% to 50% [26]. However, the accuracies in muscle volumes were limited with large variations in both study groups compared to the subject-specific MR data (Table 2).
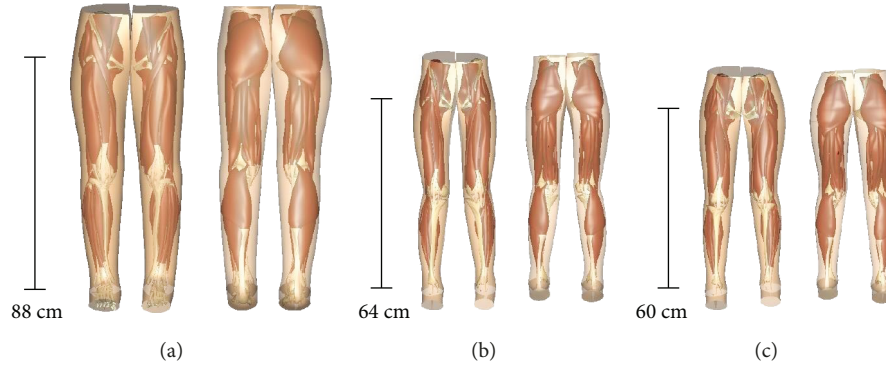
Figure 2: (a) The generic lower limb model based on the anatomy of an adult female (Oberhofer et al. 2009). (b) A fitted lower limb model of a child without CP. (c) A fitted lower limb model of a child with CP. Leg lengths of each model, ranging from the hip joint center to the ankle joint center, are given as reference.

Table 1: Average normalized muscle-tendon lengths (%) derived from the subject-specific MR images (MRI) compared to the predicted values from HMF for the children without CP and the children with CP.

	Children without CP			Children with CP		
	MRI	HMF	p value	MRI	HMF	p value
Soleus	71 (5.1)	71 (2.2)	>0.05	66 (4.7)	69 (2.3)	>0.05
Gastrocnemius	60 (5.8)	56 (3.6)	>0.05	51 (3.7)	55 (1.5)	<0.05*
Biceps femoris	58 (4.6)	60 (1.7)	>0.05	54 (3.7)	56 (4.8)	>0.05
Semi group	82 (3.3)	84 (3.7)	>0.05	76 (7.2)	81 (3.7)	<0.01*
Rectus femoris	76 (1.3)	79 (1.6)	<0.05*	68 (3.1)	75 (2.9)	<0.01*
Vasti group	91 (4.1)	91 (5.0)	>0.05	85 (2.1)	86 (2.7)	>0.05

*Difference between MRI and HMF statistically significant (repeated measures ANOVA with Tukey-Kramer multiple Comparison post hoc test, $p < 0.05$).

Table 2: Average muscle volumes (cm^3/kg) derived from the subject-specific MR images (MRI) compared to the predicted values from HMF for the children without CP and the children with CP.

	Children without CP			Children with CP		
	MRI	HMF	p value	MRI	HMF	p value
Soleus	5.5 (0.84)	3.9 (0.30)	<0.01*	4.5 (1.56)	3.7 (0.51)	>0.05
Gastrocnemius	4.4 (1.01)	3.6 (0.23)	>0.05	3.1 (1.26)	3.6 (0.56)	>0.05
Biceps femoris	2.3 (0.44)	3.5 (0.32)	<0.001*	1.6 (0.41)	3.5 (0.33)	<0.001*
Semi group	5.1 (0.91)	5.0 (0.30)	>0.05	3.9 (0.88)	5.5 (0.51)	<0.01*
Rectus femoris	3.6 (0.69)	2.2 (0.22)	<0.01*	2.6 (0.63)	2.3 (0.63)	>0.05
Vasti group	20.3 (2.80)	16.7 (1.16)	<0.05*	15.9 (3.20)	16.5 (2.58)	>0.05

*Difference between MRI and HMF statistically significant (repeated measures ANOVA with Tukey-Kramer multiple comparison post hoc test, $p < 0.05$).

The HMF technique is established under the assumption that the lower limb shape reflects the internal musculoskeletal architecture, which is a limitation of the proposed technique. It means that the relative positions of muscle-tendon structures with respect to the skin mesh remain constant during model fitting. If, for example, a thick subcutaneous fat layer between muscles and skin is present in the generic model, the relative thickness of the fat layer remains the same throughout HMF. Looking more closely at the MR images (Figure 3), it becomes apparent that significant differences existed in muscle volumes between individual subjects. In particular, children subjects

had less subcutaneous fat compared to the adult female subject, which could partly explain the unsatisfying prediction of muscle volumes compared to muscle-tendon lengths. Interestingly, the average RMS error for muscle volumes was slightly lower for the children with CP than the children without CP, which is an unexpected result (Table 2). Based on the MR images (Figure 3), it appears as if the percentage of muscle tissue versus fat tissue in children with CP more closely resembled the adult female anatomy, e.g., thicker fat layer with less muscle tissue, which may explain the unexpected outcome. Thereby, the volumetric tissue distribution critically affects the inertia properties of the multibody

Adult female subject

(a)

Child without CP

(b)

Child with CP

(c)
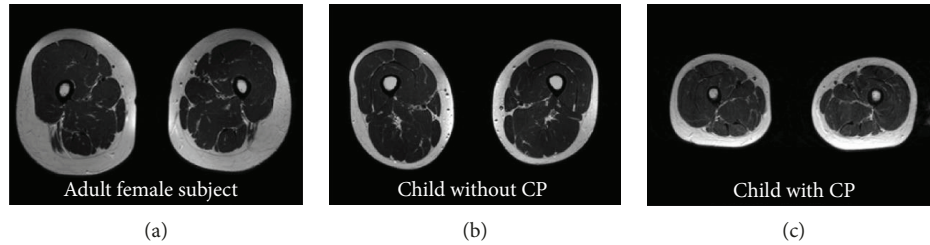
FIGURE 3: Representative MR image of the shank of (a) adult female subject, (b) child without CP, and (c) child with CP.

dynamic system and hence gait analysis results. These insights suggest that additional skin fold measurements may help to improve model fit by allowing to adjust the relative thickness of the fat layer, and thus segmental inertia properties, for individual subjects.

The time needed to develop musculoskeletal models by manually segmenting MR images is lengthy and can take several months. Currently, the modelling software CMISS contains a library of MR-based lower limb models of one female subject, six children with CP, and five typically developing children, which were adopted in the present work. The present goal to accurately fit a generic model of an adult female subject to the anatomy of children with severe gait impairments due to CP was ambitious. It is likely that more accurate results can be obtained when fitting the generic model to subjects of similar age and without significant musculoskeletal impairments. Nevertheless, the present results are promising and considered the first step towards an advanced modelling framework for subject-specific simulation and analysis of human movement. In addition to the MR-based lower limb models within CMISS, data from gait analysis was acquired in the same subjects. This unique dataset will allow the comparison of muscle-tendon length calculation during walking between generic and HMF-fitted musculoskeletal models as a next step. Furthermore, an extension of the model library based on the Visible Human Dataset from the U.S. National Library of Medicine, which includes Computed Tomography and MR images of one male and one female cadaver, is planned. The Visible Human Dataset has been applied to musculoskeletal research, educational, virtual reality, industry, and diagnostic purposes and thus will provide widely accepted reference models for future use.

The solution of the HMF objective function (equation (1)) is, in the present form, dependent on the geometry of the lower body mesh (i.e., mesh nodal degrees of freedom) and the magnitudes of the Sobolev smoothing constraints. Both, the geometry of the lower body mesh and the Sobolev smoothing constraints, have not been linked to physiological or anatomically based principles but were defined according to previously established kinematic criteria [18]. Kinematic surface-based deformation methods have extensively been used in computer graphics research [27]. Yet, they are traditionally not considering biological soft tissue as elastic solids subject to Newton's of motion. In recent work, Kadleček et al. [28] introduced a physics-based model fitting technique to find the optimum shape of a musculoskeletal model based

on several 3D body surface scans that minimizes the deformation energy, corresponding to the elasticity of biological soft tissue. The consideration of a so-called elastic potential to find the optimum fit solution (equation (1)) while complying to Newton's laws of motion for soft tissue is promising and may offer the potential to improve the accuracy of the HMF fit for subjects with various degrees of subcutaneous body fat versus muscle tissue.

Additionally, data from ultrasound imaging may allow further insights into mechanical tissue properties to advance the HMF technique based on anatomically aware principles [20]. Capturing subject-specific mechanical properties of soft tissue is particularly important when aiming to analyze kinetic variables, e.g., muscle forces, in patients with musculoskeletal disorders such as CP. Yet, taking subject-specific tissue samples *in vivo* for refining musculoskeletal models remains highly invasive and very compromised. Ultrasound data would allow to better capture mechanical properties of muscles at the tissue level, e.g., physiological cross-sectional area and fiber pennation angle, which in turn affect muscle mechanics. Ultrasound imaging is relatively inexpensive, does not involve ionizing radiation, and requires much shorter scan times compared with other imaging modalities such as MR imaging. Thereby, an anatomically aware deformation method was recently introduced by Saito et al. [29] to predict the growth and size of muscles by discretizing the anisotropic stretch in the direction of muscle fibers. The integration of muscle fiber structures into the present musculoskeletal modelling approach is highly feasible. In particular, a muscle fascicle description has already successfully been integrated into the muscle organ models in CMISS and fitted to subject-specific ultrasound data with good qualitative agreement to diffusion-weighted MR images [30].

In this study, the skin boundary surfaces of individual subjects were segmented based on MR data, though body surface scanning could be used to capture the outer skin surface of individual subjects in future work. Body surface scanning, frequently used in anthropometric body shape analysis and obesity research, offers inexpensive, rapid, and noninvasive means to characterize the skin boundary *in vivo* [31] and would make the application of the HMF technique feasible in clinical settings. Thereby, the numerical algorithms associated with HMF, as well as the library of MR-based musculoskeletal models, are currently transferred into the open source modelling environment Open-CMISS (http://www.opencmiss.org/) to provide the most advanced and

accessible numerical tools for physiologically based modelling of deformable organs, e.g., muscle tissue across multiple scales, including multibody dynamic analysis [19, 21, 22, 30].

5. Conclusions

The current study presents a crucial step towards personalized human movement analysis by demonstrating the feasibility of fitting a generic musculoskeletal model of the lower limbs to skin surface data of children with and without CP. The musculoskeletal models of the lower limbs and fitting algorithms are planned to be further developed and shared between research centers through the IUPS Physiome Project [19] and coupled with experimentally measured gait data for dynamic simulations of walking. Additional improvements in the quality of fit are expected to be gained by developing age-matched generic models for different study groups, as well as taking into account subject-specific skin fold measures and mechanical properties of muscle tissue based on ultrasound imaging. It is anticipated that the application of personalized musculoskeletal models to movement analysis will lead to crucial new insights into the complex relationship between musculoskeletal architecture and function during dynamic activities and thus assist in the assessment and management of movement pathologies due to conditions such as CP.

Data Availability

The MR image data used for this study are restricted by the New Zealand Northern Y Regional Ethics Committee in order to protect patient privacy. The data is only available to researchers who meet the criteria for accessing the confidential data. Further information can be obtained from the corresponding author Dr. Katja Oberhofer (katja.oberhofer@hest.ethz.ch).

Conflicts of Interest

All authors declare that they have no proprietary, financial, professional, or other personal relationships or obligations of any kind with other people or organisations that could inappropriately influence their work.

Acknowledgments

References

[1] A. S. Arnold, M. Q. Liu, M. H. Schwartz, S. Õunpuu, and S. L. Delp, "The role of estimating muscle-tendon lengths and velocities of the hamstrings in the evaluation and treatment of crouch gait," *Gait & Posture*, vol. 23, no. 3, pp. 273–281, 2006.

[2] F. Schellenberg, K. Oberhofer, W. R. Taylor, and S. Lorenzetti, "Review of modelling techniques for *in vivo* muscle force estimation in the lower extremities during strength training," *Computational and Mathematical Methods in Medicine*, vol. 2015, Article ID 483921, 12 pages, 2015.

[3] M. D. Klein Horsman, H. F. J. M. Koopman, F. C. T. van der Helm, L. P. Prosé, and H. E. J. Veeger, "Morphological muscle and joint parameters for musculoskeletal modelling of the lower extremity," *Clinical Biomechanics*, vol. 22, no. 2, pp. 239–247, 2007.

[4] I. Jonkers, C. Stewart, K. Desloovere, G. Molenaers, and A. Spaepen, "Musculo-tendon length and lengthening velocity of rectus femoris in stiff knee gait," *Gait & Posture*, vol. 23, no. 2, pp. 222–229, 2006.

[5] U. Trinler and R. Baker, "Estimated landmark calibration of biomechanical models for inverse kinematics," *Medical Engineering & Physics*, vol. 51, pp. 79–83, 2018.

[6] J. A. Reinbolt, J. F. Schutte, B. J. Fregly et al., "Determination of patient-specific multi-joint kinematic models through two-level optimization," *Journal of Biomechanics*, vol. 38, no. 3, pp. 621–626, 2005.

[7] M. E. Lund, M. S. Andersen, M. de Zee, and J. Rasmussen, "Scaling of musculoskeletal models from static and dynamic trials," *International Biomechanics*, vol. 2, no. 1, pp. 1–11, 2015.

[8] P. Rymaszewski, C. Stewart, D. Blana, E. Chadwick, S. Sardar, and S. Jarvis, "Musculoskeletal modelling simulation with optimisation to predict the morphological parameters of the calf muscle," *Gait & Posture*, vol. 57, pp. 87-88, 2017.

[9] R. Lampe, S. Grassl, J. Mitternacht, L. Gerdesmeyer, and R. Gradinger, "MRT-measurements of muscle volumes of the lower extremities of youths with spastic hemiplegia caused by cerebral palsy," *Brain and Development*, vol. 28, no. 8, pp. 500–506, 2006.

[10] A. A. Mohagheghi, T. Khan, T. H. Meadows, K. Giannikas, V. Baltzopoulos, and C. N. Maganaris, "Differences in gastrocnemius muscle architecture between the paretic and non-paretic legs in children with hemiplegic cerebral palsy," *Clinical biomechanics*, vol. 22, no. 6, pp. 718–724, 2007.

[11] K. Oberhofer, N. S. Stott, K. Mithraratne, and I. A. Anderson, "Subject-specific modelling of lower limb muscles in children with cerebral palsy," *Clinical Biomechanics*, vol. 25, no. 1, pp. 88–94, 2010.

[12] T. A. Correa, R. Baker, H. Kerr Graham, and M. G. Pandy, "Accuracy of generic musculoskeletal models in predicting the functional roles of muscles in human gait," *Journal of Biomechanics*, vol. 44, no. 11, pp. 2096–2105, 2011.

[13] L. Scheys, K. Desloovere, P. Suetens, and I. Jonkers, "Level of subject-specific detail in musculoskeletal models affects hip moment arm length calculation during gait in pediatric subjects with increased femoral anteversion," *Journal of Biomechanics*, vol. 44, no. 7, pp. 1346–1353, 2011.

[14] A. Carriero, A. Zavatsky, J. Stebbins, T. Theologis, and S. J. Shefelbine, "Correlation between lower limb bone morphology and gait characteristics in children with spastic diplegic cerebral palsy," *Journal of Pediatric Orthopaedics*, vol. 29, no. 1, pp. 73–79, 2009.

[15] B. Gilles and N. Magnenat-Thalmann, "Musculoskeletal MRI segmentation using multi-resolution simplex meshes with medial representations," *Medical Image Analysis*, vol. 14, no. 3, pp. 291–302, 2010.

[16] L. Scheys, K. Desloovere, A. Spaepen, P. Suetens, and I. Jonkers, "Calculating gait kinematics using MR-based

kinematic models," *Gait & Posture*, vol. 33, no. 2, pp. 158–164, 2011.

[17] J. Fernandez, P. Hunter, V. Shim, and K. Mithrraratne, "A subject-specific framework to inform musculoskeletal modeling: outcomes from the IUPS physiome project," in *Patient-Specific Computational Modeling*, pp. 39–60, Springer, 2012.

[18] J. W. Fernandez, P. Mithrraratne, S. F. Thrupp, M. H. Tawhai, and P. J. Hunter, "Anatomically based geometric modelling of the musculo-skeletal system and other organs," *Biomechanics and Modeling in Mechanobiology*, vol. 2, no. 3, pp. 139–155, 2004.

[19] J. Fernandez, J. Zhang, V. Shim et al., "Musculoskeletal modelling and the Physiome Project," in *Multiscale Mechanobiology of Bone Remodeling and Adaptation*, P. Pivonka, Ed., pp. 123–174, Springer International Publishing, Cham, 2018.

[20] E. Passmore, A. Lai, M. Sangeux, A. G. Schache, and M. G. Pandy, "Application of ultrasound imaging to subject-specific modelling of the human musculoskeletal system," *Meccanica*, vol. 52, no. 3, pp. 665–676, 2017.

[21] K. Oberhofer, K. Mithrraratne, N. S. Stott, and I. A. Anderson, "Anatomically-based musculoskeletal modeling: prediction and validation of muscle deformation during walking," *The Visual Computer*, vol. 25, no. 9, pp. 843–851, 2009.

[22] N. S. Stott and I. A. Anderson, "A novel approach to compute muscle length during walking using subject-specific musculoskeletal models," in *The 16th IASTED International Conference on Applied Simulation and Modelling*, pp. 451–456, ACTA Press, Palma de Mallorca, Spain, 2007.

[23] A. Cappozzo, U. Della Croce, A. Leardini, and L. Chiari, "Human movement analysis using stereophotogrammetry: part 1: theoretical background," *Gait & Posture*, vol. 21, no. 2, pp. 186–196, 2005.

[24] F. J. Massey Jr, "The Kolmogorov-Smirnov test for goodness of fit," *Journal of the American Statistical Association*, vol. 46, no. 253, pp. 68–78, 1951.

[25] G. Keppel and T. Wickens, *Simultaneous Comparisons and the Control of Type I Errors. Design and Analysis: A Researcher's Handbook*, Pearson Prentice Hall, Upper Saddle River (NJ), 4th ed edition, 2004.

[26] K. Oberhofer, K. Mithrraratne, N. S. Stott, and I. A. Anderson, "Error propagation from kinematic data to modeled muscle-tendon lengths during walking," *Journal of Biomechanics*, vol. 42, no. 1, pp. 77–81, 2009.

[27] D. Lee, M. Glueck, A. Khan, E. Fiume, and K. Jackson, "A survey of modeling and simulation of skeletal muscle," *ACM Transactions on Graphics*, vol. 28, no. 4, pp. 1–13, 2010.

[28] P. Kadleček, A. E. Ichim, T. Liu, J. Křivánek, and L. Kavan, "Reconstructing personalized anatomical models for physics-based body animation," *ACM Transactions on Graphics*, vol. 35, no. 6, pp. 1–13, 2016.

[29] S. Saito, Z. Y. Zhou, and L. Kavan, "Computational body-building: anatomically-based modeling of human bodies," *ACM Transactions on Graphics*, vol. 34, no. 4, pp. 41:1–41:12, 2015.

[30] M. Alipour, K. Mithrraratne, R. D. Herbert, and J. Fernandez, "A 3D ultrasound informed model of the human gastrocnemius muscle," in *Imaging for Patient-Customized Simulations and Systems for Point-of-Care Ultrasound*, pp. 27–34, Springer, 2017.

[31] J. C. K. Wells, A. Ruto, and P. Treleaven, "Whole-body three-dimensional photonic scanning: a new technique for obesity research and clinical practice," *International Journal of Obesity*, vol. 32, no. 2, pp. 232–238, 2008.

Research Article

Measurement of Flexion Angle of the Finger Joint during Cylinder Gripping Using a Three-Dimensional Bone Model Built by X-Ray Computed Tomography

Satoshi Shimawaki[ID],[1] Takuma Murai,[1] Masataka Nakabayashi,[1] and Hideharu Sugimoto[2]

[1]*Department of Mechanical and Intelligent Engineering, Utsunomiya University, 7-1-2 Yoto, Utsunomiya, 321-8585 Tochigi, Japan*
[2]*Department of Radiology, School of Medicine, Jichi Medical University and Hospital, 3311-1 Yakushiji, Shimotsuke, 329-0498 Tochigi, Japan*

Correspondence should be addressed to Satoshi Shimawaki; simawaki@cc.utsunomiya-u.ac.jp

Motion analysis of the thumb and the four fingers during human gripping of a cylindrical object is a prerequisite for designing motion mechanisms in electronic arm prostheses and robotic hands. Conventional measurement methods include the use of angle sensors or multiple video recording of markers. In the present study, we performed X-ray computed tomography (CT) imaging on fingers gripping cylinders of three different diameters (10, 60, and 120 mm) and constructed a bone model based on these CT images to directly measure the flexion angle of each finger joint. We then compared the results with the flexion angles of joints measured using other methods. The subjects comprised 10 Japanese men with no hand injuries or diseases. Our results showed that smaller cylinder diameters were associated with significant increases in the flexion angle of all the joints of the four fingers. When focusing on the distal interphalangeal joint (DIP), there was no significant difference between any of the fingers for each of the cylinders, except between the index and middle fingers for the 10 mm-diameter cylinder. When focusing on the 10 mm-diameter cylinder, the flexion angle of the proximal interphalangeal joint (PIP) of each finger was significantly larger than that of the DIP and metacarpophalangeal joint (MP). However, no such significant difference was noted for the 120 mm-diameter cylinder. The coupling ratio (CR), which is the ratio of the flexion angles of the DIP and PIP, was significantly smaller for the 10 mm-diameter cylinder than for the 60 mm-diameter cylinder. However, there were no significant differences in CR between any of the fingers. A comparison of our study results with those derived using other methods indicated quantitative consistency for the DIP and PIP. However, for the MP, we noted differences that may be explained by the difficulty in determining the longitudinal axis of the metacarpal using other methods.

1. Introduction

Several studies have investigated the gripping of an object by human fingers. Napier [1] classified gripping patterns into power and precision grips based on the anatomical and functional viewpoints. Power grip involves the manipulation of an object using the hand and arm, whereas precision grip involves the manipulation of an object using the fingers. Landsmeer [2] also classified gripping into two types, namely power grip and precision handling. With the former, the finger pulp is in an opposing position to the palm, whereas with the latter, the finger pulp is in an opposing position to the thumb pulp. With the power grip, the fingers and palm pressed against the object make it possible to convey a strong force to the object. The main type of gripping employed when holding a cylinder is the power grip.

When designing motion mechanisms for electronic arm prostheses and humanoid fingers (robotic hands), it is important to evaluate motion analysis of the thumb and the four fingers when a person grips a cylindrical object. Moreover, human motion data are crucial in enabling such devices to perform human-like finger movements. The use of an

(a)

(b)

(c)

(d)
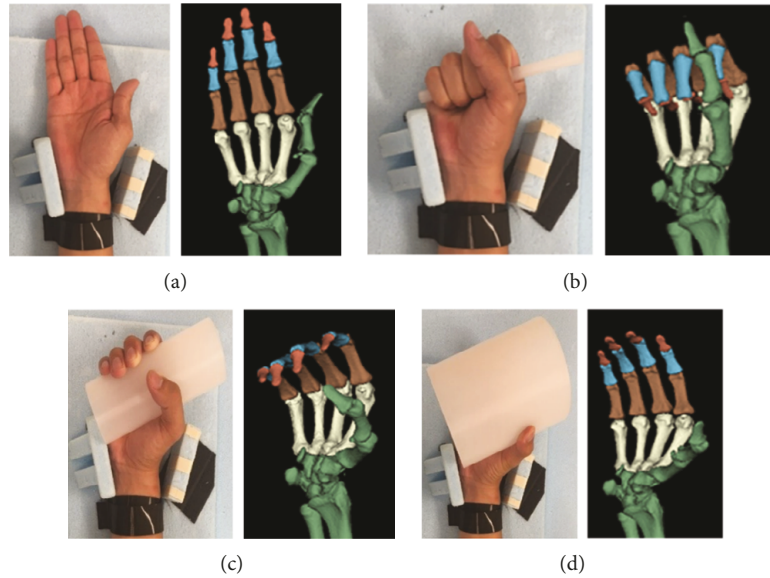
FIGURE 1: CT imaging positions and three-dimensional bone models. (a) Basic position, (b) gripping a 10 mm-diameter cylinder, (c) gripping a 60 mm-diameter cylinder, and (d) gripping a 120 mm-diameter cylinder.

actuator for each joint would result in a bulky and intricate electronic arm prosthesis. Therefore, coordinated coupling between joints should be considered to reduce the number of actuators [3, 4]. Such data could also be useful for hand and finger function diagnosis [5].

Studies have used different methods to measure the joint angles of the thumb and the four fingers while gripping a cylinder. Some of these methods employed an angle sensor attached to the back of the hand [6–8], whereas others used multiple video cameras recording the markers affixed to the back of the hand [9–13]. Although a high-precision angle measurement can be performed, the angles measured can be indirectly affected by the skin and subcutaneous tissue because the markers or angle sensors are affixed to the skin surface. To avoid this bias, we applied a method based on a bone model that was generated for numerical simulation based on X-ray CT images from our previous study [14] to measure the joint angle. This method can measure the joint angle more directly.

In this study, we performed X-ray CT imaging on the hands gripping cylinders with three different diameters and constructed bone models for the distal phalanx, middle phalanx, and proximal phalanx and for the second to fifth metacarpal of the four fingers excluding the thumb. We measured the flexion angle of each joint and compared the results with the flexion angles measured by other researchers using other methods.

2. Methods

2.1. Subjects. The subjects comprised 10 Japanese men with no hand injuries or diseases, with ages ranging from 21 to 25 years, mean height of 173.0 ± 4.4 cm (mean ± standard deviation), mean weight of 65.0 ± 10.1 kg, mean body fat percentage of $16.7 \pm 5.2\%$, and mean body mass index of 21.7 ± 3.1. The mean hand length of subjects (distance from

the tip of the middle finger to the wrist crease) was 185.8 ± 8.1 mm. The mean palm length (distance from the palmo-phalangeal crease of the middle finger to the wrist crease) was 107.7 ± 5.8 mm, and the mean hand width (distance from the radial surface of the MP of the index finger to the medial surface of the distal palm crease) was 86.3 ± 5.9 mm. This study was approved by the Institutional Review Board for Research on Human Subjects of Utsunomiya University (Approval no. H17-0016). Before performing the experiment, subjects were given thorough explanations of the purpose and details of the study, and each subject provided written consent.

2.2. CT Imaging and Three-Dimensional Bone Model Construction. Cross-sectional images distal from the midshaft of the forearm (spatial resolution: 512×512) were obtained with a field of view of 180 mm and slice thickness of 0.5 mm using an X-ray CT scanner (SOMATOM Definition AS; Siemens AG, Munich, Germany). The X-ray tube voltage was 120 kV and the tube current was 48 mA. CT images were obtained with the hands in the following four positions: basic position not gripping any cylinder and with all fingers extended, gripping a 10 mm-diameter cylinder, gripping a 60 mm-diameter cylinder, and gripping a 120 mm-diameter cylinder (Figure 1). All cylinders were made of polypropylene. The gripping type was power grip using the five fingers including the thumb and the palm surface. However, the thumb was set opposing the other fingers. During CT imaging, the distal and central parts of the forearm and distal part of the upper arm were fixated with bands so that only the five fingers and palm could move. Subjects were instructed to hold their wrist in a neutral position. Radioulnar deviation of the wrist was restricted using holders fixed to the jig, and flexion of the wrist was restricted by contacting the back of the hand with the jig.

Open source software (3D Slicer; ver. 4.5) for visualizing medical images was used to construct the three-dimensional
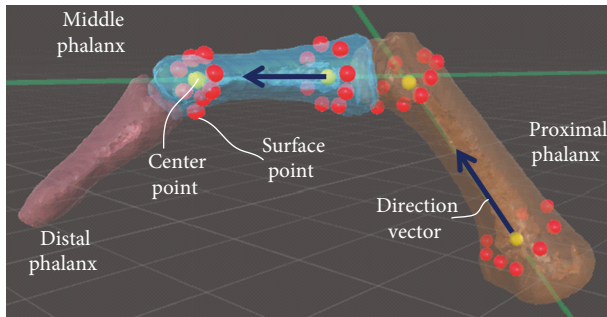
FIGURE 2: Method for calculating the flexion angle of the PIP. Direction vectors from the center of the proximal base to the center of the distal head of the middle phalanx and proximal phalanx were calculated, and the angle created by these two direction vectors was considered to be the flexion angle of the PIP.

bone models based on CT images of all bones distal from the distal portions of the radial and ulnar visually (Figure 1). Coordinates were set in the three-dimensional bone models. The origin of the coordinate system was set as the concave part of the dorsal surface of the capitate in the basic position. The y-axis was a line passing through the origin and the direction of the long axis of the third metacarpal (proximal direction was set as positive), the x-axis was a line passing through the origin and running in the palmardorsal direction to intersect the y-axis (palm direction was set as positive), and the z-axis was a line passing through the origin and running in the radioulnar direction (radial direction was set as positive) to intersect the y-axis [15].

2.3. Flexion Angles for the Interphalangeal Joints. Bone models for each cylinder gripped were used to measure the flexion angles of the distal interphalangeal joints (DIPs), proximal interphalangeal joints (PIPs), and metacarpophalangeal joints (MPs) of the four fingers (index, middle, ring, and little). The thumb was excluded from the measurements because the location of the thumb varies greatly among individuals when gripping a cylindrical object. For example, we used the following method to calculate the flexion angle of the PIP of the index finger (Figure 2). Eight surface points with intervals of approximately 45° are selected from the outer circumference of the distal head of the middle phalanx of the index finger. The coordinate of the center of the distal head of the middle phalanx is determined on the basis of the coordinates of these eight points. The coordinates of the centers of the proximal base of the middle phalanx, the distal head, and the proximal base of the proximal phalanx are determined in a similar manner. For both bones, direction vectors from the center of the proximal base to the center of the distal head are calculated and the angle created by these direction vectors is considered the flexion angle for the PIP of the index finger. The flexion angles for the DIPs, PIPs, and MPs of the four other fingers are similarly calculated.

When gripping an object, both the DIP and PIP are flexed. However, it has been reported that the flexion angle proportions of these joints are independent of the size of the object [6]. Therefore, we defined the flexion angle proportions of the DIP and PIP as the coupling ratio (CR).

2.4. Statistical Analysis. A three-way ANOVA with repeated measurement (diameter A (3) × finger B (4) × joint C (3)) was conducted for the flexion angle as the dependent variable (SPSS Statistics, Ver. 22, IBM). Sphericity was confirmed using Mauchly's sphericity test. If the sphericity hypothesis was denied, then the Greenhouse–Geisser correction was used. Three-way ANOVA results indicated that secondary ($A \times B \times C$) and primary ($A \times B$, $A \times C$, and $B \times C$) interactions were significant (Table 1). We performed simple main effect test as well as multiple comparisons using the Bonferroni method.

A two-way ANOVA with repeated measurement (diameter A (3) × finger B (4)) was conducted for CR as the dependent variable. Sphericity was confirmed using Mauchly's sphericity test. If the sphericity hypothesis was denied, then the Greenhouse–Geisser correction was used. The results of the two-way ANOVA indicated that interaction ($A \times B$) was not significant ($F(6, 54) = 0.505$, n.s.), but the main effect (A, B) was significant (A: $F(2, 18) = 4.981$, $P = 0.019$; B: $F(2.247, 20.22) = 3.436$, $P = 0.047$). Therefore, a multiple comparison was conducted using the Bonferroni method.

3. Results

3.1. Joint Flexion Angles. Table 2 shows the mean flexion angle and standard deviation in each joint (DIP, PIP, and MP) from the index finger to the little finger when cylinders of the three different diameters (10, 60, 120 mm) were gripped. Two of the three factors were selected. Multiple comparisons of the remaining factor were analyzed at combinations of all levels in the two selected factors using the Bonferroni method. The level of significance was set at $\alpha = 0.05$.

3.1.1. "Diameter A" Factor. Table 3 shows results for multiple comparisons of the "Diameter A" factor for combinations of all levels in the "Finger B" and "Joint C" factors. Although no significant differences were noted for the index finger in some comparisons, the flexion angle was found to significantly increase with smaller cylinder diameters. The result shows that all joints in all fingers have larger flexion angles when gripping an object with a small cylinder diameter compared with when gripping an object with a larger cylinder diameter.

3.1.2. "Finger B" Factor. Table 4 shows the results for multiple comparisons of the "Finger B" factor for combinations of all levels in the "Diameter A" and "Joint C" factors. When focusing on the DIP in particular, the only significant difference noted between any of the levels was between the index finger and the middle finger for the 10 mm-diameter cylinder. The result indicates that DIP joints in all fingers contribute equally when gripping a cylindrical object. When focusing on the PIP in particular, the flexion angle of the little finger was significantly smaller than that of the other fingers in conditions for which significant differences were observed. The result shows that the DIP joint in the little finger contributes less than that in other fingers when gripping a cylindrical object. In addition, the DIP joints in all the other fingers were

TABLE 1: Three-way ANOVA with repeated measurement (diameter A (3) × finger B (4) × joint C (3)). The dependent variable was the flexion angle.

Source of variation	Degree of freedom	Type III SS	Mean squares	F	P
Diameters A[a]	1.149	207,673.697	180,797.809	1025.177	<0.001
Fingers B[b]	3	4014.324	1338.108	27.279	<0.001
Joints C[c]	2	26,868.242	13,434.121	28.683	<0.001
$A \times B$	6	2151.941	358.657	12.524	<0.001
$A \times C$	2.301	19,652.346	8542.455	23.408	<0.001
$B \times C$	6	2653.076	442.179	6.792	<0.001
$A \times B \times C$	12	2488.546	207.379	3.036	0.001

[a]Diameters—10 mm, 60 mm, and 120 mm. [b]Fingers—index, middle, ring, and small. [c]Joints—DIP, PIP, and MP. SS: sums of squares.

TABLE 2: Mean flexion angle of each joint from the index to the little finger when cylinders of the different diameters were gripped. Numbers in the lower brackets indicate standard deviation.

Diameter	Index (deg)			Middle (deg)		
	DIP	PIP	MP	DIP	PIP	MP
10 mm	48.2 (22.7)	105.5 (9.2)	65.6 (7.9)	64.8 (16.4)	104.8 (9.8)	75.9 (5.5)
60 mm	35.2 (6.8)	48.0 (7.7)	39.7 (11.8)	34.5 (7.5)	48.1 (8.1)	46.3 (15.4)
120 mm	18.9 (6.1)	24.2 (6.5)	32.2 (5.5)	20.0 (12.0)	25.9 (6.7)	22.9 (10.3)

Diameter	Ring (deg)			Small (deg)		
	DIP	PIP	MP	DIP	PIP	MP
10 mm	57.2 (16.8)	110.5 (6.1)	76.6 (14.9)	65.8 (8.9)	93.0 (13.3)	64.1 (12.1)
60 mm	27.1 (7.1)	48.7 (6.8)	38.7 (12.5)	30.0 (9.6)	32.8 (11.3)	35.2 (15.9)
120 mm	16.1 (6.4)	24.7 (9.1)	15.1 (8.5)	11.9 (5.3)	15.2 (5.2)	12.6 (5.7)

found to contribute equally. When focusing on the MP in particular, although the flexion angle of the index finger for the 10 mm-diameter cylinder was significantly smaller than that of the middle finger, the flexion angle of the index finger for the 120 mm-diameter cylinder was significantly larger than the flexion angle of the other fingers. This result shows that the contribution of a finger changes according to the diameter of an object.

3.1.3. "Joint C" Factor. Table 5 shows the results for multiple comparisons of the "Joint C" factor for combinations of all levels in the "Diameter A" and "Finger B" factors. When focusing on the 10 mm-diameter cylinder in particular, the flexion angle of the PIP of each finger was significantly larger than that of the DIP and MP. However, no significant difference was noted for the 120 mm-diameter cylinder. When focusing on the 90 mm-diameter cylinder, although the flexion angle of the DIP of the middle and ring fingers was significantly smaller than that of the PIP and MP, no significant differences were noted between any joint for the index and little fingers. This result indicates that the PIP joints in all fingers contribute the most when the diameter of the gripped

object is small. However, the contribution of all fingers becomes more equal with an increase in the diameter of the gripped object.

3.2. Coupling Ratio (CR). Table 6 shows the CR, which is the ratio of the flexion angles of the DIP and PIP. Results of multiple comparisons of main effects using the Bonferroni method indicated that for "Diameter A" and "Finger B" factors, the CR of the 10 mm-diameter cylinder was significantly smaller than that of the 60 mm-diameter cylinder. No significant differences were noted among any of the levels in the "Finger B" factor. CR hardly changed when the cylinder diameter was large. In other words, the DIP and PIP joints in all fingers were found to flex synchronously under such conditions.

4. Discussion

Several studies have measured the flexion range of motion (ROM) of each finger joint [16–18]. The mean flexion ROM of the DIP, PIP, and MP was 68°, 104°, and 80° for the index finger; 70°, 107°, and 85° for the middle finger;

TABLE 3: p value as calculated with multiple comparisons of the "Diameter A" factor.

Comparison	Index			Middle		
	DIP	PIP	MP	DIP	PIP	MP
$A1$ vs $A2$	0.155 n.s.	<0.0005 $A1 > A2$	<0.0005 $A1 > A2$	<0.0005 $A1 > A2$	<0.0005 $A1 > A2$	<0.0005 $A1 > A2$
$A2$ vs $A3$	<0.0005 $A2 > A3$	<0.0005 $A2 > A3$	0.084 n.s.	0.001 $A2 > A3$	<0.0005 $A2 > A3$	<0.0005 $A2 > A3$
$A1$ vs $A3$	0.011 $A1 > A3$	<0.0005 $A1 > A3$	<0.0005 $A1 > A3$	<0.0005 $A1 > A3$	<0.0005 $A1 > A3$	<0.0005 $A1 > A3$
Comparison	Ring			Small		
	DIP	PIP	MP	DIP	PIP	MP
$A1$ vs $A2$	0.001 $A1 > A2$	<0.0005 $A1 > A2$	0.001 $A1 > A2$	<0.0005 $A1 > A2$	<0.0005 $A1 > A2$	0.001 $A1 > A2$
$A2$ vs $A3$	<0.0005 $A2 > A3$	<0.0005 $A2 > A3$	<0.0005 $A2 > A3$	<0.0005 $A2 > A3$	0.004 $A2 > A3$	0.002 $A2 > A3$
$A1$ vs $A3$	<0.0005 $A1 > A3$	<0.0005 $A1 > A3$	<0.0005 $A1 > A3$	<0.0005 $A1 > A3$	<0.0005 $A1 > A3$	<0.0005 $A1 > A3$

Significance level: $\alpha = 0.05$. $A1 = 10$ mm, $A2 = 60$ mm, and $A3 = 120$ mm.

TABLE 4: p value as calculated with multiple comparisons of the "Finger B" factor.

Comparison	Diameter 10 mm			Diameter 60 mm			Diameter 120 mm		
	DIP	PIP	MP	DIP	PIP	MP	DIP	PIP	MP
$B1$ vs $B2$	0.002 $B1 < B2$	1.0 n.s.	0.011 $B1 < B2$	1.0 n.s.	1.0 n.s.	0.391 n.s.	1.0 n.s.	1.0 n.s.	0.014 $B1 > B2$
$B1$ vs $B3$	0.551 n.s.	1.0 n.s.	0.729 n.s.	0.10 n.s.	1.0 n.s.	1.0 n.s.	1.0 n.s.	1.0 n.s.	<0.0005 $B1 > B3$
$B1$ vs $B4$	0.084 n.s.	0.128 n.s.	1.0 n.s.	0.661 n.s.	0.004 $B1 > B4$	0.874 n.s.	0.065 n.s.	0.162 n.s.	<0.0005 $B1 > B4$
$B2$ vs $B3$	0.353 n.s.	0.704 n.s.	1.0 n.s.	0.191 n.s.	1.0 n.s.	0.302 n.s.	1.0 n.s.	1.0 n.s.	0.018 $B3 > B4$
$B2$ vs $B4$	1.000 n.s.	0.007 $B2 > B4$	0.026 $B2 > B4$	0.65 n.s.	0.003 $B2 > B4$	0.071 n.s.	0.097 n.s.	0.025 $B2 > B4$	0.108 n.s.
$B3$ vs $B4$	0.861 n.s.	0.006 $B3 > B4$	0.382 n.s.	1.0 n.s.	0.001 $B3 > B4$	0.510 n.s.	0.705 n.s.	0.348 n.s.	1.0 n.s.

Significance level: $\alpha = 0.05$. $B1 = $ index, $B2 = $ middle, $B3 = $ ring, and $B4 = $ small.

$66°$, $107°$, and $87°$ for the ring finger; and $69°$, $104°$, and $86°$ for the little finger, respectively [18]. The flexion angles of the PIPs when holding a 10 mm-diameter cylinder have almost the same mean flexion ROM, as shown in Table 2. However, the flexion angles of the DIP of the index finger and the MP of the little finger when gripping the 10 mm-diameter cylinder in our study were smaller than the mean flexion ROM.

Several studies have also measured the flexion angles of each finger when gripping a cylinder. Lee and Rim [9] simultaneously recorded multiple markers affixed to the finger dorsal surface using four video cameras and calculated the three-dimensional coordinates of the markers to measure the flexion angles of the DIP, PIP, and MP of the four fingers. However, because the range of diameters of the gripped cylinders (25–50 mm) was relatively narrow, it was concluded that although the flexion angles of the PIP and MP increase as the cylinder diameter decreases, the flexion angle of the DIP remains fixed regardless of the cylinder size. Takano et al. [10] used the same method as Lee and Rim [9] to measure the flexion angles of the five fingers, including the thumb. Cylinder diameters ranged from 18 mm to 73 mm, with a decrease in the flexion angles of the four fingers, excluding the thumb, with increases in the cylinder diameter. Gülke et al. [6] used a sensor glove with 14 joint angle sensors affixed to the back of the hand to measure the flexion angles of the five fingers. Cylinder diameters ranged from 40 mm to 120 mm. Similar to the results reported by Takano et al., the flexion angles of the four fingers, excluding the thumb, decreased with increasing cylinder diameters. Lee and Jung [11] affixed multiple reflective markers to the back of the hand and used the VICON system to measure the flexion angles of the five fingers in different gripping positions.

Table 5: p value as calculated with multiple comparisons of the "Joint C" factor.

Comparison	Index			Middle		
	10 mm	60 mm	120 mm	10 mm	60 mm	120 mm
$C1$ vs $C2$	**0.001**	0.050	0.508	**<0.0005**	**0.034**	0.958
	$C1 < C2$	n.s.	n.s.	$C1 < C2$	$C1 < C2$	n.s.
$C1$ vs $C3$	0.125	0.636	**<0.0005**	0.148	**0.041**	0.840
	n.s.	n.s.	$C1 < C3$	n.s.	$C1 < C3$	n.s.
$C2$ vs $C3$	**<0.0005**	0.538	0.057	**<0.0005**	1.0	1.0
	$C2 > C3$	n.s.	n.s.	$C2 > C3$	n.s.	n.s.
Comparison	Ring			Small		
	10 mm	60 mm	120 mm	10 mm	60 mm	120 mm
$C1$ vs $C2$	**<0.0005**	**0.001**	0.095	**0.006**	1.0	0.536
	$C1 < C2$	$C1 < C2$	n.s.	$C1 < C2$	n.s.	n.s.
$C1$ vs $C3$	0.06	**0.042**	1.0	1.0	0.713	1.0
	n.s.	$C1 < C3$	n.s.	n.s.	n.s.	n.s.
$C2$ vs $C3$	**<0.0005**	0.343	0.195	**0.008**	1.0	1.0
	$C2 > C3$	n.s.	n.s.	$C2 > C3$	n.s.	n.s.

Significant level: $\alpha = 0.05$. $C1$ = DIP, $C2$ = PIP, and $C3$ = MP.

Table 6: Coupling ratio (CR), the ratio of the flexion angles of the DIP and PIP.

Diameter	Index	Middle	Ring	Small	All
10 mm	0.47 (0.24)	0.62 (0.16)	0.52 (0.16)	0.73 (0.18)	0.58* (0.20)
60 mm	0.77 (0.29)	0.75 (0.26)	0.58 (0.21)	1.10 (0.67)	0.80* (0.43)
120 mm	0.85 (0.41)	0.96 (0.98)	0.73 (0.44)	0.97 (0.67)	0.88 (0.65)
All	0.70 (0.35)	0.78 (0.59)	0.61 (0.30)	0.93 (0.56)	0.75 (0.48)

*$p < 0.05$.

Cylinder diameters ranged from 20 mm to 80 mm. As with the results reported by Takano et al., the flexion angles of the four fingers, excluding the thumb, decreased with increasing cylinder diameters. However, the flexion angles when a cylinder with a smaller diameter was gripped were smaller than those obtained in Takano et al.'s study [10].

Figure 3 compares flexion angles measured in our study with those measured in Takano et al.'s and Gülke et al.'s studies [6, 10]. To simplify the results, the standard deviation is not shown. Figure 3(a) shows that when the flexion angles of the DIP are compared, similar trends are noted for the 10 mm-diameter cylinder in our study as observed by Takano et al. For the 60 mm-diameter cylinder, our results for the middle finger are very consistent with those reported by Takano et al. and Gülke et al., whereas for the other fingers, our results are consistent only with those reported by Takano et al. For the 120 mm-diameter cylinder, our results for the middle and little fingers are highly consistent with those reported by Gülke et al., whereas for the other fingers, differences were observed. Figure 3(b) shows that when the flexion angles of the PIP were compared, similar trends were noted for the 10 mm-diameter cylinder between our study and Takano et al.'s study for all fingers, except for the little finger. For the 60 mm-diameter cylinder, results for all joints are highly consistent with those reported by Takano et al. and Gülke et al. For the 120 mm-diameter cylinder, results for

the index and little fingers were different from those reported by Gülke et al. but highly consistent for the other fingers. Figure 3(c) shows that when the flexion angles of the MP were compared, results were different from those reported by Takano et al. for the 10 mm-diameter cylinder. Differences were also noted for the 60 mm-diameter cylinder compared with those reported by Takano et al. and Gülke et al. For the 120 mm-diameter cylinder, results were highly consistent with those reported by Gülke et al., except for the index finger. A comparison with the results of other researchers who used different measurement methods indicated qualitative consistency, with the flexion angle of each joint shown to decrease with increasing cylinder diameters. While quantitative consistency was noted for the DIP and PIP, large differences were observed for the MP compared with results reported by other researchers. This may have been because other researchers measured flexion angles using video measurement of markers or angle sensors affixed to the back of the hand, and although it is relatively easy to identify long axes of the distal, middle, and proximal phalanxes, it is difficult to determine the long axis of the metacarpal.

Figure 4 compares the results of the CR obtained in our study with those reported by other researchers. A comparison of the results obtained for the index finger shown in Figure 4(a) indicates that the CR increases with increases in the cylinder diameter of up to 60 mm. For cylinders of

(a) DIP

(b) PIP

(c) MP
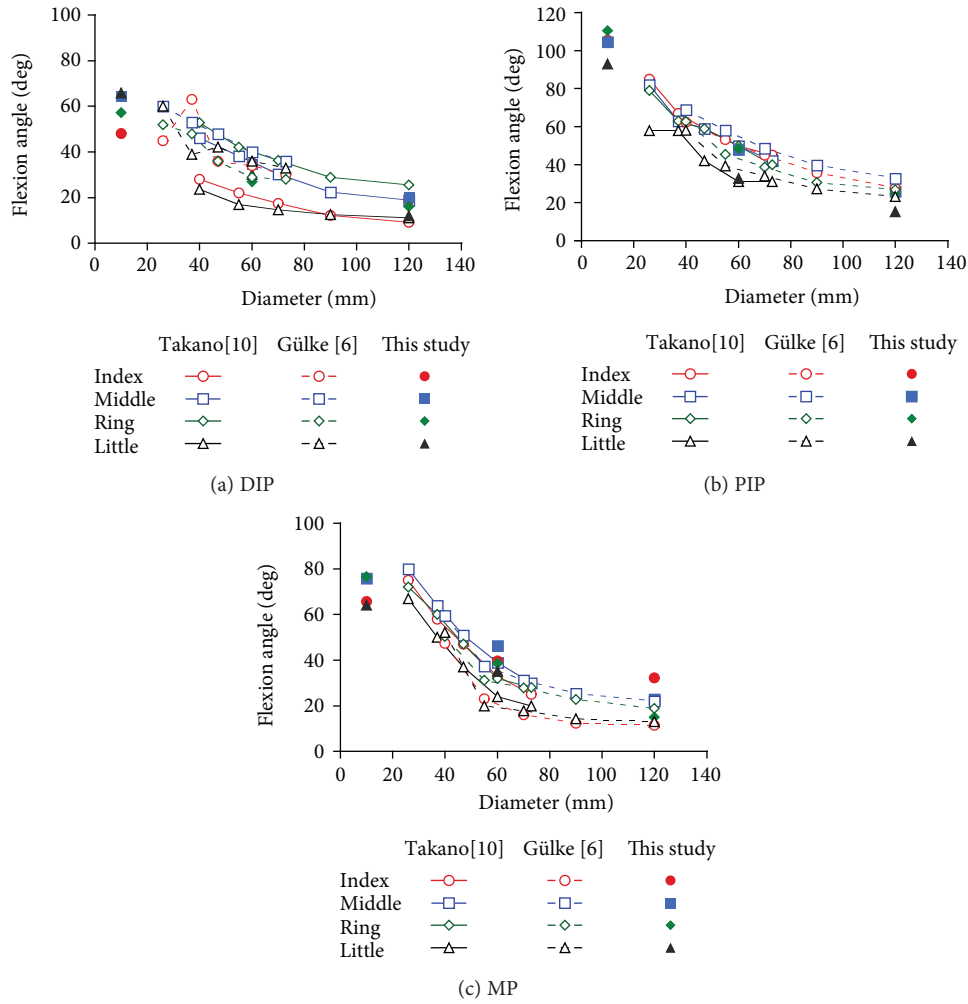
FIGURE 3: A comparison of flexion angles measured in our study with those measured in Takano et al.'s and Gülke et al.'s studies [6, 10].

(a) Index
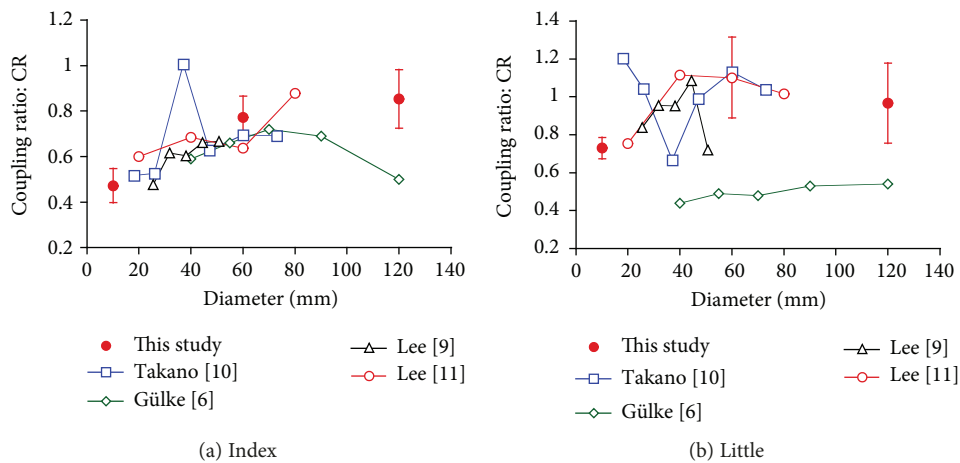
(b) Little

FIGURE 4: A comparison of the CR obtained in our study with those reported by other researchers. ●: this study, ——□——: Takano et al. [10], ——◇——: Gülke et al. [6], ——△——: Lee and Rim [9], and ——○——: Lee and Jung [11].

≥ 60 mm, the CR remains fixed or decreases. A comparison of the results of the little finger shown in Figure 4(b) indicates that the CR increases with increases in the cylinder diameter

of up to 60 mm. For cylinders of ≥ 60 mm, the CR remains almost fixed. However, the standard error indicates large individual variations. Because the results reported by Gülke

et al. indicated different trends to those reported by other researchers, some sort of measurement error may have occurred. Thus, because the CR increases and flexion angles of the DIP and PIP decrease with a cylinder diameter of up to 60 mm (Figure 3), adjustments against the diameter change are mainly conducted by the PIP. Moreover, because the CR is mainly fixed for cylinder diameters of ≥60 mm while joint angles of the DIP and PIP decrease (Figure 3), the adjustments in this case appear to be conducted by both joints.

Table 3 shows that the flexion angles of all joints of the four fingers significantly increased with a decrease in the cylinder diameter. These results, which were also observed by other researchers, indicate that all joints are mobile when the object is gripped. However, as shown in Table 6, the CR (the ratio of the flexion angles of the DIP and PIP) was different for all gripped objects. The CR was significantly smaller when a 10 mm-diameter cylinder was gripped than when a 60 mm-diameter cylinder was gripped. Therefore, the flexion angle of the PIP changes appears to be greater when the gripped object has a diameter changing from 10 mm to 30 mm. According to Table 4, flexion angles of the DIP of the four fingers were almost fixed when objects were gripped and the flexion angle of the PIP of the little finger was smaller than that of the other fingers. According to Table 5, when a 10 mm-diameter cylinder was gripped, the flexion angle of the PIP of all fingers was significantly larger than that of the other joints. However, when a 120 mm-diameter cylinder was gripped, no significant differences were noted between the flexion angle of the PIP and the flexion angles of the other joints, indicating that greater changes were observed in the flexion angles of the PIP.

Several limitations accompany the measurement of the flexion angle using X-ray CT imaging. First, this technique is a low invasive measurement because of the use of X-ray. This makes it difficult to perform measurements in several different conditions on each subject. Therefore, the radiation dose ($CTDI_{vol}$) used in this study was fairly low (5 mGy). Second, only the flexion angle can be measured when the cylindrical object is gripped. When video imaging or a sensor glove is used, the flexion angle during prehension before gripping the cylinder can be simultaneously measured. Third, measurements could only be performed in the CT imaging room. The fourth limitation was that the flexion angles of the thumb joints were not measured. With a sensor glove, flexion angles can be measured during daily living. Thus, our data could be used to verify data measured using video imaging or sensor glove methods.

5. Conclusions

In the present study, we performed X-ray CT imaging on fingers gripping cylinders of three different diameters (10, 60, and 120 mm) and constructed a bone model based on these CT images to directly measure the flexion angle of each finger joint. Our results showed that smaller cylinder diameters were associated with significant increases in the flexion angle of all the joints of the four fingers. When focusing on the 10 mm-diameter cylinder, the flexion angle of the PIP of each finger was significantly larger than that of the DIP and MP. However, no significant difference was noted for the 120 mm-diameter cylinder. The coupling ratio (CR), which is the ratio of the flexion angles of the DIP and PIP, was significantly smaller for the 10 mm-diameter cylinder than for the 60 mm-diameter cylinder. However, there were no significant differences of the CR between any of the fingers.

Data Availability

The data used to support the findings of this study are included within the article. The CT data used to support the findings of this study have not been made available because of privacy protection.

Conflicts of Interest

The authors declare that there are no conflicts of interest regarding the publication of this paper.

Acknowledgments

References

[1] J. R. Napier, "The prehensile movements of the human hand," *Journal of Bone and Joint Surgery*, vol. 38-B, no. 4, pp. 902–913, 1956.

[2] J. M. F. Landsmeer, "Power grip and precision handling," *Annals of the Rheumatic Diseases*, vol. 21, no. 2, pp. 164–170, 1962.

[3] D. A. Bennett, S. A. Dalley, and M. Goldfarb, "Design of a hand prosthesis with precision and conformal grasp capability," in *2012 Annual International Conference of the IEEE Engineering in Medicine and Biology Society*, pp. 3044–30447, San Diego, CA, USA, 2012.

[4] T. E. Wiste, S. A. Dalley, H. Atakan Varol, and M. Goldfarb, "Design of a multigrasp transradial prosthesis," *Journal of Medical Devices*, vol. 5, no. 3, article 031009, 2011.

[5] H. Y. Chiu, S. C. Lin, F. C. Su, S. T. Wang, and H. Y. Hsu, "The use of the motion analysis system for evaluation of loss of movement in the finger," *Journal of Hand Surgery*, vol. 25, no. 2, pp. 195–199, 2000.

[6] J. Gülke, N. J. Wachter, T. Geyer, H. Schöll, G. Apic, and M. Mentzel, "Motion coordination patterns during cylinder grip analyzed with a sensor glove," *The Journal of Hand Surgery*, vol. 35, no. 5, pp. 797–806, 2010.

[7] C. Häger-Ross and M. H. Schieber, "Quantifying the independence of human finger movements: comparisons of digits, hands, and movement frequencies," *The Journal of Neuroscience*, vol. 20, no. 22, pp. 8542–8550, 2000.

[8] M. Santello, M. Flanders, and J. F. Soechting, "Patterns of hand motion during grasping and the influence of sensory guidance," *The Journal of Neuroscience*, vol. 22, no. 4, pp. 1426–1435, 2002.

[9] J. W. Lee and K. Rim, "Measurement of finger joint angles and maximum finger forces during cylinder grip activity," *Journal of Biomedical Engineering*, vol. 13, no. 2, pp. 152–162, 1991.

[10] T. Takano, H. Yamamoto, and T. Hara, "Biomechanical analysis of grasp motion characteristics," *Transactions of the Japan Society of Mechanical Engineers Series C*, vol. 62, no. 603, pp. 4257–4263, 1996.

[11] K. S. Lee and M. C. Jung, "Three-dimensional finger joint angles by hand posture and object properties," *Ergonomics*, vol. 59, no. 7, pp. 890–900, 2016.

[12] H. Y. Chiu, F. C. Su, S. T. Wang, and H. Y. Hsu, "The motion analysis system and goniometry of the finger joints," *Journal of Hand Surgery*, vol. 23, no. 6, pp. 788–791, 1998.

[13] P. Braido and X. Zhang, "Quantitative analysis of finger motion coordination in hand manipulative and gestic acts," *Human Movement Science*, vol. 22, no. 6, pp. 661–678, 2004.

[14] S. Shimawaki, M. Oniwa, M. Nakabayashi, N. Sakai, H. Sugimoto, and S. Yamazaki, "Deformation of the distal radioulnar ligament during rotation using finite element analysis," *Journal of Biomechanical Science and Engineering*, vol. 10, no. 2, article 15-00286, 2015.

[15] G. Wu, F. van der Helm, H. E. Veeger et al., "ISB recommendation on definitions of joint coordinate systems of various joints for the reporting of human joint motion—part II: shoulder, elbow, wrist and hand," *Journal of Biomechanics*, vol. 38, no. 5, pp. 981–992, 2005.

[16] J. C. Becker and N. V. Thakor, "A study of the range of motion of human fingers with application to anthropomorphic designs," *IEEE Transactions on Biomedical Engineering*, vol. 35, no. 2, pp. 110–117, 1988.

[17] R. Degeorges and C. Oberlin, "Measurement of three-joint-finger motions: reality or fancy? A three-dimensional anatomical approach," *Surgical and Radiologic Anatomy*, vol. 25, no. 2, pp. 105–112, 2003.

[18] K. S. Lee and M. C. Jung, "Ergonomic evaluation of biomechanical hand function," *Safety and Health at Work*, vol. 6, no. 1, pp. 9–17, 2015.